



Politecnico
di Bari

Repository Istituzionale dei Prodotti della Ricerca del Politecnico di Bari

Fragility analysis of prestressed concrete girder bridges affected by corrosion under traffic loads

This is a PhD Thesis

Original Citation:

Fragility analysis of prestressed concrete girder bridges affected by corrosion under traffic loads / Nettis, Alessandro. - ELETTRONICO. - (2025).

Availability:

This version is available at <http://hdl.handle.net/11589/282060> since: 2025-01-13

Published version

DOI:

Publisher: Politecnico di Bari

Terms of use:

(Article begins on next page)

23 January 2025



Politecnico
di Bari

LIBERATORIA PER L'ARCHIVIAZIONE DELLA TESI DI DOTTORATO

Al Magnifico Rettore
del Politecnico di Bari

Il/la sottoscritto/a **Alessandro Nettis** nato/a a **Acquaviva delle Fonti** il **28/09/1995** residente a **Acquaviva delle Fonti** in via **Luigi Pirandello, 40**, e-mail: **nettisalessandro@gmail.com**.

iscritto al 3° anno di Corso di Dottorato di Ricerca in **Rischio e Sviluppo Ambientale, Territoriale ed Edilizio**, ciclo **XXXVII**.

ed essendo stato ammesso a sostenere l'esame finale con la prevista discussione della tesi dal titolo:

“Fragility analysis of prestressed concrete bridges affected by corrosion under traffic loads”

DICHIARA

- 1) di essere consapevole che, ai sensi del D.P.R. n. 445 del 28.12.2000, le dichiarazioni mendaci, la falsità negli atti e l'uso di atti falsi sono puniti ai sensi del codice penale e delle Leggi speciali in materia, e che nel caso ricorressero dette ipotesi, decade fin dall'inizio e senza necessità di nessuna formalità dai benefici conseguenti al provvedimento emanato sulla base di tali dichiarazioni;
- 2) di essere iscritto al Corso di Dottorato di ricerca in **Rischio e Sviluppo Ambientale, Territoriale ed Edilizio**, ciclo **XXXVII**, corso attivato ai sensi del “*Regolamento dei Corsi di Dottorato di ricerca del Politecnico di Bari*”, emanato con D.R. n.286 del 01.07.2013;
- 3) di essere pienamente a conoscenza delle disposizioni contenute nel predetto Regolamento in merito alla procedura di deposito, pubblicazione e autoarchiviazione della tesi di dottorato nell'Archivio Istituzionale ad accesso aperto alla letteratura scientifica;
- 4) di essere consapevole che attraverso l'autoarchiviazione delle tesi nell'Archivio Istituzionale ad accesso aperto alla letteratura scientifica del Politecnico di Bari (IRIS-POLIBA), l'Ateneo archiverà e renderà consultabile in rete (nel rispetto della Policy di Ateneo di cui al D.R. 642 del 13.11.2015) il testo completo della tesi di dottorato, fatta salva la possibilità di sottoscrizione di apposite licenze per le relative condizioni di utilizzo (di cui al sito <http://www.creativecommons.it/Licenze>), e fatte salve, altresì, le eventuali esigenze di “embargo”, legate a strette considerazioni sulla tutelabilità e sfruttamento industriale/commerciale dei contenuti della tesi, da rappresentarsi mediante compilazione e sottoscrizione del modulo in calce (Richiesta di embargo);
- 5) che la tesi da depositare in IRIS-POLIBA, in formato digitale (PDF/A) sarà del tutto identica a quelle **consegnate**/inviata/da inviarsi ai componenti della commissione per l'esame finale e a qualsiasi altra copia depositata presso gli Uffici del Politecnico di Bari in forma cartacea o digitale, ovvero a quella da discutere in sede di esame finale, a quella da depositare, a cura dell'Ateneo, presso le Biblioteche Nazionali Centrali di Roma e Firenze e presso tutti gli

Uffici competenti per legge al momento del deposito stesso, e che di conseguenza va esclusa qualsiasi responsabilità del Politecnico di Bari per quanto riguarda eventuali errori, imprecisioni o omissioni nei contenuti della tesi;

- 6) che il contenuto e l'organizzazione della tesi è opera originale realizzata dal sottoscritto e non compromette in alcun modo i diritti di terzi, ivi compresi quelli relativi alla sicurezza dei dati personali; che pertanto il Politecnico di Bari ed i suoi funzionari sono in ogni caso esenti da responsabilità di qualsivoglia natura: civile, amministrativa e penale e saranno dal sottoscritto tenuti indenni da qualsiasi richiesta o rivendicazione da parte di terzi;
- 7) che il contenuto della tesi non infrange in alcun modo il diritto d'Autore né gli obblighi connessi alla salvaguardia di diritti morali ed economici di altri autori o di altri aventi diritto, sia per testi, immagini, foto, tabelle, o altre parti di cui la tesi è composta.

Luogo e data: Bari, 08/01/2025

Firma Alessandro Nettis

Il/La sottoscritto, con l'autoarchiviazione della propria tesi di dottorato nell'Archivio Istituzionale ad accesso aperto del Politecnico di Bari (POLIBA-IRIS), pur mantenendo su di essa tutti i diritti d'autore, morali ed economici, ai sensi della normativa vigente (Legge 633/1941 e ss.mm.ii.),

CONCEDE

- al Politecnico di Bari il permesso di trasferire l'opera su qualsiasi supporto e di convertirla in qualsiasi formato al fine di una corretta conservazione nel tempo. Il Politecnico di Bari garantisce che non verrà effettuata alcuna modifica al contenuto e alla struttura dell'opera.
- al Politecnico di Bari la possibilità di riprodurre l'opera in più di una copia per fini di sicurezza, back-up e conservazione.

Luogo e data: Bari, 08/01/2025

Firma Alessandro Nettis



D.R.S.A.T.E.

POLITECNICO DI BARI

06

Doctor in Risk And Environmental, Territorial And Building Development

2024

Coordinator: Prof. Vito Iacobellis

XXXVII CYCLE
Curriculum: Structural Engineering

DICATECh
Department of Civil, Environmental,
Building Engineering and Chemistry

Alessandro Nettis

Fragility analysis of prestressed concrete girder bridges affected by corrosion under traffic loads

Prof. Giuseppina Uva
DICATECh Department, Polytechnic University of Bari

Prof. Joan Ramon Casas Rius
Department of Civil and Environmental Engineering – Bridge Section
Universitat Politècnica de Catalunya

Dr. Andrea Nettis
DICATECh Department, Polytechnic University of Bari





D.R.S.A.T.E.

POLITECNICO DI BARI

06

Dottorato di Ricerca in Rischio e Sviluppo Ambientale, Territoriale ed Edilizio

2024

Coordinatore: Prof. Vito Iacobellis

XXXVII CICLO
Curriculum: Ingegneria Strutturale

DICATECh
Dipartimento di Ingegneria Civile,
Ambientale, del Territorio, Edile e di Chimica

Alessandro Nettis

Analisi di fragilità al carico da traffico di ponti in calcestruzzo armato precompresso soggetti a corrosione

Prof. Giuseppina Uva
Dipartimento DICATECh, Politecnico di Bari

Prof. Joan Ramon Casas Rius
Dipartimento di Ingegneria Civile e Ambientale– Sezione Ponti
Universitat Politècnica de Catalunya

Dr. Andrea Nettis
Dipartimento DICATECh, Politecnico di Bari



EXTENDED ABSTRACT

Italian and European transportation networks include a considerable number of existing bridges, built since the early '60s, characterised by simply supported prestressed-concrete (PC) girders with post-tensioned steel tendons. Corrosion of tendons, which may lead to significant loss of structural capacity, cannot be detected by simple visual inspections and requires advanced and expensive testing by bridge owner companies. Therefore, procedures aimed at risk-informed prioritisation for network-scale assessment are needed, to provide fundamental support for drawing up priority lists to be followed for an optimal allocation of resources to be employed for advanced inspections and possible retrofit. The thesis presents a study on the fragility of existing PC girder bridges considering traffic loads, accounting for corrosion-induced effects. An automated framework is proposed, aiming at the efficient probabilistic structural assessment of the investigated bridge class accounting for 1) the influence of knowledge-based uncertainty related to geometric and mechanical properties and 2) different scenarios including diverse critical corrosion levels and code-compliant traffic load models. A simplified analytical method and a refined finite element method are adopted as structure modelling strategies. To simulate corrosion effects, geometric and mechanical characteristics of prestressing steel tendons are modified by reducing the steel area and stiffness, ductility and strength properties. For analytic calculations, such modifications are integrated into a specific algorithm able to estimate variations in flexural and shear bearing capacity of critical cross-sections. In the thesis, the framework is tested with reference to a dataset of case-study superstructures with different span lengths and numbers of beams. The obtained fragility curves are deeply discussed, focusing on the corrosion effect on structural fragility and highlighting the variation of the corrosion-induced increase in fragility among the selected bridge archetypes. Although the proposed methodology presents some simplifications, it could improve the current practices of risk prioritisation, by supporting transportation authorities in ensuring the safety of the existing bridge stock.

Keywords: Prestressed-concrete bridges, post-tensioning, corrosion, traffic loads, fragility assessment.

EXTENDED ABSTRACT (ITA)

La rete infrastrutturale dei trasporti in Italia ed in Europa comprende un numero elevato di ponti esistenti, costruiti dal periodo risalente agli anni '60 in poi, la cui tipologia strutturale è caratterizzata da travi semplicemente appoggiate in calcestruzzo armato precompresso (CAP), realizzate con la tecnica della post-tensione dei cavi. Il fenomeno della corrosione agente su questi ultimi, il quale può portare ad una significativa riduzione della capacità strutturale, non può essere rilevato da semplici ispezioni visive e richiede tecniche di ispezione avanzate, e costose per i gestori di reti infrastrutturali. Di conseguenza, nasce l'esigenza di disporre di procedure basate su informazioni di rischio strutturale mirate ad individuare priorità di intervento da impiegare in valutazioni a scala territoriale. Procedure, che possano offrire un prezioso supporto per stilare liste di priorità da seguire per un'allocazione ottimale delle risorse per ispezioni speciali e, eventualmente, interventi di consolidamento. Il presente lavoro di tesi propone uno studio sulla fragilità al traffico di ponti esistenti a travata in CAP, considerando gli effetti di degrado indotti dalla corrosione dei cavi su tali strutture. La procedura proposta è automatizzata, ed ha per obiettivo un'efficace valutazione strutturale di tipo probabilistico di tale classe di ponti, considerando l'influenza delle incertezze derivanti dalla mancata conoscenza delle caratteristiche geometriche e meccaniche del sistema. Inoltre, la metodologia include la valutazione di diversi scenari di condizioni critiche di corrosione, utilizzando differenti modelli di carichi da traffico proposti dalle normative vigenti. Nella procedura vengono adottate due differenti strategie per la modellazione della struttura, una di tipo semplificato e analitica, ed una numerica più raffinata ad elementi finiti. Per simulare gli effetti della corrosione, si adottano modifiche delle proprietà geometriche e meccaniche dei cavi di precompressione in acciaio, riducendo l'area efficace dei cavi e le relative proprietà di rigidità, duttilità e resistenza. Nel caso del calcolo analitico, la capacità risultante è calcolata mediante uno specifico algoritmo in grado di stimare le variazioni della capacità flessionale e a taglio dovute alla corrosione nelle sezioni strutturali più critiche. Inoltre, si propone un'applicazione della metodologia in riferimento ad un insieme di casi studio, ovvero tipologie strutturali aventi lunghezza di

campata e numero di travi variabile. Le curve di fragilità ottenute sono ampiamente discusse, con un focus particolare sugli effetti della corrosione sulla fragilità strutturale e ponendo particolare attenzione alla variazione dell'incremento di fragilità indotto dalla corrosione tra le differenti tipologie strutturali selezionate. Sebbene la metodologia proposta presenti alcune semplificazioni, essa può potenzialmente migliorare l'attuale conoscenza sui metodi di gerarchizzazione basati sul rischio, fornendo un supporto per le autorità in ambito dei trasporti, al fine di incrementare la sicurezza del patrimonio infrastrutturale esistente.

Keywords: Ponti in calcestruzzo armato precompresso, post-tensione, corrosione, carichi da traffico, valutazione di fragilità.

CONTENTS

1	INTRODUCTION	1
1.1	Background	1
1.2	Motivation and objectives	5
1.3	Outline of the thesis.....	12
	PART I – BACKGROUND ON FRAGILITY ASSESSMENT OF CORROSION-AFFECTED PC BRIDGES	15
2	CORROSION EFFECTS ON PRESTRESSING STEEL AND CONCRETE STRUCTURAL MEMBERS	17
3	PROBABILISTIC ASSESSMENT OF DEGRADING CONCRETE BRIDGES	35
	PART II – PROPOSAL OF A METHODOLOGY FOR THE FRAGILITY ANALYSIS	47
4	WORKFLOW OF THE METHODOLOGY	49
4.1	Description of traffic load models	51
4.1.1	Eurocode traffic load model.....	51
4.1.2	Traffic load models in Italian standards	57
4.2	Modelling uncertainties of geometric and mechanical properties.....	64
4.3	Modelling strategies	65
4.3.1	Simplified structural modelling and analysis.....	65
4.3.2	FE structural modelling and analysis	67
4.4	Capacity models accounting for corrosion effects	69
4.5	Computation of fragility functions	72
5	MODELLING FLEXURAL CAPACITY CONSIDERING CORROSION EFFECTS	75
5.1	Method I: Tendon area reduction	76
5.2	Method II: Effect of modifications of steel constitutive laws	78
5.3	Validation and comparison of methods	84
6	CASE-STUDY: A SET OF ARCHETYPES OF SIMPLY SUPPORTED GIRDER-TYPE PC BRIDGES	89
6.1	Description of the typological and general features of the case-study	89
6.2	Selection of uncertain parameters and corrosion scenarios	91
6.3	Sensitivity analysis to define the size of the representative sample.....	94

7	NUMERICAL FE MODELLING OF THE ARCHETYPE-SET	97
7.1	Modelling of prestressing effects.....	97
7.2	Grillage model	101
7.3	Constitutive laws of materials.....	108
7.4	Section modelling via fibre-approach.....	110
7.5	Dead and traffic load patterns and cases	118
8	RESULTS AND DISCUSSION	127
8.1	“Corrosion-affected fragility” curves accounting for the Eurocode-based traffic model	127
8.1.1	Fragility curves via simplified analytical model fragility	127
8.1.2	Fragility curves via FE model fragility	137
8.1.3	Simplified vs FEM strategy	147
8.2	“Corrosion-affected fragility” accounting for alternative traffic models...	155
9	CONCLUSIONS	163
9.1	Summary	163
9.2	Future developments.....	165
10	ACKNOWLEDGEMENTS	169
11	LIST OF FIGURES	171
12	LIST OF TABLES	179
13	BIBLIOGRAPHY.....	181
14	CURRICULUM.....	191

1 INTRODUCTION

1.1 Background

The structural performance of existing bridges under traffic loads and natural hazards significantly affects the serviceability and safety of transportation networks, which require continuous maintenance and monitoring. For reasons related to the history and orography of the country, the infrastructure network of bridges in Italy is very extensive, varied and old, and constitutes one of the most important assets of today's society. History-wise, 1960s were an extraordinary time for the construction of free-ways in Europe. In most of European countries, the backbone of the modern freeway network was built at that time, and the same applies to Italy, when “Autostrada del Sole”, linking Milan to Rome and Naples was designed and built. With these premises, it is evident that a large portion of infrastructure in Europe has either reached or is approaching the end of its intended design life. This creates a pressing need for resources to be allocated toward structure evaluation, repair, and upgrading. Specifically, entire large groups of structures require assessment to ensure that limited resources are allocated in a logical and prioritized manner. This calls for the development of rapid assessment methods for an initial screening, followed by more detailed evaluations (with the collection of additional data as needed) for a smaller number of cases, and potentially the implementation of targeted monitoring systems in certain situations.

During the last few years in Italy, the occurrence of some collapse events, due to a various number of causes, raised the public attention on the topic, which highly affects not only the public health, but also the local and regional economy. Citing some iconic examples:

- In February 2013, the partial collapse of **Verdura viaduct**, in Sicily (Cufalo, 2013), in which no victims were involved, led to a huge economic impact on a regional scale, due to the lack of alternative roads in the area. As shown in Figure 1, the masonry arch constituting the deck fell down causing a large opening in the superstructure, preventing the traffic from crossing the bridge.

The heavy traffic was consequently transferred from a road of national importance to a winding 30 km-longer path on secondary narrow roads, leading to time wasting and increasing in costs for freight transport. Secondary roads and the related infrastructures were therefore endangered, not being designed to face such an impactful situation, with the possibility of suffering from additional dangerous problems.

- One year later, in 2014, the **Petrulla viaduct** failure (Redazione ANSA, 2016; Anania, Badalà and D’Agata, 2018) involved some injured people, but no victims. An entire span of the prestressed concrete bridge failed, breaking at the middle region of the deck (Figure 1). The following investigations blamed the collapse on poor construction work. In this case as well, one of the major consequences was on the road network of the area, very difficult to manage due to the lack of alternative paths, leading to huge difficulties for transports in the area, also defined as an “odyssey” by some local newspaper (Redazione AGRIGENTOOGGIIT, 2018).



Figure 1 – Verdura (a) and Petrulla (b) Viaduct failures, Agrigento 2014

- In October 2016, the **Annone viaduct** failure (BBC News, 2016; Di Prisco *et al.*, 2018) caused one victim. The prestress concrete girder-type bridge failed due to an exceptional transport-load passage. The reason lied in design errors on the dapped-end joint at the bearings and lack of maintenance over time, which led to a brittle failure due to shear stress at the support zone, as shown in Figure 2.

- In 2017, another failure episode of a post-tensioned **bridge in Fossano** (Fulloni, 2017), Piemonte, caused no victims and raised the attention again on construction errors. The prestressed concrete girder-type bridge suddenly collapsed without any vehicle load on the deck, only under its self-weight, due to a prestressing steel tendon problem. The failure is reported in Figure 2.



Figure 2 - Annone Viaduct (a), Lecco 2016, and Fossano Viaduct (b), Cuneo 2017

- Back in time, on 23 April 1999, near Messina, the **Santo Stefano bridge** (Caspanello, 2018) collapsed due to its self-weight. The post-tensioned 78m-span bridge had a box section and was designed in 1954 by Riccardo Morandi and built two years later, in 1956. The construction technique used for the bridge was the same as the most famous Polcevera bridge in Genoa. Fortunately, no victims were involved in the collapse.
- The **Polcevera bridge** failure, in 2018 (Calvi *et al.*, 2019), was the most tragic of these events. The bridge was designed again by Riccardo Morandi and was built between 1963 and 1967. A relevant portion of about 243 m of the bridge collapsed killing 43 people. What was left of the bridge after the tragedy is shown in Figure 3. The bridge was cable-stayed with single post-tensioned concrete stays and spans exceeding 200 m and was part of the important national road A10 managed by Autostrade per l'Italia S.p.A.. The failure was mainly caused by the high level of corrosion in the prestressed concrete stays.



Figure 3 - Polcevera Bridge failure, Genoa 2018

- Lastly, on 8 April 2020, a **viaduct** between **Albiano Magra** and Caprigliola suddenly failed, apparently under its self-weight. Although the bridge was typically used by over 2,000 vehicles per day, traffic was light that day due to the COVID-19 travel restrictions, and only two truck drivers sustained minor injuries. Under normal traffic conditions, the incident could likely have caused many casualties. According to an eyewitness who had driven across the bridge just seconds before the event, a localized, unidentified damage appeared to propagate rapidly from the Caprigliola-side abutment, triggering a progressive domino-like collapse (see Figure 4). Immediately after the event, several qualitative hypotheses were proposed regarding the causes of the bridge failure, including material degradation, foundation settlement, excessive overload, and a slow landslide on the Caprigliola slope. According to a recent work (Farneti *et al.*, 2023), the failure was actually due to the slow landslide pushing on the abutment and provoking an irreversible change in the arch shape of the adjacent span.



Figure 4 - Albiano Magra bridge collapse.

The collapse of such important existing bridges (Bazzucchi, Restuccia and Ferro, 2018), proved the elevated vulnerability of the existing bridge stock, which as seen may lead to relevant economic losses, casualties and transport disruptions affecting urban and industrial contexts.

1.2 Motivation and objectives

As a natural consequence, transportation management companies have to face one of the biggest challenges for today's society: to perform an overall bridge stock assessment, by evaluating the bridge structural performance against external actions which may be inappropriately considered in past design codes. The challenges that such environmentally exposed kind of structures need to face have also become recently more severe because of the climate effects of global warming. In this context, the number of bridges that would need a detailed assessment is very high. Given such a high number of structures, performing a refined assessment process for each specific asset would involve a significant demand of time and cost resources, as they would require appropriate onsite surveys and material test campaigns to derive reliable numerical models to be analysed under different sources of actions. Such process results

incompatible with respect to the actual resource availability and available time to carry them out.

A more eligible option for such a large-scale assessment converges in risk-informed prioritisation methodologies, as the one reported in Figure 5 by the Italian Guidelines for existing bridge assessment (Consiglio Superiore dei Lavori Pubblici (CS.LL.PP.), 2020), which allow the identification of the most risk-critical bridges to be subjected to targeted assessment and interventions (Nettis, Raffaele and Uva, 2023).

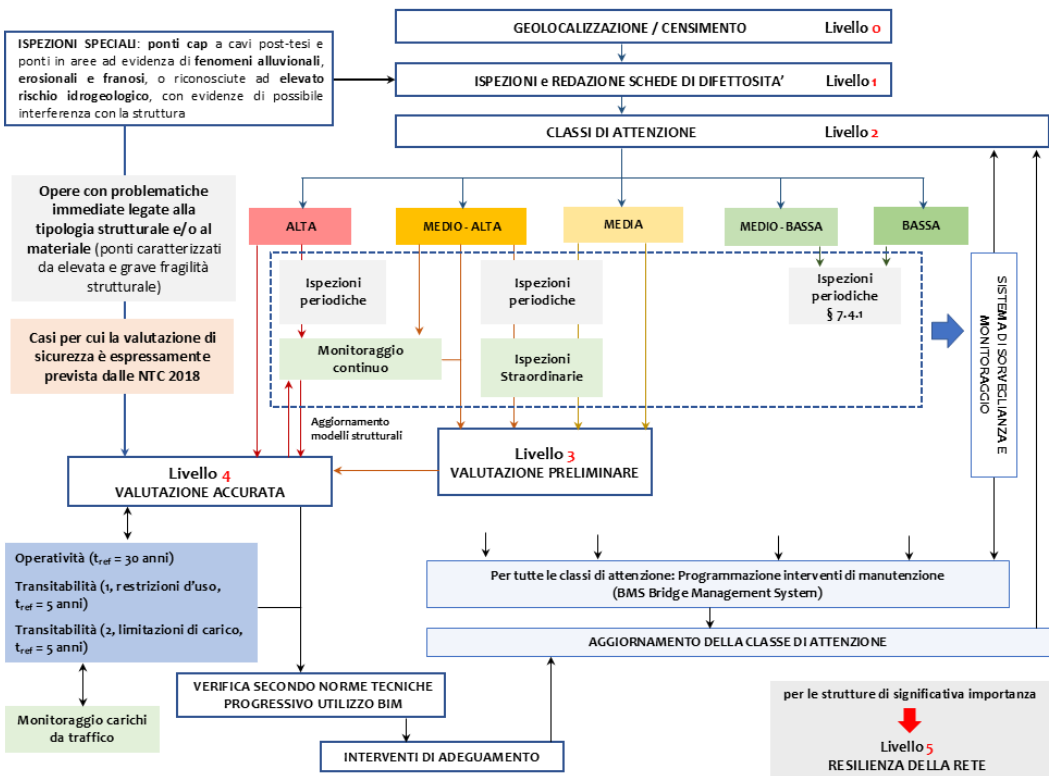


Figure 5 - Risk-based prioritisation procedure in Italian 2020 Guidelines for existing bridge assessment.

Risk-informed prioritisation is strictly related to the bridge fragility under multiple hazard sources, e.g., seismic loads, flood loads and debris flow, landslides and so on. Among those latter, a relevant source of fragility for existing bridges is represented by service traffic loads (Fiorillo and Ghosn, 2018; Miluccio *et al.*, 2021; Sangiorgio *et al.*, 2022). Current service loads are undoubtedly more severe in terms of the number

and mass of vehicles with respect to the past. Indeed, as anticipated, most of the existing bridges were designed considering old design traffic load schemes, which may be inadequate if compared to the current traffic load demand. Nevertheless, only few studies discussing the risk related to traffic loads can be currently reported in literature. Among those, Fiorillo and Ghosn (Fiorillo and Ghosn, 2018) use real field truck data to perform fragility analysis of existing bridges considering overweight traffic loads in the United States. Anitori (Anitori, 2021) developed a rational approach for determining a risk-based optimum time interval between bridge inspections. To illustrate the proposed procedure using actual bridge data, the work uses highway data from the state of New York (NYS) in the United States of America (USA) in the form of Weigh-in-Motion (WIM) truck traffic data and bridge records provided through the National Bridge Inventory (NBI) database. These data are used to develop a theoretical framework able to define the evolution of the bridge fragility and increase in risk if a bridge's inspection is deferred for a limited period of time. Miluccio et al. (Miluccio *et al.*, 2021) perform a fragility analysis of the class of existing prestressed concrete (PC) girder superstructures. They consider code-based traffic load models and use statistical distributions of significant geometric and structural variables to model the variability of structural features within the considered bridge typology. Some literature studies focus also on the time-variant reliability analysis considering traffic loads (Wang *et al.*, 2021; Zhou, Caprani and Zhang, 2021; Zhou *et al.*, 2023). For example, Zhou et al. (Zhou *et al.*, 2023) analyse the time-varying reliability of simply supported PC girder-type bridges accounting for traffic loads and concrete shrinkage and creep. In addition, Zhou et al. (Zhou, Caprani and Zhang, 2021), with their work, prove the relevant influence of maintenance works causing traffic congestion on the structural reliability of long-span bridges.

Time-variant performances play a key role in this context. As anticipated, the economically flourishing post-war period in Italy, and in some European countries as well, led to an expansion of civil infrastructure from the 1960s onwards, and hence, the construction age of many bridges dates back to these years. At this time, the technical knowledge of civil engineering about the design and construction techniques and

degradation phenomena of structures over time was much poorer than today, as well as the traffic load to which the road and infrastructure network were subjected.

As far as design and construction techniques are concerned, the prestressed concrete technique (see Figure 6) was widely adopted at that time. Prestressed concrete had been conceptualised and experimented since the late 1920s, primarily by Freyssinet. However, even highly skilled and passionate researchers and engineers such as Torroja in Spain, Dischinger in Germany, and Colonnetti in Italy encountered a major obstacle, namely, the difficulty of producing high-strength steel, which was essential for the practical use of prestressed concrete. After World War II, the situation changed rapidly, particularly in Italy. Between 1945 and 1960 several design manuals were published, and patents related to elastic coaction, cable anchoring, and other technologies were deposited or imported. Although prestressed concrete was still considered to be in its early stages, talented designers like Levi, Cestelli-Guidi, Pizzetti, Oberti, and Zorzi quickly began applying it to relatively long-span bridges (Iori and Poretti, 2009). Issues such as creep, temperature changes, strand relaxation, redistribution effects in statically indeterminate structures, and nonlinear and ultimate behaviour were initially addressed intuitively, or in some cases, overlooked. It was only years later, with the advent of specialised software, that these complex time-dependent effects could be accurately modelled. Due to this historical reason, lots of existing bridges on Italian territory belong to the prestressed concrete bridge class and are strongly influenced by the incomplete knowledge of the construction technique, and related problems, present at the time of their design.

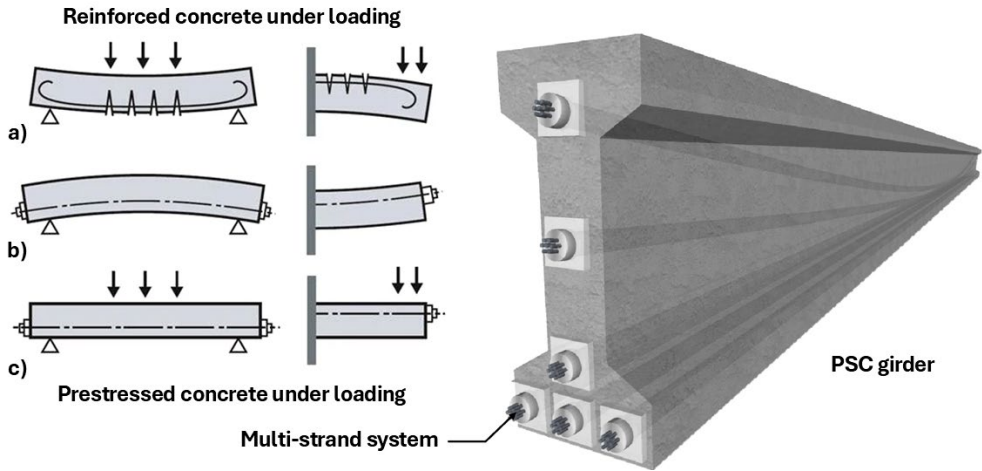


Figure 6 - Prestressed concrete (PC) basic principles, a) reinforced concrete cracked under load; b) post-tensioned concrete before loading; c) post-tensioned concrete after loading.

A fundamental hazard source to be considered while dealing with bridge intervention prioritisation is related to aggressive environmental agents involving structural degradation of bridge components (Figure 7) and increasing fragility. Besides Italy, in many European countries, existing bridges built in the post-war period exhibit severe degradation conditions caused by the combination of aggressive environmental agents and inadequate durability requirements of materials and structural details. One of the main consequences of degradation in existing bridges is the corrosion of mild steel reinforcements and prestressing steel strands or wires, which leads to capacity degradation effects for concrete girder bridges with pre-tensioned and post-tensioned steel.

Particularly, in girders characterised by post-tensioned tendons, corrosion of strands may be triggered by corrosive agents penetrating through anchorages and may be enhanced by construction errors, such as incomplete grouting causing voids in the ducts. As evidenced by some abovementioned recent collapses of bridges in Italy and more (Colajanni *et al.*, 2016; Anania, Badalà and D'Agata, 2018; Ferro *et al.*, 2022) corroded tendons in PC bridges may involve significant loss of structural capacity under gravity loads and cause structural failures.



Figure 7 - Degradation of concrete structures.

The structural assessment of such bridge typology may be quite challenging due to 1) the partial or full lack of original design data, e.g., poor knowledge of geometric and material characteristics or missing information on construction details, and 2) corrosion effects on internal tendons and presence of voids inside the ducts cannot be detected and monitored by bridge inspectors via conventional visual surveys as they are hidden within the girders and might not emerge before failure occurs. Indeed, according to the guidelines developed in Italy (Consiglio Superiore dei Lavori Pubblici (CS.LL.PP.), 2020) and earlier in the United States (FHWA - Office of Research Development and Technology, 2013), the condition rating of prestressed girders characterised by post-tensioned tendons requires advanced (also referred to as “special” in (Consiglio Superiore dei Lavori Pubblici (CS.LL.PP.), 2020)) inspections in which non-destructive and destructive non-invasive tests are used to detect voids and to identify corroded tendons inside the ducts.

Among special techniques are ultrasonic tomography, impact echo, X-rays, endoscopies, acoustic emission and others. To briefly describe some of them:

- The **tomographic investigation** is a non-destructive technique used to assess the internal condition of materials and structures by detecting defects, very useful for hidden anomalies in post-tensioned concrete such as cracks, voids and corrosion of steel tendons.
- The **impact echo technique** is an ultrasonic test method, based on the propagation of elastic waves, in the material under investigation, generated by the

impact of a metal sphere. The ultrasonic pulse propagated through the material is reflected and then detected, revealing the position of a possible internal defect, computed knowing the speed of the wave.

- **Radiographic investigation**, or X-rays, is a non-destructive diagnostic technique that allows two-dimensional images of the investigated portions to be obtained. It is based on the ionising radiation diffusion through the material, emitted by a source and absorbed by a receiver, which allows to point out the more or less absorbing discontinuities in the investigated material, revealing voids, cracks and mild and prestressing steel path.
- **Endoscopic inspection** is a semi-destructive investigation method that involves inserting a camera into the concrete element, up to the inside of steel tendon ducts, to visually inspect for corrosion or cracks.

In case more detailed investigations are needed, destructive techniques can be used such as direct surveys with visual inspections and the method of tension release for measuring the stress state of the steel tendons. Understandably, such special inspections demand a significant amount of resources in terms of time, manpower and cost and, therefore, should be appropriately targeted by risk-informed prioritisation strategies (Mazzatura *et al.*, 2023).

In addressing these issues, this PhD thesis reports a novel discussion on the probabilistic structural assessment (i.e. fragility analysis) of PC girder-type bridges subjected to traffic loads considering prestressing steel corrosion. Particularly, the simply supported PC girder-type bridge class characterised by post-tensioned tendons is analysed, characterised by wide spreading in Europe from the 1960s onwards. The study presents a methodology aimed at computing fragility curves for PC bridge superstructures subjected to gravity loads including:

- 1) The propagation of uncertainties related to structural characteristics, such as geometrical and mechanical parameters.
- 2) The potential loss in capacity due to corrosion, modelled by introducing modifications to the uncorroded prestressing steel constitutive laws.

The methodology can be used for predicting the potential increase of fragility due to increasing corrosion of prestressing steel. Unlike the existing bridge-specific methodologies involving significant modelling and analysis effort (Tu, Dong and Fang, 2019; Wang *et al.*, 2021), the presented approach is suitable for portfolio-scale applications to prioritise diagnostic campaigns (i.e. special inspections) of the prestressing steel systems and subsequent in-depth assessment. To this aim, the methodology is composed of different computation modules to be implemented in simple programming routines which allows for an extensive and automatic analysis of multiple bridges with low computational effort. Furthermore, the methodology can be implemented following two different approaches, depending on the adopted structural modelling strategy, i.e., a simplified-analytical modelling strategy and a numerical refined one.

It is worth underlining that the methodology can be applied to assess both bridge-specific or class fragility curves. For single bridges, it can be applied for investigating the increase of fragility for a given superstructure considering the potential loss of capacity due to corrosion if knowledge-based uncertainties are included. Alternatively, the procedure can be used for class fragility assessment of conventional PC bridge superstructures, if statistical distributions related to geometric parameters (e.g., span length, number of girders, deck width) are implemented.

In the case-study sections, this study reports novel outcomes on the influence of tendon corrosion on structural fragility under traffic loads of common typologies of PC girder-type bridges.

1.3 Outline of the thesis

The thesis is organised as follows:

- Part I, including Sections 2 and 3 provides a state-of-the-art on fragility assessment of prestressed concrete (PC) bridges, describing the different modelling strategies available in literature for simulating corrosion of mild reinforcement or prestressing strands in concrete bridges and presenting some studies on fragility assessment of degrading bridges.

- Section 4 describes the proposed methodology for fragility analysis, particularly taking into account simply supported girder-type post-tensioned PC bridges. Particularly concerning traffic load, Section 4.1 provides an insight into the traffic load models currently available in European standards for traffic load assessment of bridges.
- Section 5 discusses the strategy for predicting the flexural bearing capacity of PC members with corroded post-tensioned tendons providing a validation based on experimental test results (Rinaldi, Imperatore and Valente, 2010; Yu *et al.*, 2022).
- Section 6 describes the case-study, i.e., six different PC bridge superstructure archetypes, and how it is statistically processed, from the selection of variable and deterministic quantities to the sensitivity analysis performed to estimate the statistically significant sample size to be generated for analysis.
- Section 7 goes through the process of the finite element (FE) model generation, listing the modelling choices and assumptions adopted for obtaining an FE model that well represents the response of the analysed bridge typologies.
- The obtained results are deeply discussed in Section 8, highlighting their pros for risk-informed prioritisation and for addressing targeted inspections on bridges, and performing a thorough comparison between the two adopted strategies, analysing common aspects and differences.
- The entire work of this thesis together with its main achieved results is finally summarised in Section 9, providing interesting suggestions for future developments of this work.

PART I – BACKGROUND ON FRAGILITY ASSESSMENT OF CORROSION-AFFECTED PC BRIDGES

2 CORROSION EFFECTS ON PRESTRESSING STEEL AND CONCRETE STRUCTURAL MEMBERS

Corrosion in reinforced concrete (RC) structures is a physical phenomenon that mainly involves the degradation of the steel embedded in concrete members. Such a destructive mechanism concerns both RC and prestressed concrete (PC) structures, highly affecting the capacity of structures at material level first, and then involving sections and elements. The physical mechanism is described in Figure 8. The process occurs through electrochemical reactions triggered by various environmental and chemical factors, including the presence of moisture and oxygen after the de-passivation of the steel due to the presence of aggressive agents such as chlorides and carbon dioxide (CO_2). From a physical point of view, the steel wrapped by concrete is initially well protected from the external environment due to the high pH of the concrete environment, i.e., around 12-13, which creates a passive layer around the steel material. This passive layer is made of iron oxides and is stable and prevents steel corrosion from starting. Over time, CO_2 from the atmosphere can penetrate the concrete and lower its pH through a process called carbonation. This reduction in pH leads to the de-passivation of the steel, making it vulnerable to corrosion. Often coming from seawater or de-icing salts used on road pavements, chlorides can also penetrate the concrete and destroy the passive protective layer. Once this last is compromised, the steel begins to corrode through an electrochemical reaction. In a galvanic cell system, certain areas of the steel become anodic and others cathodic. In the anodic, the iron in the steel oxidizes and dissolves as ferrous ions (Fe^{2+}), releasing electrons, while in the cathodic these electrons combine with the oxygen and water to form hydroxide ions (OH^-). The freed ferrous ions (Fe^{2+}) react with the available oxygen and water, forming iron oxides and hydroxides, such as rust (Fe_2O_3). These products occupy much more volume than the original iron, causing expansion and internal pressure in concrete. These internal stresses can lead to cracking and spalling of the concrete cover (see Figure 8), further exposing the reinforcement to corrosion. This finally results in a reduction in the

structural capacity of the member section and progressive degradation over time, as the phenomenon can get worse and worse.

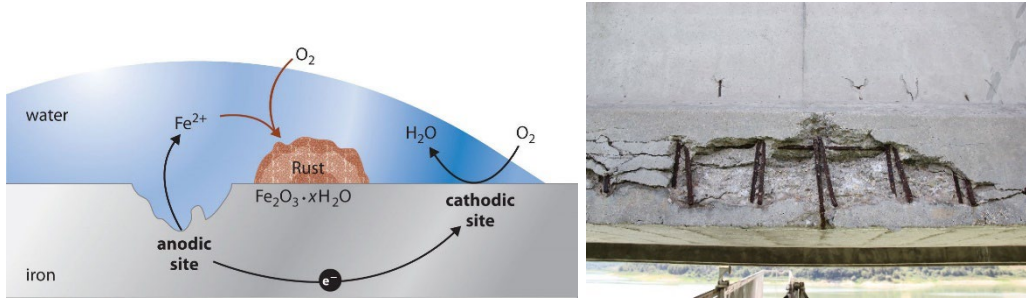


Figure 8 - Physical corrosion mechanism and result on concrete members.

To summarize, there are mainly two different sources of depassivation, i.e., carbonation and chlorides. At the same time, there can be different corrosion morphologies, as the phenomenon can be spread all over the material, i.e., uniform corrosion, or localized in little spots, i.e., pitting corrosion. The differences between the two corrosion modes are shown later in Figure 9. Usually, chloride-induced de-passivation leads to a pit morphology and can be more dangerous for structural members, as corrosion is focused and goes deep into the material, causing damage localization and localized failures of members. Basically, three different pitting corrosion modes can be identified (Franceschini *et al.*, 2022), as shown in Figure 10. At a material behaviour level, this degradation process leads to steel mass loss, i.e., reduction of steel bar area, loss of bond strength between steel and concrete, and affects the steel mechanical properties implying a decrease of stiffness, ductility and strength (Jeon *et al.*, 2019; Franceschini *et al.*, 2022; Yu *et al.*, 2022). At member level, this could be translated into load-carrying capacity and ductility reduction (Rinaldi, Imperatore and Valente, 2010; Belletti *et al.*, 2020). Particularly referring to PC structures, this can be a huge problem, as the combination of the deterioration and the stress level of the steel tendon may lead to brittle failures that occur without visual warning signs (Colajanni *et al.*, 2016; Anania, Badalà and D'Agata, 2018; Messina and Proverbio, 2023).

Given the presence of moisture and carbon dioxide in corrosion-related phenomena, the modelling of this process becomes of key importance in today's civil

engineering. A common challenge to all sciences fields of modern society concerns climate changes due to global warming. This process is strictly related to the increasing presence of CO₂ in the atmosphere and leads to an increase in temperatures and, consequently, in the presence of moisture. Indeed, hotter air raises its capacity in terms of moisture content, and the combination of these two factors, i.e., moisture and CO₂ increase, raises the probability of corrosion initiation and propagation in environmentally exposed structures. For this reason, understanding how corrosion-related phenomena evolve over time becomes of paramount importance to perform a life-cycle risk assessment of structures. In literature, there are few studies on this topic (Mortagi and Ghosh, 2022; Ge, Yang and Kim, 2023), trying to perform a life-cycle assessment of structures, considering corrosion evolution over time. Global warming makes such an assessment even more complex, as current trends in climate change must be taken into account and different evolution scenarios, from the most to the least severe, must be assumed to obtain a reliable outcome. Climate change, including higher atmospheric CO₂ levels, rising temperatures and changes in humidity, accelerates the deterioration of RC and PC structures, increasing their vulnerability to external hazards.

The corrosion process develops over time in two main stages, i.e., initiation and propagation. There are different models for corrosion processes in literature, they can be used differently depending on the objective to achieve. An interesting overview of the equations that can be used to model the corrosion process evolution and its effects on the steel material over time is reported in Ge et al. (Ge, Yang and Kim, 2023), and equations from (1) to (20) are taken from this study.

Focusing on chloride-induced corrosion, as it is the most dangerous for the abovementioned reasons, the corrosion process starts with chloride ions that from the external environment gradually diffuse through the concrete cover to the surface of the reinforcement. Corrosion begins when the chloride concentration at the reinforcement surface reaches a critical threshold. Temperature and relative humidity are the key climate-related factors that influence the chloride diffusion coefficient during the corrosion initiation phase. Considering the effects of temperature and relative humidity at a

specific site on the chloride diffusion coefficient, the corrosion initiation time t_{in} can be estimated with Equation (1).

$$t_{in} = \left\{ \frac{d_c^2}{4k_e k_c k_t D_c(t, T, RH) t_0^m} \left[erf^{-1} \left(1 - \frac{Cl_c}{Cl_s} \right) \right]^{-2} \right\}^{1/(1-m)} \quad (1)$$

In this equation, d_c is the concrete cover depth (mm); k_e is the environmental factor; k_c is the curing time correction factor; k_t is the testing method factor; $D_c(t, T, RH)$ is the adjusted chloride diffusion coefficient associated with time t , temperature T , and relative humidity RH ; t_0 is the reference time period; m is the aging factor; erf is the error function; Cl_c is the critical chloride concentration (% of binder mass); and Cl_s is the surface chloride concentration (% by mass of binder). This last parameter can be computed with Equation (2), where W/c is the water cement ratio, and A_{cs} and ε_{cs} are the regression parameter and the error term, respectively, for estimating the uncertainty of Cl_s .

$$Cl_s = A_{cs} \times W/c + \varepsilon_{cs} \quad (2)$$

In addition, the adapted chloride diffusion coefficient $D_c(t, T, RH)$, expressed in [mm²/year] can be expressed according to Equation (3).

$$D_c(t, T, RH) = D_{c,ref} F_1(t) F_2(T) F_3(RH) \quad (3)$$

In the above equation $D_{c,ref}$ is the reference chloride diffusion coefficient [mm²/year], and $F_1(t)$ is the adjustment factor at time t , that can be assumed as unit value, according to literature references (Ge, Yang and Kim, 2023). The adjustment factors $F_2(T)$ and $F_3(RH)$ associated with temperature and relative humidity can be estimated, respectively, through Equations (4) and (5).

$$F_2(T) = exp \left[\frac{U_c}{R_g} \left(\frac{1}{T_{re} + 273} - \frac{1}{T_c + 273} \right) \right] \quad (4)$$

$$F_3(RH) = exp \left[\left(1 + \frac{(1 - RH)^4}{(1 - RH_{th})} \right)^{-1} \right] \quad (5)$$

In these last two equations, U_c is the activation energy of the chloride-diffusion process [kJ/mol], R_g is the gas constant, T_{re} is the reference temperature, T_c is the current absolute temperature, and RH_{th} is the relative humidity threshold. Other factors can affect the corrosion initiation time, which need to be certainly further studied in scientific literature. Surely, the nature of the corrosion initiation process, as well as the propagation, is strongly uncertain. For this reason, one of the best ways to model the process consists of probabilistically modelling all the involved parameters, with some probabilistic distributions available in literature, and randomly generating samples of these parameters (Ge, Yang and Kim, 2023). Further research study can be done in this direction, to enhance the reliability of the data available to model the process.

After corrosion initiation, the propagation phase significantly affects the deterioration of concrete bridges, reflected in the loss of reinforcement cross-sectional area and other secondary effects. The corrosion rate is a key factor in this process. While some studies simplify it as a constant over time, some researches in literature (Li, 2003; Vidal, Castel and François, 2007) show that the corrosion rate is influenced by concrete properties, climatic variations, and changes over a bridge's service life. Thus, a proper corrosion rate model must account for time-dependent factors. The expression of the corrosion rate $r_{corr}(t)$ [mm/year] is described by Equation (6).

$$r_{corr}(t) = i_{corr}(t)f_Tf_{RH}f_{Cl} \quad \text{for } t > t_{in} \quad (6)$$

In this equation $i_{corr}(t)$ is the corrosion current density [$\mu\text{A}/\text{cm}^2$] at time t , and f_T , f_{RH} and f_{Cl} are the modification factors for temperature, relative humidity and chloride concentration, respectively, expressed in Equations (9), (10) and (11). The corrosion current density can be estimated by Equation (7), where $i_{corr,0}$ is the corrosion current density at the beginning of corrosion propagation, expressed in Equation (8).

$$i_{corr}(t) = 0.0116i_{corr,0} \cdot 0.85(t - t_{in})^{-0.29} \quad \text{for } t > t_{in} \quad (7)$$

$$i_{corr,0} = \frac{37.8(1 - W/C)^{-1.64}}{d_c} \quad (8)$$

$$f_t = \exp \left[2283 \left(\frac{1}{284.15} - \frac{1}{T_{an} + 273} \right) \right] \tag{9}$$

$$f_{RH} = \exp \left[-6000 \left(\frac{RH_{an} - 75}{100} \right)^6 \right] \tag{10}$$

$$f_{Cl} = \frac{Cl_s + Cl_c}{2Cl_c} \tag{11}$$

In these equations d_c is the concrete cover depth (mm), w/c is the water cement ratio, T_{an} is the annual average temperature [°C], RH_{an} is the annual average relative humidity and Cl_s and Cl_c are the surface and critical chloride concentrations, respectively. Such a computed rate of corrosion is decisive for the determination of the area loss of the corroded steel, both in case of uniform and pitting corrosion (Ge, Yang and Kim, 2023).

The rate of corrosion parameter r_{corr} is the key for the steel area loss model. As mentioned above, two possible corrosion mechanisms have been classified in literature, i.e., uniform and pitting corrosion. The uniform corrosion model assumes an equal and continuous area reduction around the steel element. A scheme of this type of corrosion is shown in Figure 9. The remaining cross-sectional area (mm²) of the steel element $A_{ru}(t)$ at time t can be computed through Equation (12). In this equation, D_0 is the initial diameter of the bar or strand (mm), $r_{corr}(t)$ is the time-dependent corrosion rate (mm/year) in Equation (6), and t_f is the hypothetical time at which the residual diameter of the element is reduced to zero.

$$A_{ru}(t) = \begin{cases} \frac{\pi D_0^2}{4} & \text{for } 0 \leq t \leq t_{in} \\ \frac{\pi \left(D_0 - 2 \int_{t_{in}}^t r_{corr}(t) dt \right)^2}{4} & \text{for } t_{in} \leq t \leq t_f \\ 0 & \text{for } t > t_f \end{cases} \tag{12}$$

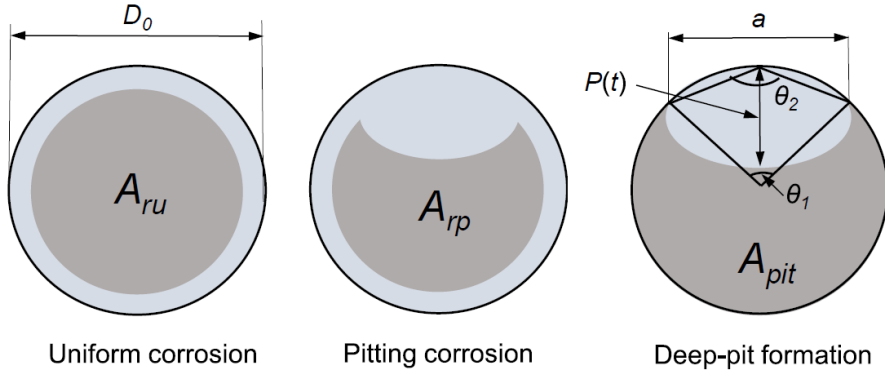


Figure 9 - Models of corrosion: uniform, pitting and deep-pitting formation (Ge, Yang and Kim, 2023).

The pitting corrosion model exposed in the following is proposed by Ghosh and Sood (Ghosh and Sood, 2016). Looking at pitting corrosion as depicted in Figure 9, the associated remaining steel element cross-sectional area $A_{rp}(t)$ (mm^2) is expressed through Equation (13), where $A_{ru}(t)$ is the time-dependent remaining cross-sectional area (mm^2) of the uniformly corroded steel element described by Equation (12), A_0 is the pristine steel element cross-sectional-area, and a is the pit width.

$$A_{rp}(t) = (A_{ru}(t) - A_0) \left(1 - \frac{a}{2D_0}\right) + A_{pit}(t) \quad (13)$$

The remaining cross-sectional area of the steel element $A_{pit}(t)$ under localized corrosion, as shown in Figure 9, is computed through Equation (14), in which the maximum pit depth $P(t)$ is expressed with Equation (15).

$$A_{pit}(t) = \begin{cases} \frac{\pi D_0^2}{4} - A_1 - A_2 & \text{for } P(t) \leq \frac{\sqrt{2}D_0}{2} \\ A_1 - A_2 & \text{for } \frac{\sqrt{2}D_0}{2} \leq P(t) \leq D_0 \\ 0 & \text{for } P(t) > D_0 \end{cases} \quad (14)$$

$$P(t) = R \int_{t_{in}}^t r_{corr}(t) dt \quad \text{for } t > t_{in} \quad (15)$$

In Equation (15), R is the ratio of the maximum to the average pit depth. All the details on the parameters a , θ_1 and θ_2 , whose geometric meaning is shown in Figure 9, can be found in Val and Melchers (Val and Melchers, 1997) and are reported in below Equations from (16) to (20).

$$A_1 = \frac{1}{2} \left[\theta_1 \left(\frac{D_0}{2} \right)^2 - a \left| \frac{D_0}{2} - \frac{P(t)^2}{D_0} \right| \right] \quad (16)$$

$$A_2 = \frac{1}{2} \left[\theta_2 P(t)^2 - a \frac{P(t)^2}{D_0} \right] \quad (17)$$

$$a = 2P(t) \sqrt{1 - \left[\frac{P(t)^2}{D_0} \right]} \quad (18)$$

$$\theta_1 = 2 \sin^{-1} \left(\frac{2a}{D_0} \right) \quad (19)$$

$$\theta_2 = 2 \sin^{-1} \left(\frac{a}{P(t)} \right) \quad (20)$$

It is worth stressing again the point that lots of parameters are involved in the determination of area loss of corroded steel elements. Statistical distribution can be adopted to model this behaviour, which is actually highly probabilistic. Different distributions are available in literature, depending on the external environment (Mortagi and Ghosh, 2022; Ge, Yang and Kim, 2023). Actually, this last concept represents a major limitation for this approach at the current state of the art, i.e., lots of assumptions need to be taken into account to perform such a probabilistic assessment. As a consequence, the corrosion rate - and, hence, all the corrosion modelling processes - is strongly dependent on these assumptions. It would be desirable for future developments to investigate these aspects more in detail, collecting more data for defining reliable statistical distributions. This would allow more reliable studies on degradation effects on environmentally exposed structures based on such a probabilistic approach.

Experimental studies for investigation on corrosion effects on prestressing steel material can be found in literature. Laboratory experimental test results on several strands extracted by naturally corroded PC beams are reported by Franceschini *et al.* (Franceschini *et al.*, 2022), who propose a corrosion-affected constitutive model. In particular, the authors proposed a modified stress-strain relationship for corroded strands, according to experimental evidence from real strands extracted from full-scale beams exposed for 10 years to chloride action from seawater. A total of 24 strand samples (4 uncorroded and 20 corroded) were analysed. Mass loss was measured and parameters like maximum pit depth and cross-sectional loss were estimated using a 3D laser scanner. Each corroded wire was classified into three different pit morphologies, shown in Figure 10.

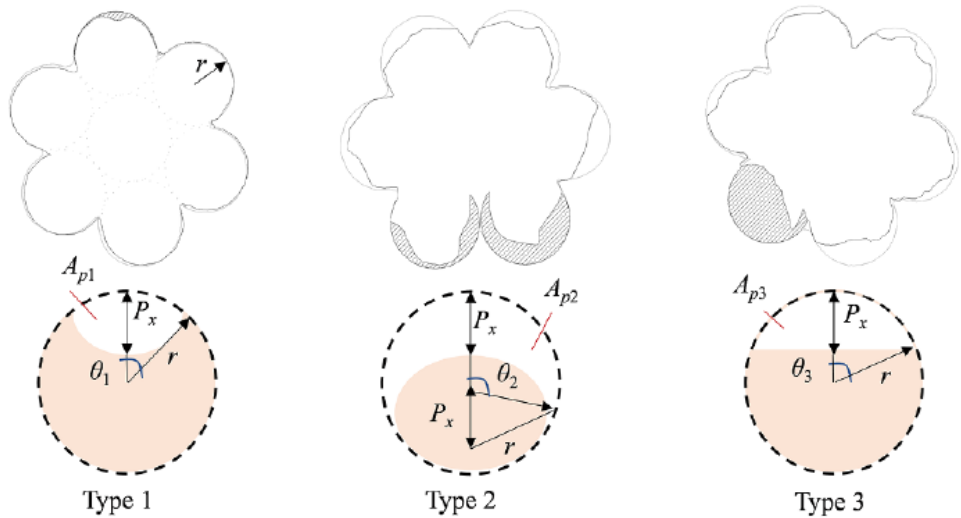


Figure 10 - Three different pit morphology (Franceschini *et al.*, 2022)

Regression analyses were performed to study how the ultimate strength and strain of the corroded strands changed with the level of corrosion. A new CPS-model for corroded strands was introduced, based on the assumption that the strand behaves like multiple springs in parallel, with failure occurring when the most corroded wire breaks. To give an idea of the corroded steel behaviour, the obtained model, i.e., CPS-model, is graphically shown below in Figure 11. It is evident that the stress-strain

relationship of the material is modified in terms of ultimate strength and ultimate strain as the steel area loss μ_{loss} , described by Equation (21), increases.

$$\mu_{loss} = \frac{A_p}{A_{outwire,0}} \tag{21}$$

In this equation, A_p is the wire area loss, experimentally measured or analytically computed, and $A_{outwire,0}$ is the uncorroded cross-sectional area of the external wire. The uncorroded steel material failed with a significant plastic deformation at the hardening stage. However, as area loss increases, the hardening phase decreases till a threshold limit characterised only by the elastic and yielding phases. This critical area loss value μ_{lim} is of key importance in modelling the corroded steel behaviour, since it governs the presence of the hardening phase and determines the ductile or brittle failure of the material. It is worth specifying that different critical cross-sectional loss leading to the loss of the hardening phase in the stress-strain curve was identified for each pit type.

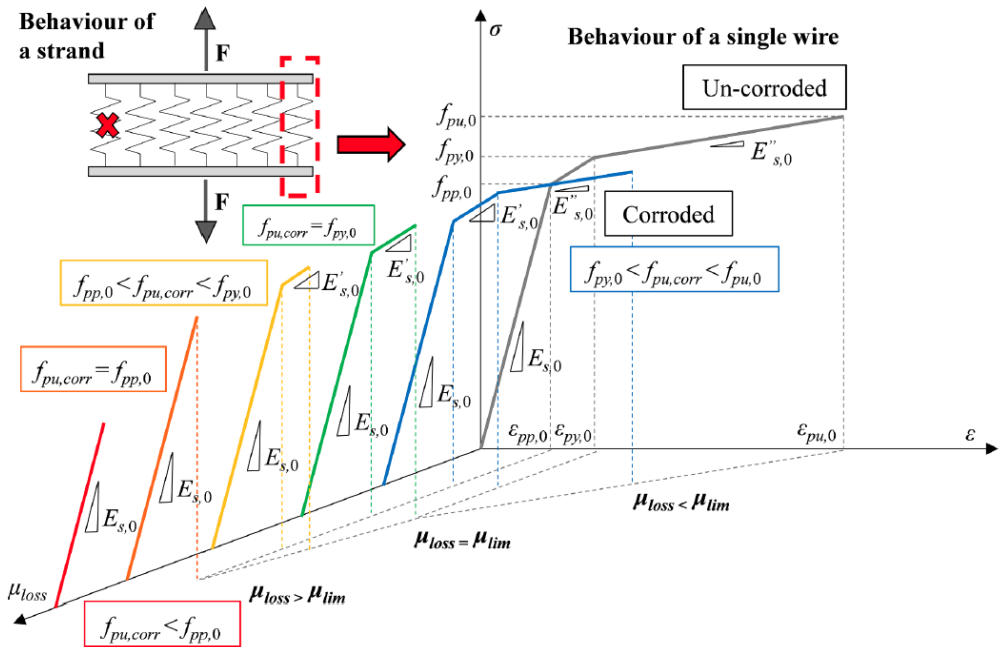


Figure 11 - Stress-strain behaviour of a corroded steel wire as a function of the cross-sectional loss (Franceschini *et al.*, 2022).

Key outcomes of the study include a database of maximum pit depth, ultimate strength, and strain in relation to mass loss and cross-sectional loss, with a new relationship between pit depth and cross-sectional loss proposed. Tensile tests showed that ultimate strength and strain depend on cross-sectional loss, and critical cross-sectional loss values μ_{lim} for three different pit morphologies were established as equal to 8.1%, 10.7%, and 5.4%. These values have key importance for the work proposed in this thesis, as will be specified in the following Section 4. Finally, an operational procedure was suggested for assessing prestressing elements in service by measuring maximum pit depth on corroded wires, enabling the application of these findings to real-world structures.

Other experimental results on this topic are shown in Yu et al. (Yu *et al.*, 2022), alongside new constitutive laws for corrosion-affected mild and prestressing steel, which are calibrated on tension tests of samples of corroded prestressing steel strands and wires. This paper investigates the deterioration of prestressing tendons and PC beams due to corrosion. In the study, the corrosion process is artificially induced. Results of the experimental tests performed on corroded strands are shown in Figure 12. It is clearly visible how corrosion, expressed in this case through a steel mass loss parameter η_s (see Equation (22), where m_0 is the mass before corrosion and m_{corr} is the mass after the corrosion process), affects the steel behaviour both in case of prestressing strands and wires.

$$\eta_s = \frac{m_0 - m_{corr}}{m_0} \quad (22)$$

As corrosion level η_s increases, ultimate strength and strain reduce, together with a slight reduction in elastic modulus for strands.

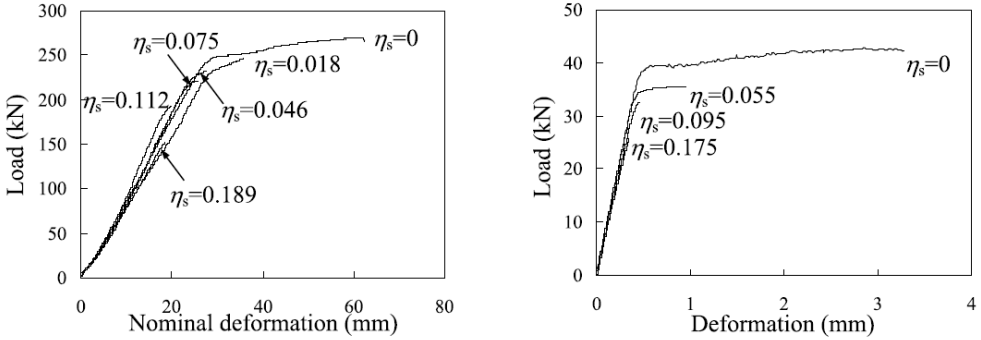


Figure 12 - Load-deformation curves of rupture tests on (a) differently corroded strands and (b) differently corroded wires (Yu *et al.*, 2022).

For the abovementioned reasons, a stress-strain relationship model like the one in Figure 13 is proposed for analytical calculations considering degradation in prestressing steel. All the parameters involved in such a simple model will be thoroughly discussed in Section 4, as this model plays a fundamental role for this thesis' purpose.

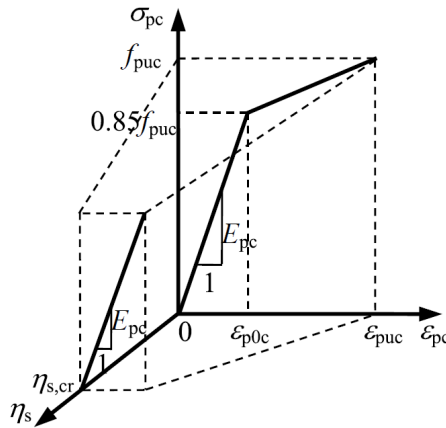


Figure 13 - Constitutive model for corroded prestressing steel (Yu *et al.*, 2022).

An analytical method was also proposed in this study, to evaluate the flexural behaviour of corroded beams. Experimental results showed that corrosion-damaged beams failed either through tendon rupture or concrete crushing, with the cracking, yield, and ultimate loads decreasing significantly as corrosion worsened. As corrosion

increased, the load-deflection behaviour of prestressed beams became similar to that of non-prestressed beams. A theoretical method for predicting the ultimate bearing capacity of beams with corroded tendons was proposed and validated using experimental data and comparison with test results taken from literature. As mentioned above, such analytical method and constitutive models can be very useful for the methodology proposed by the present thesis, thanks to their straightforwardness in application. Indeed, aiming at prioritisation on a large-scale assessment, the proposed procedure needs easy and fast modelling and analysis methods, as will be detailed in Section 4.

As far as effects of corrosion on concrete structural members are concerned, an increasing number of literature studies have been recently published regarding degradation in concrete structures, investigating both natural and artificial corrosion on mild and prestressing steel. Laboratory investigations on steel material have been carried out, as well as experimental investigations on corroded reinforced concrete and prestressed concrete members.

Focusing on corroded PC beam performance, experimental studies under natural or artificial corrosion of tendons have been developed. A significant study on artificial corrosion has been performed by Rinaldi et al. (Rinaldi, Imperatore and Valente, 2010). The researchers performed experimental tests to analyse the flexural behaviour of nine artificially corroded PC beams. The standard beam used for the test is shown in Figure 14. Prestressing is provided by 3½-inch (about 12 mm in diameter) – seven-wire strands, two placed at the bottom of the section and one at the top. The nine pre-tensioned beams (section size 200x300 mm; total length 3000 mm) were subjected to four-point bending, displacement-controlled tests in laboratory. Actually, three beams were left uncorroded and six were corroded up to a corrosion percentage level of 7%, 14% and 20%, for each strand. A comparison between the experimentally obtained results and the analytically computed bending moment resistance was also performed to test the validity of the widespread analytical model for capacity computation when in presence of corrosion.

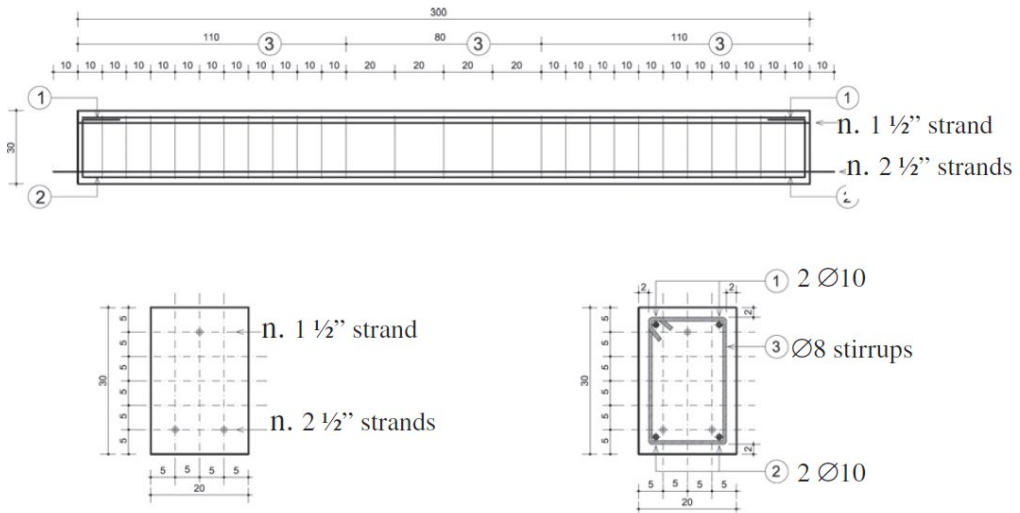


Figure 14 - Standard beam for testing (Rinaldi, Imperatore and Valente, 2010).

As clearly visible in Figure 15, the study found that corrosion of prestressed strands significantly impacts the overall performance of simply supported beams under bending, affecting both load capacity and failure modes. Unlike uncorroded beams, which fail due to concrete crushing, beams with moderate (14%) and severe (20%) corrosion levels failed because of strand rupture. Even beams with a low corrosion level (7%) exhibited reduced ductility and sudden failure due to simultaneous failure of both concrete and strands. As far as the failure for concrete crushing is concerned, the performance of uncorroded beams is clearly influenced by concrete quality, particularly with low-grade concrete, where strand slip and prestress loss were observed.

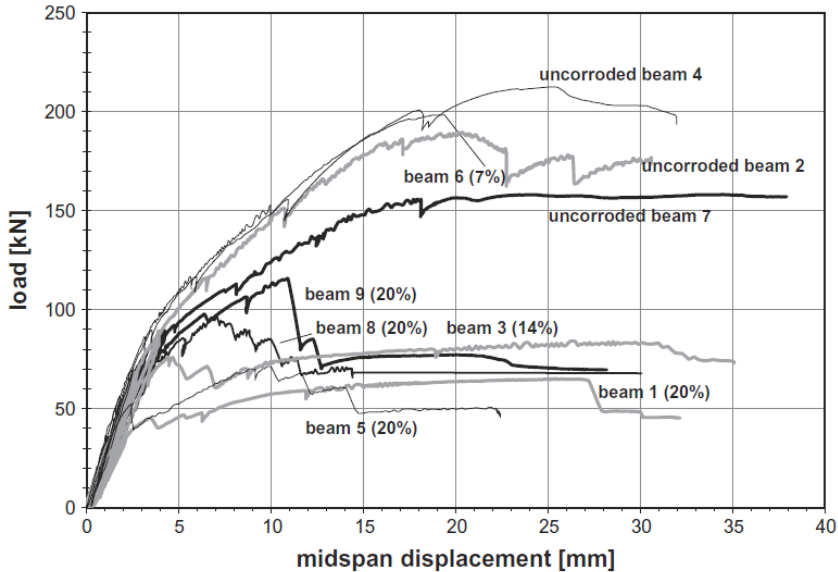


Figure 15 - Load - midspan displacement curves (Rinaldi, Imperatore and Valente, 2010)

To better understand the results, the analytical ultimate load was calculated using sectional models. As reported in Figure 16, for beams with severe corrosion, their ultimate behaviour was comparable to beams with only one strand wire and conventional reinforcement or beams with only conventional reinforcement. The analysis showed that standard methods for assessing corrosion in steel reinforcement, such as reducing the rebar diameter based on mass loss, do not apply to prestressed elements. This is because pitting corrosion causes localized stress, leading to sudden strand rupture and brittle failure. Corrosion levels over 7% mass loss alter the failure mode, and for levels around 15–20%, the ultimate load can be estimated by assuming the presence of one or two intact wires, plus conventional reinforcement.

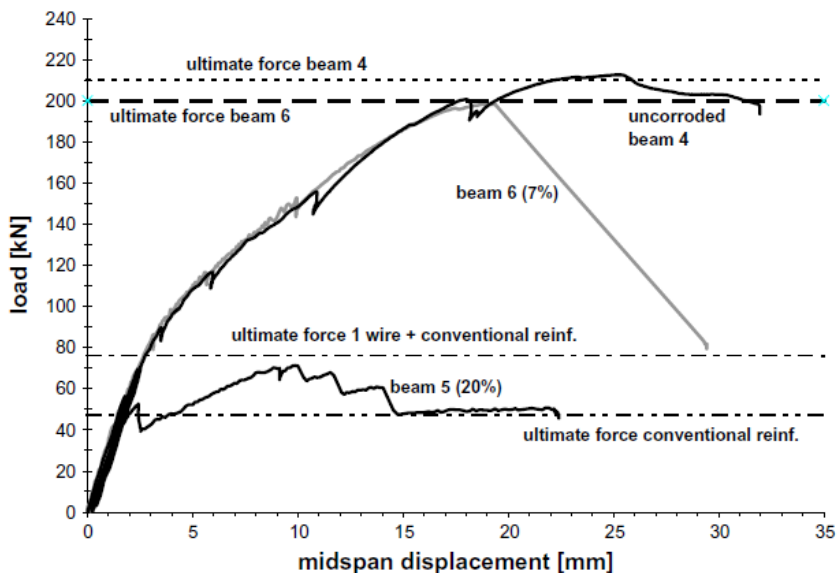


Figure 16 - Comparison between analytical ultimate force and experimental outcomes (Rinaldi, Imperatore and Valente, 2010)

As for naturally induced degradation, few studies have been provided on existing PC bridge members. An interesting experimental study on the shear behaviour of naturally corroded PC beams has been performed by Belletti et al. (Belletti *et al.*, 2020). The paper presents and discusses the results of experimental tests on seven naturally corroded PC beams and one uncorroded control beam. To investigate the effects of corrosion on shear capacity, four-point bending tests to failure were performed. Key outcomes from visual inspections, such as crack pattern maps, and also mass loss measurements, were correlated with observed shear failures and displacement measurements, to figure out some important information on shear mechanisms in presence of corrosion phenomena.

The tests led to some important conclusions. For example, the tests proved that corrosion in the strands caused strain localization and premature failure. Beams with similar shear span-to-depth ratios showed decreased shear resistance as the level of corrosion increased. The beneficial effects of prestressing on shear capacity were severely compromised by corrosion, which led to increased interaction between bending

and shear mechanisms due to the reduced tensile resistance of corroded strands. Higher corrosion levels in certain areas of the PC beams resulted in larger diagonal crack openings, negatively affecting the aggregate interlock mechanism. Lastly, this study emphasizes the importance of understanding corrosion distribution along PC members to predict the impact of strain localization on structural behaviour.

3 PROBABILISTIC ASSESSMENT OF DEGRADING CONCRETE BRIDGES

Despite the highlighted limitations associated with this approach (see Section 2), corrosion evolution models for taking into account the time-variant performance of structures have been used in literature for studies on bridge assessment to different hazards. To the author's knowledge, there is a very low number of scientific works on PC bridges at the current state-of-the-art (Wang *et al.*, 2021; Al-Mosawe, Neves and Owen, 2022), but more analyses can be found on RC bridges. Particularly, interesting studies dealing with time-variant seismic risk assessment can be pointed out (Ghosh and Sood, 2016; Mortagi and Ghosh, 2022; Ge, Yang and Kim, 2023). Among those, Ghosh *et al.* (Ghosh and Sood, 2016) present a framework for developing seismic fragility curves for ageing highway bridges, focusing on chloride-induced corrosion. The framework includes two key models: a pitting corrosion deterioration model for RC bridge columns and time-evolving capacity distributions for different damage states. A time-dependent area loss model for pitting corrosion is proposed, followed by capacity limit state distributions based on pushover analysis using the Monte Carlo method. Both pitting and uniform corrosion models are used to assess bridge fragility. Full-scale finite element models are developed for a case study of a multi-span continuous steel girder bridge subjected to corrosion. By comparing fragility curves derived from realistic pitting corrosion models with those from uniform corrosion models using traditional, time-invariant capacities, the study reveals that pitting corrosion causes a time-dependent shift in the mean and uncertainties of column capacity distributions, with fragility curves following a generalised extreme value (GEV) distribution, unlike the lognormal distribution typically assumed for uniform corrosion. The comparison also shows that uniform corrosion fragility analysis significantly overestimates the structural resilience of ageing bridges. To give a graphical idea of what kind of results can be achieved with this process, examples are shown in Figure 17 and Figure 18. Sensitivity analysis shows that factors like concrete cover depth and water-cement ratio critically affect seismic vulnerability, with smaller cover and higher

permeability, accelerating corrosion initiation and steel section loss. The study concludes by recommending the use of more realistic deterioration models for future seismic fragility assessments, suggesting these models to be extended to other critical bridge components, such as bearings. It also highlights the importance of incorporating time-varying corrosion effects into life-cycle analysis for a more accurate assessment of ageing bridges' seismic vulnerability.

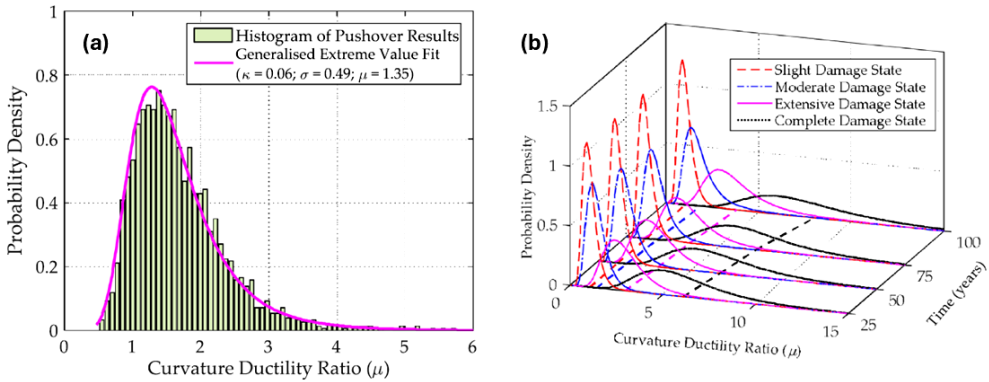


Figure 17 - (a) GEV distribution fit to 10000 column curvature ductility ratios for the moderate damage state at 75 years of pitting corrosion obtained using pushover analysis, and (b) time-evolution of capacity damage state distributions at 25, 50, 75 and 100 years of pitting corrosion. The dotted lines indicate the time-dependent changes in the mean of the fitted distributions to the different damage states (Ghosh and Sood, 2016).

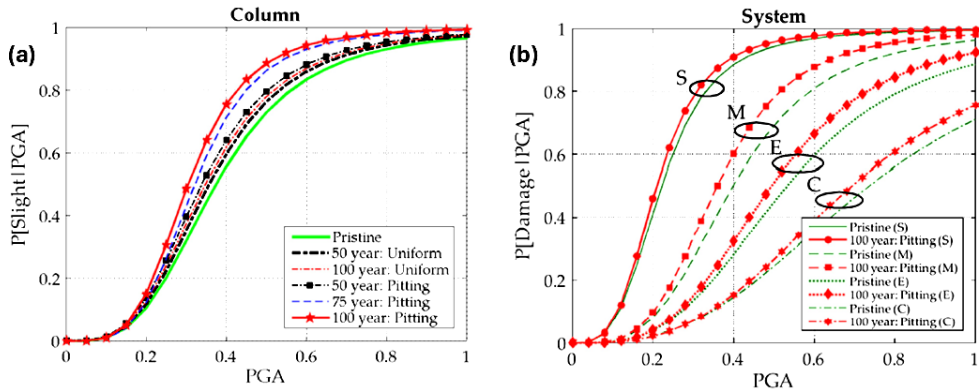


Figure 18 - Seismic fragility curves for critical bridge components, such as (a) RC columns. (b) Comparison of system level fragility curves for Slight (S), Moderate (M), Extensive (E), and Complete (C) at the end of service life (100 years) under pitting corrosion using time-evolving seismic demand and capacity models (Ghosh and Sood, 2016).

Another interesting work is the one realised by Mortagi et al. (Mortagi and Ghosh, 2022). The authors present a study on seismic loss assessment of ageing bridges. Particularly, their study proposes a framework for evaluating the lifetime seismic economic losses of ageing highway bridges, considering both future climate change effects and time-dependent chloride ingress. The study uses a realistic pitting corrosion model for RC bridge components, instead of the traditional uniform corrosion model. Climate change models from IPCC (Intergovernmental Panel on Climate Change) (*Climate Change 2013: The Physical Science Basis. Contribution of Working Group I to the Fifth Assessment Report of the Intergovernmental Panel on Climate Change*, 2013) are taken into account, downscaled from global circulation models. Climate scenarios are introduced by the notion of Representative Concentration Pathways (RCPs). According to IPCC, these are scenarios that include different time series of emissions and concentrations of the full suite of greenhouse gases or whatever chemically active gases are in the atmosphere, as well as land use or cover (IPCC, 2019). Two different RCPs are considered in the study. The full selection of scenarios includes: (a) ageing-only, which disregards any future climate change events; (b) ageing with RCP 4.5 ("moderate") climate change and lifetime chloride ingress; and ageing

with RCP 8.5 ("extreme") climate change and lifetime chloride ingress. An example of trend of annual temperature in the two IPCC scenarios is reported in Figure 19.

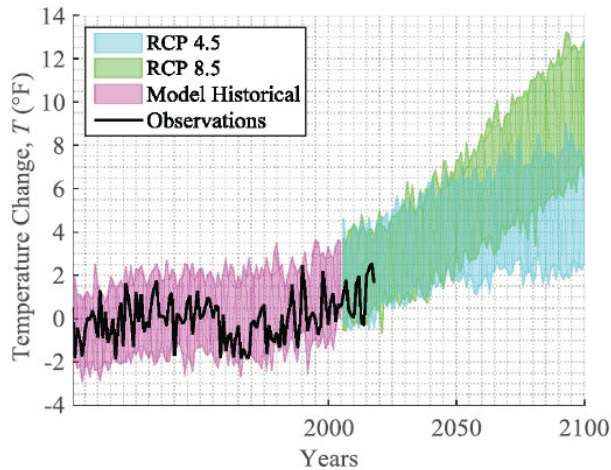


Figure 19 - Variation in annual temperature corresponding to the RCP 4.5 and RCP 8.5 scenarios for South Carolina up to the year 2100. The historical temperature model and the recorded observations of actual temperature originate from the year 1950 (Mortagi and Ghosh, 2022).

The framework integrates uncertainties related to bridge modelling, structural characteristics, deterioration parameters, climate change scenarios, seismic repair techniques, and associated repair costs. Two bridges of different typologies but having similar geometries were analysed: a multi-span continuous (MSC) steel-girder bridge and an MSC concrete-girder bridge, both located in Charleston, South Carolina. A scheme of the bridges is shown in Figure 20.

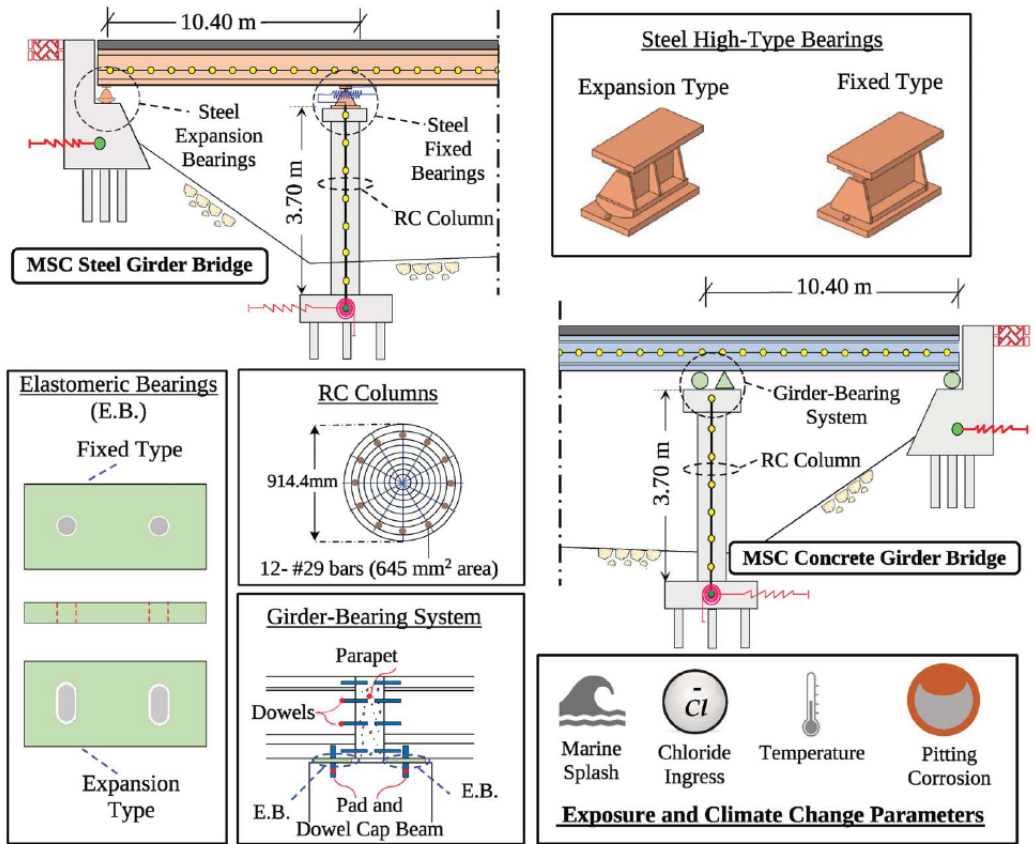


Figure 20 - A scheme of the two case-study bridges (Mortagi and Ghosh, 2022).

The paper points out key conclusions about the consideration of climate change's effects on deteriorating bridge structures. What is interesting for this thesis' objective is reported in Figure 21, where the output of the procedure in terms of fragility curve variation with different climate scenarios is shown. It is visible that climate change and chloride ingress significantly affect the seismic performance of both bridge types. Indeed, the reduction in median PGA estimates for bridge columns at 50 years of service life ranges from 17.25% to 39.89%, depending on the bridge type and the considered scenario. However, for the sake of completeness, there are other important outcomes to record. For example, analyses show that steel bridge columns are more fragile, but concrete bridge columns are more affected by ageing and climate change. Neglecting ageing and deterioration variation with different climate change scenarios

leads to underestimating seismic losses for both bridge typologies. Conclusions also highlight that seismically designed bridges are less affected by climate change than non-seismically designed ones. The whole process followed in the study emphasises the importance of explicitly considering climate change in seismic economic loss assessments of ageing bridges, as it can help decision-makers better allocate resources for structural upgrades.

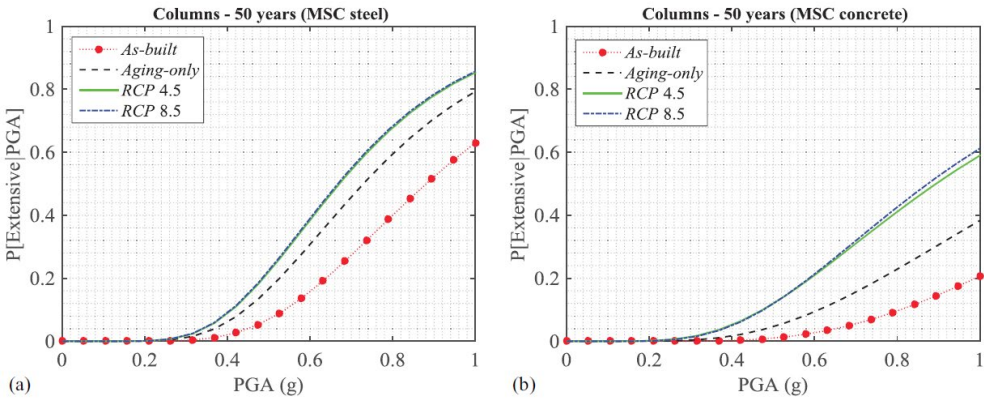


Figure 21 - Seismic fragility curves at 50 years of life for columns of (a) MSC steel bridge and (b) MSC reinforced concrete bridge (Mortagi and Ghosh, 2022).

A significant work is the one performed by Ge et al. (Ge, Yang and Kim, 2023). This paper presents an improved framework for assessing the seismic vulnerability and risk of deteriorating RC bridges. It focuses on: (a) corrosion initiation and propagation influenced by climate change, (b) time-dependent corrosion rate, (c) seismic fragility analysis using a 3D finite element (FE) model, and (d) the integration of continuous deterioration due to corrosion, climate change, earthquakes, and flood-induced scour into a time-dependent risk assessment. The framework consists of three key components:

1. Bridge deterioration prediction: this part models chloride-induced corrosion with climate change effects, incorporating variations in temperature and humidity to adjust chloride diffusion and corrosion rates. Both uniform and pitting corrosion models are considered, with and without climate change influences.

- Particularly, four deterioration scenarios are taken into account: (a) uniform corrosion without climate change (U w/o C); (b) pitting corrosion without climate change (P w/o C); (c) uniform corrosion with climate change (U w/ C); and (d) pitting corrosion with climate change (P w/ C). Climate change data are obtained from the NASA Prediction of Worldwide Energy Resources (POWER).
2. Time-dependent seismic fragility analysis: a 3D FE model of the bridge is updated at each time step to reflect corrosion initiation and propagation. Nonlinear time history analyses are then performed to generate seismic fragility curves under selected ground motion intensities.
 3. Time-dependent risk assessment: this involves predicting local scour depth due to floods based on the Hydraulic Engineering Circular (HEC)-18 guidelines and incorporating it into the FE model for a comprehensive seismic fragility assessment. The framework is demonstrated using a case study of an existing multi-span RC girder bridge, represented in Figure 22.

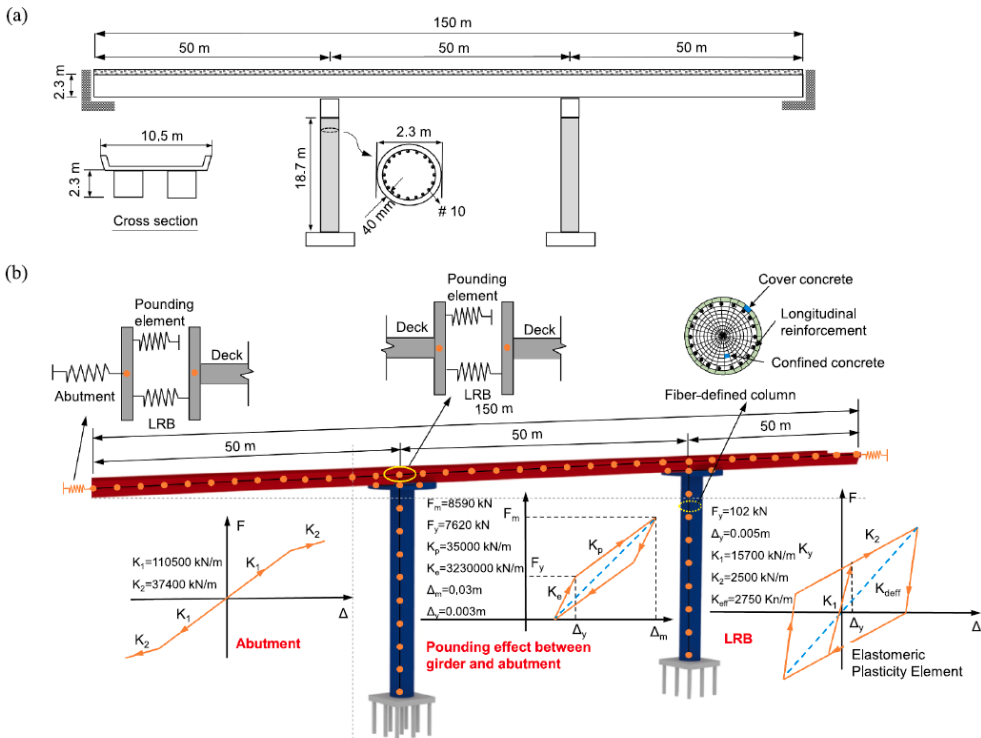


Figure 22 - Bridge modelling for case-study application (Ge, Yang and Kim, 2023)

Fragility curves obtained from the procedure are reported in Figure 23. In this figure the changes in seismic fragility at 0, 35 and 70 years are described, for each adopted limit state and for each climate change scenario assumed. The intensity measure (IM) adopted in this case-study application is the peak ground acceleration (PGA).

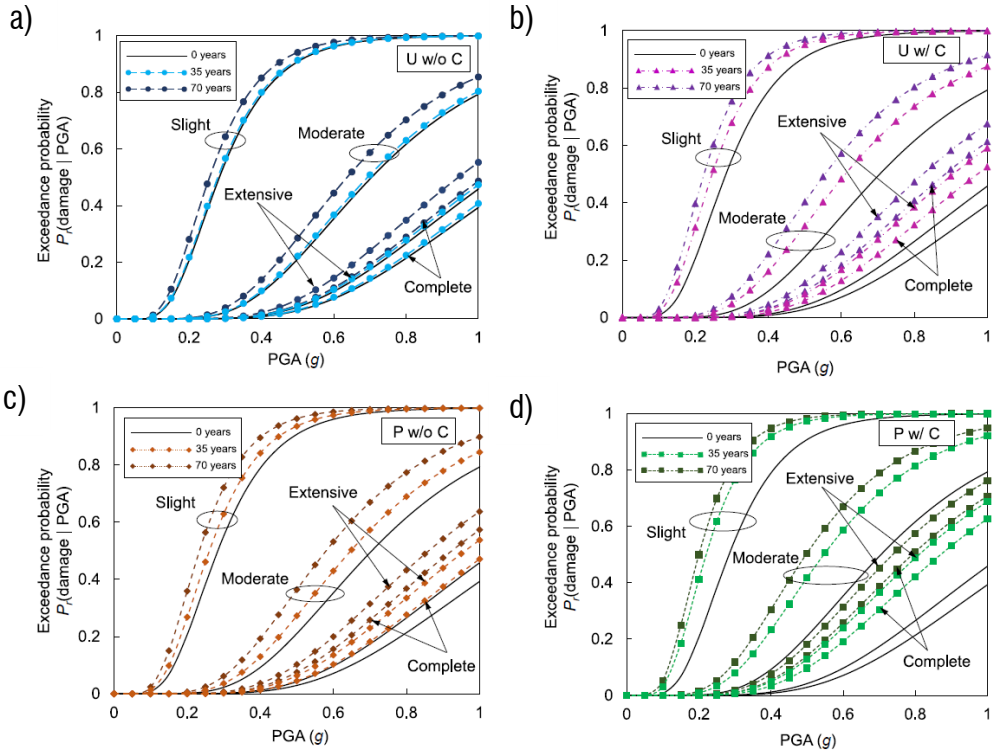


Figure 23 - Time-dependent seismic fragility curves of bridge column under four deterioration scenarios: (a) U w/o C; (b) P w/o C; (c) U w/ C; (d) P w/ C (Ge, Yang and Kim, 2023).

In the final part of the work, the authors performed also a risk analysis based on two further scenarios, i.e., with or without considering flood-induced scour. For the sake of brevity, those last results are not herein reported, as the most important outcome for this thesis' aim concerns the variation in fragility curves due to degradation effects. To conclude, the key findings of the work include:

- Climate change accelerates the initiation and propagation of corrosion, particularly in scenarios where both pitting corrosion and climate change (P w/ C) are considered. Neglecting climate change underestimates the deterioration impact on seismic performance.
- The level of structural deterioration significantly affects seismic fragility. Bridge columns with greater reinforcement loss (due to corrosion) show higher seismic demand and a greater probability of exceeding damage thresholds, with the P w/ C scenario being the most vulnerable.
- Flood-induced scour weakens the foundations, further increasing seismic fragility. Bridges in flood-prone areas under P w/ C conditions are the most vulnerable to seismic damage among all scenarios studied.
- An increase in the PGA leads to an increase in the expected risk due to the increased severity of the bridge damage. Moreover, the expected risk for the case considering the flood hazard was larger than that without considering the flood hazard under the same deterioration and seismic conditions.

Another interesting aspect of this work consists in highlighting the limitations of the corrosion evolution models currently at disposal in scientific literature. Indeed, the corrosion initiation and propagation prediction are highly dependent on the models adopted. In this particular study, the models for predicting corrosion processes were chosen based on their advantages, limitations, relevance to the work's objectives and, above all, the availability of relevant information. However, it is crucial to validate the adopted models for practical applications of corrosion evolution and, consequently, of structural degradation predictions.

Interesting literature insights on degradation evolution models applied to PC bridges, with particular reference to their superstructures, can be also pointed out. Useful information can be gathered in the work of Wang et al. (Wang *et al.*, 2021), who introduce a novel approach for assessing the time-variant reliability and redundancy of multi-girder bridges, taking into account load-carrying mechanisms due to the transverse connection of longitudinal girders, and plastic redistribution. A new system-level redundancy indicator is proposed in the study, to evaluate performance based on load

distribution and plastic redistribution among multiple girders. Most importantly, the study also investigates the negative impacts of material deterioration on structural capacity, ductility, redundancy, and load-carrying mechanisms. A detailed computational framework is developed, including an incremental nonlinear finite element analysis. The approach is validated through two full-scale destructive tests on deteriorated girder bridges, an RC and a PC bridge, showing that time-variant factors significantly influence the ultimate load-carrying capacity and reliability of ageing bridge structures.

To assess the system redundancy, three typical failure modes are identified, based on the investigation of real-world accidents of multi-girder bridges. A principal distinction can be highlighted between single-girder failure mode (SGFM) and multi-girder failure mode (MGFM). Based on the bridge design specification, the MGFM can be divided into multi-girder failure mode under elastic distribution of the load (MGFM-ED) and multi-girder failure mode by considering the plastic redistribution of the load (MGFM-PR). SGFM can happen when transverse connection fails and the load-transferring capacity of the bridge is cut off. In this case, any single girder within the system that exceeds ultimate limit states (ULS) will cause a structural failure. If the transverse connection works, the bridge is able to distribute the load among the girders according to the component stiffness, in an initial elastic stage. When the first among the beams reaches its ULS the MGFM-ED can be considered as reached and the bridge can be regarded as failed. However, the ULS of the first beam does not represent the ULS of the entire system in a girder bridge. Indeed, after that point, the deck is able to show a plastic redistribution of stresses, reaching its ULS beyond the MGFM-ED. This limit state is defined as MGFM-PR.

The output of such an assessment procedure is reported in Figure 24. As mentioned above in the previous section, the aim of showing the obtained results is to highlight how corrosion evolution modelling can affect the performance of structures over time. For this reason, there is no need to go further in detail for the whole proposed procedure in this thesis. What is important to note from Figure 24 is that the reliability of the system with respect to the three listed limit states, and, consequently, the reliability index of the entire system, is highly reduced by degradation during its service life.

Key findings of the work are that material deterioration affects both resistance and ductility of girders, reducing their capacity to redistribute loads. The used model is validated through full-scale destructive tests of two deteriorated bridges, showing strong agreement between test data and simulations. With such a validated model, the study highlights the importance of time-variant load-carrying mechanisms and redundancy in the structural reliability of ageing bridges, suggesting that these factors are crucial for designing more resilient structures and for properly assessing the existing ones.

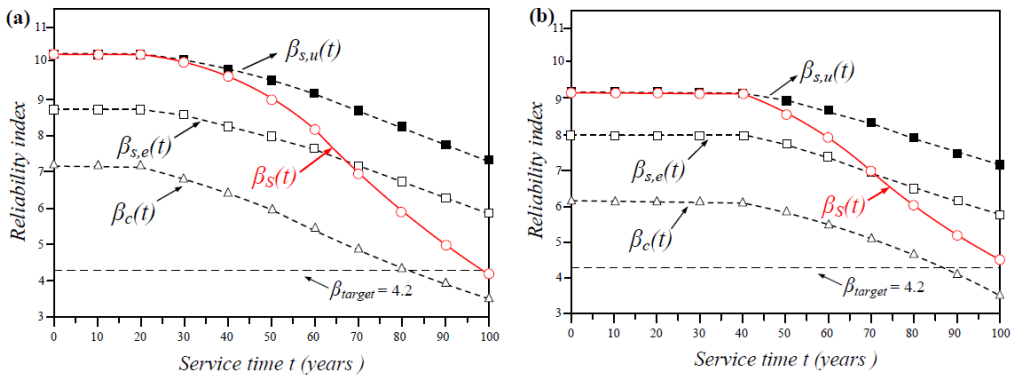


Figure 24 - Obtained time-variant reliability of the two analysed bridges (Wang *et al.*, 2021).

The last interesting reference on corrosion evolution processes on PC bridges is the work made by Al-Mosawe *et al.* (Al-Mosawe, Neves and Owen, 2022). This work is based on a slightly different model for corrosion evolution processes compared to the one exposed in Section 2. The article evaluates the reliability of the deteriorated Ynys-y-Gwas segmental post-tensioned (PT) concrete bridge, focusing on the corrosion of prestressing strands, a major cause of degradation in PT concrete bridges. The bridge is represented in Figure 25.

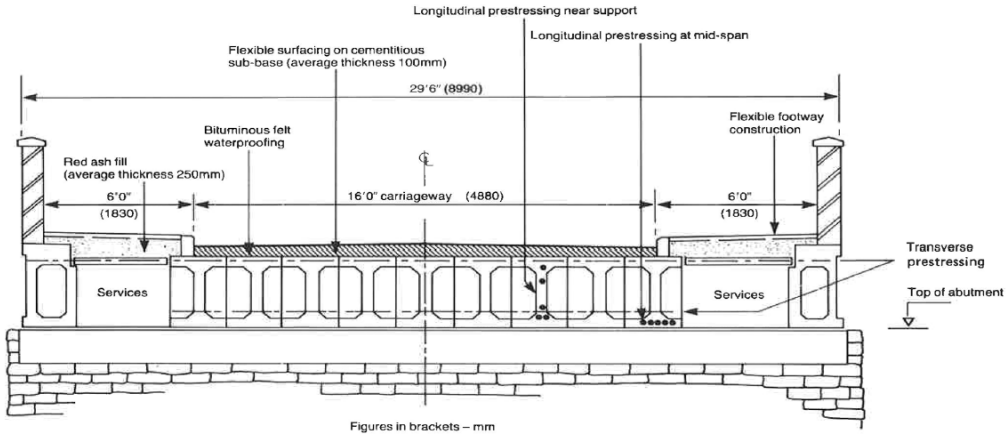


Figure 25 - Cross-section of the Ynys-y-Gwas bridge (Al-Mosawe, Neves and Owen, 2022).

A framework for assessing the reliability of existing PT bridges is developed using a three-dimensional finite element model to simulate the bridge’s nonlinear behaviour. Corrosion is modelled by reducing the strand area over time and accounting for randomly generated pit depths at beam joints.

Key findings of the work include:

- Corrosion initiation occurred early, with an estimated time of 0.773 years, suggesting that the bridge was vulnerable to corrosion soon after construction.
- Over 30 years, localized corrosion reduced the reliability index to nearly zero (0.27), indicating failure.
- Sensitivity analysis shows that corrosion significantly impacts the reliability, particularly affecting the resistance moment, while other factors remain stable.
- The importance of the knife edge load decreases with corrosion, while the resistance moment's role becomes more prominent.

Such an analysis proves that corrosion evolution modelling is key not only for predictions, but also to piece together what happens in bridge-specific failure events, learning from errors for future assessment or design procedures. Finally, it is worth mentioning that the last listed finding also plays an important role for the outcome of this thesis work, as will be seen in Section 8.

PART II – PROPOSAL OF A METHODOLOGY FOR THE FRAGILITY ANALYSIS

4 WORKFLOW OF THE METHODOLOGY

As far as refined assessment methods are concerned, different works have been proposed in literature so far, considering PC bridges subject to the hazard combination of steel corrosion and traffic loads. However, as recently highlighted by the Italian bridge issue, the need to investigate the field of large-scale assessment methods is emerging today. The aim is to identify priorities for in-depth assessment within a set of bridges to be evaluated, in order to optimise the allocation and use of the few resources available. Keeping a clear overview of the infrastructure network to which these bridges belong is key to achieving the objective.

At a first stage, at a network level, bridge classification is essential. Each bridge class, given a specific territorial context, presents different materials and exposure to external hazards and follows diverse design and construction rules. As a consequence, different suitable analysis methods exist for a generic structure belonging to a particular bridge class, as a function of its load-carrying mechanism, construction materials or even the structure limit state for which the analysis is meant to be performed. Nevertheless, in a large-scale comprehensive assessment methodology, the structural analysis may represent just one single step, while other common steps to every bridge class can be identified.

With this background, this thesis work aims at proposing and investigating the application of a large-scale fragility assessment methodology for prioritisation. It is worth mentioning that fragility assessment represents just one of the three concurrent factors (hazard, vulnerability and exposure) determining the broader concept of risk. Future statistics studies on the involved external hazards, i.e., steel corrosion and traffic loads, may lead to a more reliable risk evaluation, compared to the actual knowledge on these topics. Common steps, suitable for every bridge class, are proposed in the present methodology, e.g. uncertainties modelling or fragility curve construction method. These steps can be applied to the assessment of every kind of structure class. At the same time, to provide an application of the proposed procedure, a case-study bridge class is herein identified. For the abovementioned deeply discussed reasons,

one of the most widespread structural bridge classes over Italian territory is the simply supported, post-tensioned prestressed concrete, girder-type bridge class. The proposed methodology is suitable for this specific bridge class, but changing the structural analysis method, under data availability assumption, its use may be interestingly extended to other different bridge classes.

In this section, the proposed methodology for fragility analysis considering the involved uncertain parameters is described. It is composed of different computation modules shown in Figure 26. In the following, after a detailed discussion on the available code-compliant traffic load model adopted for the analysis, the statistical sampling technique, the simplified modelling strategy, the analysis procedure and the algorithm to achieve fragility curves are presented.

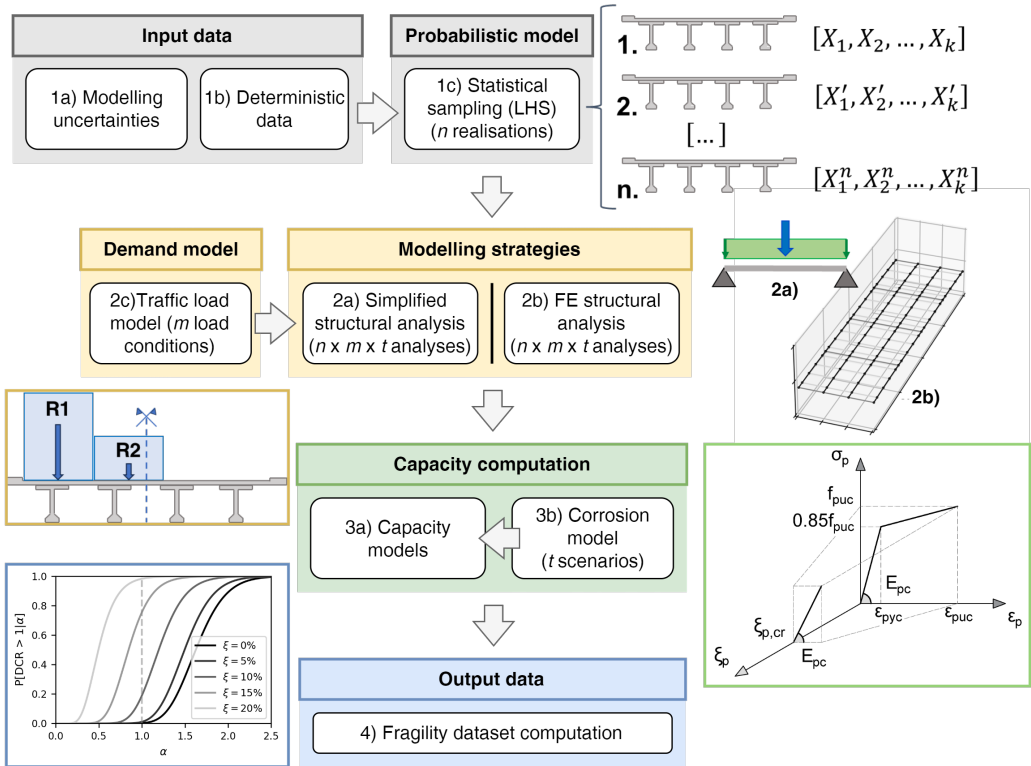


Figure 26 - Flowchart for fragility analysis.

4.1 *Description of traffic load models*

Before entering the details of the proposed methodology, it is worth presenting a discussion on the adopted traffic load models. Traffic is one of the most impactful external actions on bridges. A heavy traffic event, especially when combined with high degradation, may lead to structural failure, as clearly demonstrated by events like bridge collapses listed in Section 1.1. For this reason, when dealing with large-scale risk assessment aimed at prioritisation, traffic load actions on structures cannot be neglected. There is a strong potential in such an assessment on a regional basis, as it may constitute a powerful tool for decision-making, useful for warning of critical situations requiring traffic closures, but also load restrictions. This affects the entire road served by a critical infrastructure, and, consequently, the entire road network affected by any relative changes.

Different possibilities can be found in current standards to model the traffic action on structures, Eurocode EN1991-2 (CEN, 2003) is certainly one of the best options. As the thesis work is basically set in the Italian context, also the Italian code for construction and the Italian Guidelines for bridge assessment (Ministero delle Infrastrutture e dei Trasporti, 2018; Consiglio Superiore dei Lavori Pubblici (CS.LL.PP.), 2020) can be followed for this purpose. Finally, more advanced modelling options can be found in literature (Fiorillo and Ghosn, 2018; Iervolino *et al.*, 2023; Testa *et al.*, 2023), useful for advanced probabilistic applications.

4.1.1 *Eurocode traffic load model*

“EN 1991-2 defines models of traffic loads for the design of road bridges, footbridges and railway bridges” (CEN, 2003). Such a clear statement sets the main goal of Eurocode 1 – Part 2, which defines traffic loads on bridges on a European scale. The scope of the standards is defining imposed loads (models and representative values) associated with road traffic, pedestrian actions and rail traffic which include, when relevant, dynamic effects and centrifugal, braking and acceleration actions and actions for accidental design situations. Such actions are intended to be used for the design of

new bridges, but, at the same time, represent a fundamental reference suitable for assessment and, consequently, for this thesis' purposes.

Traffic actions on road bridges, which are of interest to the present work, consist of variable actions, which can be represented by various models. For normal conditions of use, the traffic loads should be considered as variable actions and their representative values are: characteristics or nominal values, i.e., statistical values corresponding to a limited probability of being exceeded on a bridge during its design working life, frequent values and quasi-permanent values. To give an idea, for the Traffic Load Model 1 (LM1), detailed in the following, the characteristic values represent the load intensity with a 1000-year return period for traffic on the main roads in Europe, or alternatively, the value with probability of exceedance of 5% in 50 years.

A specific bridge structure can be designed, and also assessed, for various situations. The most interesting situations coincide with the most critical, which can be different depending on each particular structure. The most critical load cases, depending on their effects on the structure, shall be identified when dealing with either design or assessment.

Eurocode defines load models that should be used for bridges with loaded length less than 200 m. It is worth mentioning that the value of 200 m corresponds to the maximum span length taken into account for the calibration of LM1 and for lengths over this value the use of such a model is safe-sided. All the proposed models and associated rules are intended to cover all normally foreseeable traffic situations. However, specific models may be defined in each National Standard for the individual project to be used for bridges equipped with appropriate means including road signs intended to strictly limit the weight of any vehicle. Indeed, in Italy, other models can be identified, proposed by the new "Guidelines for risk classification, safety assessment and structural health monitoring of existing bridges" (Consiglio Superiore dei Lavori Pubblici (CS.LL.PP.), 2020), that may be useful for this thesis' purpose and will be detailed in the following.

Traffic loads consist of cars, lorries and special vehicles. However, it is important to note that such traffic models do not describe actual loads. They have been

selected and calibrated so that their effects represent the maximum effects for a reference period of 100 years.

One of the main aspects to establish in order to apply such load models is the carriageway width. The carriageway is defined by standards like “the part of the road surface, supported by a single structure (deck, pier, etc.), which includes all physical traffic lanes (i.e., as may be marked on the road surface), hard shoulders, hard strips and marker strips”. The carriageway width, indicated as w , should be measured between kerbs or between the inner limits of vehicle restraint systems. This portion of the deck has to be divided into different notional lanes of different width, w_l . Specifically, the standards’ definition of notional lane is the following: “Strip of the carriageway, parallel to an edge of the carriageway, which [...] is deemed to carry a line of cars and/or lorries”. The width w_l of a notional lane on a carriageway and the greatest possible whole (integer) number n_l of such lanes on this carriageway are defined in standards, here reported in Table 1. The difference, where relevant, between the total area of the carriageway and the sum of the areas of the notional lanes is named remaining area.

Table 1 - Number and width of notional lanes (CEN, 2003).

Carriageway width w	Number of notional lanes	Width of a notional lane w_l	Width of the remaining area
$w < 5,4 \text{ m}$	$n_l = 1$	3 m	$w - 3 \text{ m}$
$5,4 \text{ m} \leq w < 6 \text{ m}$	$n_l = 2$	$\frac{w}{2}$	0
$6 \text{ m} \leq w$	$n_l = \text{Int}\left(\frac{w}{3}\right)$	3 m	$w - 3 \times n_l$

For each individual verification, e.g., for a verification of the ultimate limit state of resistance of a cross-section to bending moment, the number of lanes to be taken into account as loaded, their location on the carriageway and their numbering should be so chosen that the effects from the load models are the most adverse. In order to establish an order of lanes, from the most unfavourable to the least, giving the possibility to exclude the lanes whose contribution is favourable for the cross-section and

the stress under verification, Eurocode proposes a numbering system for the notional lanes on the carriageway, as shown in Figure 27. In the figure, w is the carriageway width, w_l is the notional lane width, the lanes are numbered with numbers 1, 2 and 3 and number 4 is for the remaining area. The lane giving the most unfavourable effect is numbered as Lane Number 1, the lane giving the second most unfavourable effect is numbered as Lane Number 2 and so on.

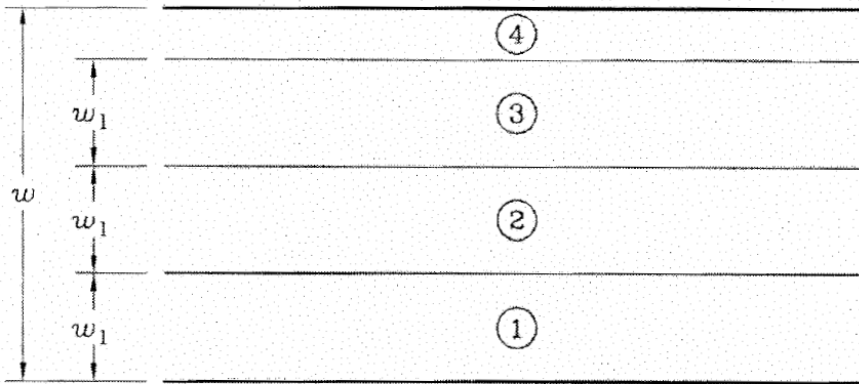


Figure 27 - Example of the Lane Numbering in the most general case (CEN, 2003).

Beyond the transversal distribution of notional lanes, also the longitudinal distribution of traffic loads is regulated by the Eurocode. Indeed, it is specified that for each individual verification, the load models, on each notional lane, should be applied on such a length and so longitudinally located that the most adverse effect is obtained. Also on the remaining area, the associated load model should be applied on such lengths and widths in order to obtain the most adverse effect.

Going into the details of the traffic load model proposed by Eurocode, it is important to note that characteristic loads, as defined above, are intended for the determination of road traffic effects associated with service and ultimate limit state verification. This latter is exactly the objective of this thesis work, as will be specified below. Citing the European standards, here are reported all the Load Models (LM) therein proposed, pointing out the most interesting for the present work.

- a) Load Model 1 (LM1): Concentrated and uniformly distributed loads, which cover most of the effects of the traffic of lorries and cars. This model should be used for general and local verifications.
- b) Load Model 2 (LM2): A single axle load applied on specific tyre contact areas which covers the dynamic effects of the normal traffic on short structural members.
- c) Load Model 3 (LM3): A set of assemblies of axle loads representing special vehicles (e.g. for industrial transport) which can travel on routes permitted for abnormal loads. It is intended for general and local verifications.
- d) Load Model 4 (LM4): A crowd loading, intended only for general verifications. It is worth mentioning what is the standards' definition of "abnormal load", that is a "vehicle load which may not be carried on a route without permission from the authority".

The LM1 is the LM to be used in this work, aiming at general verification, and for this reason, is the only one to be detailed herein. According to Eurocode, it consists of two partial systems. The first is represented by double-axle concentrated loads, also called tandem system (TS). These are defined in the standards as an "assembly of two consecutive axles considered to be simultaneously loaded". For the assessment of general effects, no more than one TS should be taken into account for each notional lane, each TS should be assumed to travel centrally along the axes of notional lanes and each axle has two identical wheels, so that the total axle weight is divided into two parts, one half for each wheel. The second system is represented by uniformly distributed loads (UDL). These should be applied only in the unfavourable parts of the influence surface, both longitudinally and transversally, as mentioned above, and on each notional lane plus the remaining area. It is worth noting that LM1 is intended to cover flowing, congested or traffic jam situations with a high percentage of heavy lorries. In general, when used with the basic values, as in this work, it covers the effects of a special vehicle of total weights equal to 600 kN. The details of LM1 are shown in Figure 28 and the basic load intensities, i.e., without taking into account the relative load amplification factors α_{Qi} and α_{qi} , are reported in Table 2.

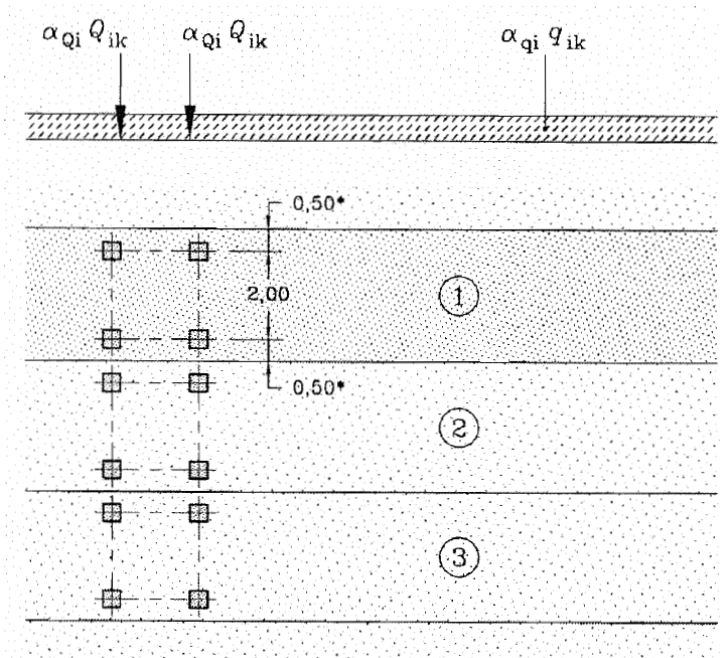


Figure 28 - Application of Load Model 1 (CEN, 2003).

Table 2 - Load Model 1: characteristic values (CEN, 2003).

Location	Tandem system TS	UDL system
	Axle loads Q_{ik} (kN)	q_{ik} or q_{rk} (kN/m ²)
Lane Number 1	300	9
Lane Number 2	200	2,5
Lane Number 3	100	2,5
Other lanes	0	2,5
Remaining area (q_{rk})	0	2,5

It is worth noting that where general and local effects can be calculated separately, the general effects may be calculated by using simplified rules, e.g. for spans greater than 10 m, each TS is replaced in each lane by a one-axle concentrated load of weight equal to the total weight of the two axles.

Finally, it is worth mentioning Load Model 3 (LM3), which is meant for defining special vehicles that, where relevant, may be taken into account for specific analyses, like the different LM proposed by Italian Guidelines.

4.1.2 Traffic load models in Italian standards

According to Eurocode (CEN, 2003), National Annexes may define alternative traffic load models. In Italy, two main standards are in force dealing with design and assessment of bridges (Ministero delle Infrastrutture e dei Trasporti, 2018; Consiglio Superiore dei Lavori Pubblici (CS.LL.PP.), 2020), and hence, proposing different traffic load models. In this subsection, the relative traffic load models are analysed.

In 2018, the Ministry of Public Transportation and Infrastructure issued the “Aggiornamento delle Norme tecniche per le costruzioni” (Ministero delle Infrastrutture e dei Trasporti, 2018), the national standards for the design and assessment of structures and infrastructures. In the fifth chapter of this document, the design rules for bridges are discussed. External actions on bridges are also reported in this section. Specifically, traffic Load Model 1 proposed by these standards, which is of interest for the present work, is exactly the same as the Eurocode. According to European standards, traffic model application rules, e.g., longitudinal and transversal placement of notional lanes in the worst combination for a specific verification, together with load shapes and intensities are taken into account in the same way as defined in the previous section. For the sake of completeness, the other traffic load models, alongside relative figures (Figure 29 and Figure 30) for a better understanding of the adopted schemes, are herein reported.

Traffic load models, including dynamic effects, are defined with the following Load Models (LM):

- a) Load Model 1: as Eurocode LM1 (see Figure 29).
- b) Load Model 2: single-axle load applied on specific rectangular-shaped tyres. The scheme is taken into account as a reference for local verification and is placed with longitudinal axis in the worst position. However, when relevant, only one wheel of 200 kN may be taken into account (see Figure 30).

- c) Load Model 3: an isolated load equal to 150 kN with rectangular shape, used for local verification on sidewalks not protected by vehicle barriers (see Figure 30).
- d) Load Model 4: an isolated load equal to 10 kN with squared shape, for local verifications on sidewalks protected by vehicle barriers and on footbridge (see Figure 30).
- e) Load Model 5: crowd loading, if relevant, should be represented by a Load Model consisting of a uniformly distributed load (which includes dynamic amplification) equal to 5 kN/m². This model should be applied on the relevant parts of the length and width of the road bridge deck, the central reservation being included where relevant. This loading system is intended for general verifications (see Figure 30).
- f) Load Models 6a, 6b, 6c: for bridge length greater than 300 m.

More details on each Load Model can be found on Italian standards (Ministero delle Infrastrutture e dei Trasporti, 2018) and are not herein reported as not of interest.

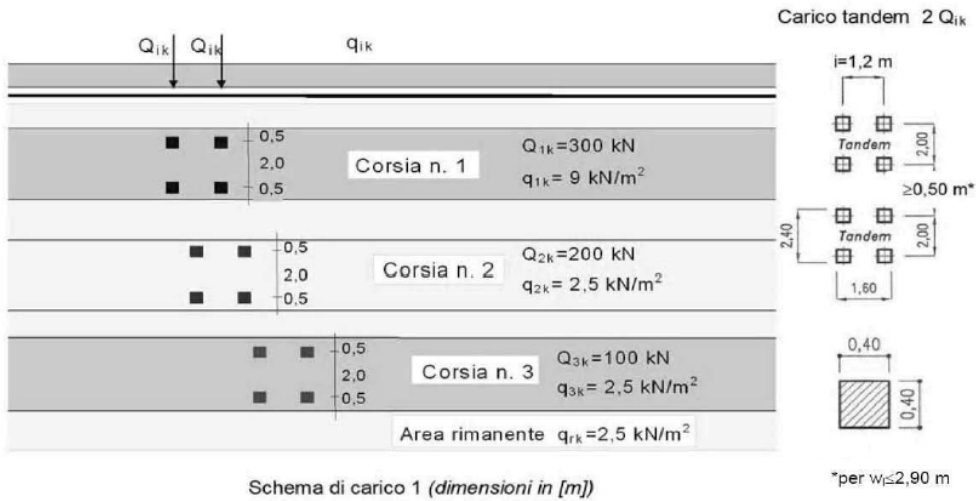


Figure 29 - Load Model 1 in Italian standards (Ministero delle Infrastrutture e dei Trasporti, 2018).

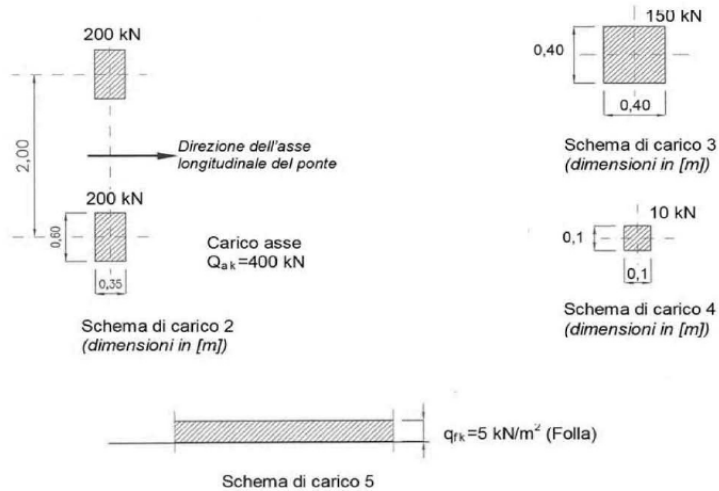


Figure 30 - Load Model 2, 3, 4 and 5 in Italian standards (Ministero delle Infrastrutture e dei Trasporti, 2018).

The Polcevera bridge failure in 2018 (Bazzucchi, Restuccia and Ferro, 2018) highlighted many weaknesses in the infrastructure management system held by Italian road managers at that time. The catastrophic event pushed the Italian government to seek solutions to the problem. As a consequence, national “Guidelines for risk classification, safety assessment and structural health monitoring of existing bridges” (Consiglio Superiore dei Lavori Pubblici (CS.LL.PP.), 2020) were issued in 2020 by the High Council of Public Works, aiming at representing a big step in this direction.

The Guidelines outline a procedure for managing the safety of existing bridges, aiming at preventing significant damage and keeping risks for bridges at acceptable levels. The document is divided into three main parts: risk assessment and classification, safety verification, and monitoring of bridges and viaducts, therein defined as “structures with a span length greater than 6.0 m”. The document presents a multi-level approach, starting from the preliminary inventory of structures to define an “attention class” that guides further detailed steps of safety verification. These preliminary classification and subsequent detailed verification provide valuable information for assessing the resilience of the entire transport network. It explains how to perform initial and special inspections and assess major risks (structural, seismic, and

hydrogeological), which are then combined into an overall classification. The guidelines provide tools to preliminarily assess the territorial status of bridges at a large scale and establish priorities for monitoring, detailed verification, and retrofit interventions. While applicable to both road and rail bridges, the document focuses on operational details for road bridges.

The use of a multi-level approach for managing existing bridges is justified by the large number of infrastructures in Italy. The complexity and, consequently, the cost of inspections, investigations, monitoring, and verifications are calibrated by assessing, even approximately and qualitatively, the actual need and urgency based on the current state of the structure. This leads to a consistent and uniform method, across different infrastructure types, for evaluating the "attention class". The proposed multi-level approach includes broad, territorial-level evaluations, such as surveys, inspections, and classifications, as well as more detailed, complex assessments focused on individual structures. Specifically, through an initial analysis of the entire infrastructure network, which includes gathering as much information as possible and conducting structured visual inspections, an "attention class" is assigned to each bridge. This classification then determines the complexity and type of any subsequent investigations that may be required, which are appropriately scaled and optimized.

An overview of the procedure is shown in Figure 5 in Section 0. The multi-level approach is developed over six levels, each with increasing depth and complexity. Briefly:

- **Level 0** involves gathering data on all structures and their main characteristics through the collection of available information and documentation.
- **Level 1**, which extends to all structures surveyed at Level 0, includes direct visual inspections and a quick assessment of the structure and the geomorphological and hydraulic characteristics of the area. This aims to identify the state of deterioration, the main structural and geometric features, and potential risks from landslides or hydrodynamic actions.

- **Level 2** establishes the "attention class" for each bridge, based on hazard, vulnerability, and exposure parameters derived from previous levels. Depending on this classification, the process moves to one of the subsequent levels.
- **Level 3** includes preliminary assessments to determine, alongside the analysis of the type and severity of the damages noted during Level 1 inspections, whether more detailed checks (Level 4) are necessary.
- **Level 4** involves detailed evaluations following the current Italian code for construction (Ministero delle Infrastrutture e dei Trasporti, 2018).
- **Level 5** (not explicitly covered in the Guidelines) applies to bridges of significant importance within the network. For these structures, more sophisticated analyses, such as resilience studies of the road network or transportation system they belong to, are recommended. This includes evaluating the bridge's relevance to transportation, its interaction with the road network, and the socio-economic impact of a potential service interruption.

As the process moves from Level 0 to Level 5, the complexity, detail, and cost of investigations and analyses increase, but the number of infrastructures involved, and the uncertainty of the results, decreases.

In Part II of Guidelines, particularly in Chapter 6, indications for level 4 assessment are provided. For such a detailed assessment, the document provides various traffic load models for different purposes. Firstly, the document states that existing bridges for which a lack of continuous and correct structural maintenance has been perpetrated over time are generally affected by numerous degradation phenomena due to environmental actions. Therefore, it is needed to carefully take into account the actual conditions of the bridge and a degradation-affected configuration for its assessment, in case of capacity reduction.

Once established that the assessment of a structural work cannot neglect the definition of its degraded configuration, the Guidelines classify the actual state of a bridge in function of its capacity to bear the demand defined by the standards. According to this classification, a bridge can be defined as:

- 1) **Adequate**, a bridge that meets the verification requirements according to the Italian code for construction (Ministero delle Infrastrutture e dei Trasporti, 2018), using the specified loads and relative partial safety factors.
- 2) **Operational**, a bridge that meets verification requirements following the principles of the Italian code but with reduced reference time for evaluating partial safety factors for loads and materials. The indicative reference time assumed in these Guidelines is 30 years.
- 3) **Serviceable**, a bridge that meets verification requirements over a short-term period during which improvement or operational works are planned and implemented, with measures such as (a) "load limitations" or (b) "restricted use of the bridge". The reference time for evaluating partial safety factors for loads and materials is further reduced, with a maximum of 5 years assumed in these Guidelines.

For the first two conditions, the adopted traffic load model, as stated above, is the same as the Italian code. For the serviceability condition, the traffic load model can be the one of Italian code, but in case of traffic limitation, a distinction between code-compliant traffic load model, i.e., from Italian code for constructions, and "Road Code" (Ministero delle Infrastrutture e dei Trasporti, 1992) traffic load model is needed. This is because any traffic limitation needs to be compatible with the Italian road code. For safety verification purposes, with a reference time of 5 years during which the minimum safety level at the ultimate limit state must still be ensured, different loads to be used with relative partial safety factors are provided. This addresses the crucial issue of operational verification of the load limitations imposed through measures defined by the Italian road code.

Four different types of serviceability levels for the Italian road code traffic load model are defined in the Guidelines, graphically shown in Figure 31, Figure 32 and Figure 33:

- 1) **Heavy vehicle serviceability**, a traffic load model considering a lorry of 5 axles with a total weight equal to 440 kN (44 t), which is a standard limitation imposed by the Italian road code. This tandem system model is combined with a

uniformly distributed load acting on the remaining part of the notional lane of intensity equal to 9 kN/m^2 , like in the notional Lane Number 1 defined in Italian code for constructions.

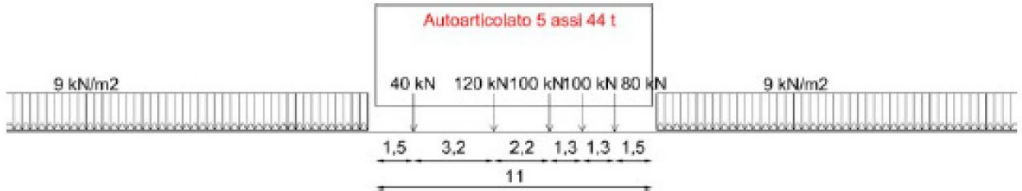


Figure 31 - Heavy traffic load model conforming to the Italian Road Code, a possible distribution (Consiglio Superiore dei Lavori Pubblici (CS.LL.PP.), 2020).

- 2) **Medium vehicle serviceability**, a traffic load model considering a lorry of 3 axles with a total weight of 260 kN (26 t), according to specific limitations of the Italian road code. The tandem system is combined again with a uniformly distributed load acting on the remaining part of the notional lane, with a lower intensity of 7.5 kN/m^2 .

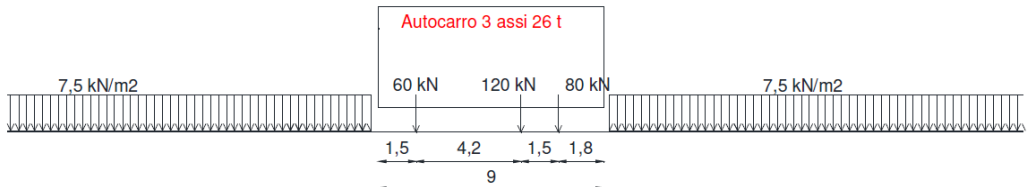


Figure 32 - Medium traffic load model conforming to the Italian Road Code, a possible distribution (Consiglio Superiore dei Lavori Pubblici (CS.LL.PP.), 2020).

- 3) **Light vehicle serviceability**, a traffic load model considering a light lorry of 2 axles with a total weight of 75 kN (7.5 t), corresponding to another specific limitation of Italian road code. This tandem system is combined with a uniformly distributed load acting on the remaining part of the notional lane with an intensity equal to 4.2 kN/m^2 .

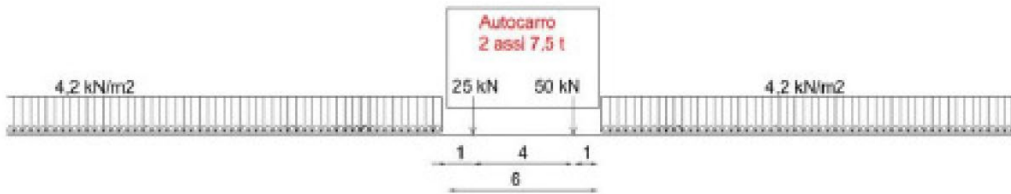


Figure 33 - Light traffic load model conforming to the Italian Road Code, a possible distribution (Consiglio Superiore dei Lavori Pubblici (CS.LL.PP.), 2020).

- 4) **Superlight vehicle** or **only-vehicles serviceability**, a simple traffic load model with a notional lane made of only uniformly distributed load with intensity of 2.5 kN/m^2 .

Such defined traffic load models apply to all open lanes, assuming a notional lane width of 3.0 m, following the current Italian building code. Additionally, if there are no physical barriers, they also extend to hard shoulders and access lanes. Loads must be placed along both carriageways in both directions of travel, longitudinally and transversally in the most unfavourable positions.

More details about the traffic load models and their applications can be found in the Guidelines. For the sake of brevity, these details are not herein fully reported, as these concepts are what strictly concerns the present thesis work.

4.2 Modelling uncertainties of geometric and mechanical properties

Geometric and mechanical parameters affecting the structural safety assessment of the investigated bridge superstructure (or a given archetype bridge, for class fragility analysis) are required as input for the proposed approach. In practical application, geometric parameters which can be accurately deduced by design blueprints or by using on-site measurements (Nettis, Saponaro and Nanna, 2020) (e.g. superstructure width and length, dimensions of structural components) can be deterministically modelled (Step 1b in Figure 26). Conversely, the determination of accurate values for geometric dimensions of components which may be difficult to inspect (e.g. slab width, beam spacing or height, beam web thickness) and mechanical parameters of materials (e.g., concrete compressive strength, ultimate and yielding tensile stress and strain of

prestressing and mild steel) would require running an appropriate diagnostic campaign based on non-destructive and destructive tests, involving inevitably additional efforts in the assessment process in terms of time and financial resources. Specifically, post-tensioned PC bridges require special inspections, as discussed in Section 1.2, to be considered as fully inspected, entailing further additional cost and time. In the proposed methodology, such unknown variables (Step 1a in Figure 26) are considered epistemic (i.e., knowledge-based (Bradley, 2010)) and aleatory uncertainties and are modelled via statistical distributions and relationships. Note that, according to Celik and Ellingwood (Celik and Ellingwood, 2010), epistemic uncertainties derive from imperfect knowledge and can be reduced by using further measurements and tests, while aleatory uncertainties represent variables (i.e., mechanical parameters of structural materials) which are inherently random in their nature. To this scope, several literature studies provide statistical distributions and regression models derived from statistical analysis for uncertain structural parameters such as prestressing and mild steel tensile strength and concrete compressive strength (Jacinto *et al.*, 2012; Zelaschi, Monteiro and Pinho, 2016; Miluccio *et al.*, 2021).

After the definition of deterministic and probabilistic variables, the Latin Hypercube Sampling (LHS) (McKay, Beckman and Conover, 1979; Iman and Conover, 1982) is used as a statistical sampling technique for the random generation of a sample of bridge model realisations (Step 1c in Figure 26). The LHS technique is applied to establish random samples of probabilistic variables to assign to each model realisation. The model realisations exhibit the same deterministic parameters, but different uncertain parameters depending on the attributed random samples. A sensitivity analysis (Silva *et al.*, 2014) can be carried out to identify a robust number of realisations for the sample to generate (e.g., see Section 6.3).

4.3 Modelling strategies

4.3.1 Simplified structural modelling and analysis

In such an assessment, which is meant to be suitable at a regional scale, simplification is key to guarantee the usability of the procedure. For this reason, following

the sampling process described in the previous section, each bridge realisation is analysed by using a simplified modelling and analysis strategy (Step 2a in Figure 26). This latter is aimed at the analytical computation of the structural demand of the beams of a bridge superstructure under a given traffic load intensity. It does not require the use of finite-element modelling and can be easily implemented in programming routines, facilitating the extensive and automatic application on multiple bridges within a given network.

The simplified modelling and analysis strategy adopted in this study is suitable for the structural assessment of a simply supported girder-type superstructure subjected to gravity loads. Particularly, the so-called Courbon-Albenga method (Albenga, 1930) is used for calculating the maximum flexure and shear demands for the girders of a given bridge grillage superstructure. This method assumes an infinite flexural stiffness of the transverse diaphragms and a negligible torsional stiffness of the girders and, therefore, results appropriate for bridge superstructures exhibiting a high length/width ratio, which is a common geometric characteristic of existing roadway bridges. Under these hypotheses and regardless of the position of the diaphragms, the transverse distribution of a given load on the deck among the different girders can be analytically simulated by using distribution coefficients depending only on the number and position of the girders. Although simplified, the proposed approach induces a conservative estimate in terms of stress demand with respect to a refined numerical modelling strategy which accurately accounts for the hyperstatic effects related to the transverse load distribution (e.g., (Messina and Proverbio, 2023)). For bridges not reflecting the abovementioned applicability assumptions of the method, such as continuous decks or with beams whose torsional stiffness is not negligible or even bridges without diaphragms, a numerical model should be used to predict the stress distributions in girders under traffic loads.

Gravity loads in terms of self-weight of the bridge elements and non-structural components are simulated by using uniformly distributed loads. Traffic loads (Step 2c in Figure 26) are modelled by adopting the load schemes (Table 2 in Section 4.1.1) provided by Eurocode 1 – Part 2 (CEN, 2003), which is the same as in the Italian

building code “Norme Tecniche per le Costruzioni 2018” (Ministero delle Infrastrutture e dei Trasporti, 2018), as deeply discussed in Section 4.1. For each model realisation, the demand parameters extracted from the analysis are the maximum bending moment $M_{D,mid}$, recorded at mid-span, and the maximum shear demand $V_{D,sup}$, recorded at the support, for the edge girder. The number and arrangement of loaded traffic lanes to be considered in the analysis and the tandem load position along the deck are defined according to the code-prescribed position, i.e., in such a way as to maximise the flexural and shear demand for the edge girder. To this scope, the traffic lanes are located adjacent to the kerb (as shown in Figure 38 in Section 6.1). Only the traffic lanes giving an unfavourable stress contribution to the edge girder are considered in the analysis. No variability in the lateral position of the traffic lanes with respect to the deck longitudinal axis is considered. The tandem load system is assumed acting alternatively at the mid-span and at the support cross-sections to determine $M_{D,mid}$ and $V_{D,sup}$, respectively. Once gravity and traffic loads are modelled, their contributions on the edge girder are computed through the Courbon-Albenga method and a pair of $M_{D,mid}$, $V_{D,sup}$ is retrieved for each model realisation.

4.3.2 FE structural modelling and analysis

Simplified modelling allows for very fast analyses, which are essential for large-scale assessment. However, it is important that such analyses provide an effective and reliable result as well. Greater reliability is certainly provided by numerical finite element (FE) models, which can capture the effects of load redistribution between structural members. To perform more reliable analyses and to compare them with the analyses produced by simplified modelling, a suitable finite element (FE) model can be adopted for the class of simply supported girder-type PC bridges (Step 2b in Figure 26). To realise such a model is obviously much more complex in terms of computational effort, from the global and local geometry to the definition of materials, loads and gravity analyses.

To best represent the characteristics of this structural typology, and at the same time try to mitigate the analysis computational costs, a plane grillage model is adopted

in this study, with beams, diaphragms and slabs represented by linear and non-linear beam elements. In particular, one-dimensional non-linear elements and section fibre modelling are chosen to model beams and diaphragms, while the slab contribution is modelled separately according to the considered direction, i.e., transverse or longitudinal. As for the longitudinal contribution, the slab is merged into the longitudinal beam section, by modelling a composite section for the generic one-dimensional beam member. As for the transverse direction, one-dimensional linear elastic elements are adopted to model the relative slab contribution. The modelling choices to be considered for the definition of such a model are much more and more complex than the modelling process described in the previous section and are discussed more in detail in section 7. However, it is worth specifying that, for the sake of comparison with the previous method, the adopted model is only suitable for the class of PC bridges assessed in this thesis.

Such a model allows the equations governing the structural analysis problem to be solved without being constrained to the strong assumptions, and therefore limitations, associated with the Courbon-Albenga method, which is needed in the simplified case described in the previous section. As a consequence, through an FE model, it is possible to extend the evaluation to bridges that do not meet the assumptions of the Courbon-Albenga method, i.e. bridges with a low length-to-width ratio or bridges without diaphragms.

Even more important is to emphasise the possibility provided by the FE modelling strategy to realise a non-linear type model, capable of also capturing the plastic response of the structure, both at the level of the individual element and at the global level of the entire structure, which presents a stresses redistribution capacity that goes beyond the achievement of the ultimate limit state of the most stressed element. This allows the response of the structure to be recorded in its completeness, guaranteeing a more accurate and truthful evaluation.

The modelling of the gravitational loads, i.e., self-weights and traffic loads, will also be dealt with more in detail in the following. As for traffic load models, the schemes

proposed by the Eurocode 1 – Part 2 (CEN, 2003) and by Italian Guidelines (Consiglio Superiore dei Lavori Pubblici (CS.LL.PP.), 2020) are adopted.

These loads are applied to the structure using a “push-down” displacement-control numerical procedure, which allows recording the plastic response of the structure, whose non-linear elements exhibit a certain ductility before reaching complete failure. The analysis basically consists of gradually pushing the structure with the previously defined load system in several steps, monitoring the vertical displacement of a selected control node. The amplitude of each step can be decided and determines the accuracy and computational effort of each analysis. At the end of each step, the strain and stress characteristics of the materials can be monitored in each defined section, including critical forces like $M_{D,mid}$ at midspan and $V_{D,sup}$ at the support zone of the most loaded beam.

4.4 Capacity models accounting for corrosion effects

For each model realisation, the demand parameters for flexure and shear ($M_{D,mid}$ and $V_{D,sup}$), calculated as above, are compared with the corresponding capacity ($M_{C,mid}$ and $V_{C,sup}$, Step 3a in Figure 26). Regarding shear capacity $V_{C,sup}$ at support zones, the same analytical formulation, reported in Equation (24), is adopted for the two different modelling strategies. Differently, for computing flexure capacity $M_{C,mid}$ at the generic beam middle section, the computational approach adopted by the two modelling strategies differs substantially, although achieving consistent numerical results.

An analytical model, through a more or less complex algorithm, which is detailed in Section 5.2 and graphically described in Figure 36, is adopted for computing the flexural capacity of a generic beam for the simplified strategy. The algorithm basically consists of solving the translational and rotational equilibrium equations for the analysed cross-section in either concrete crushing or tendon rupture conditions.

On the other hand, the refined fibre model of the numerical strategy allows for monitoring the stress or strain state of each fibre of a generic cross-section belonging to any structural member. For this reason, in the FE model, the attainment of the ultimate

flexural capacity of a generic beam is achieved when the first fibre of any cross-section fails during the analysis, reaching its ultimate strain value. Hence, the flexural capacity $M_{C,mid}$ for the generic cross-section of the beam equals the bending moment demand corresponding to the step at which the fibre failure occurs.

Several corrosion scenarios are assumed to estimate the influence of corrosion on capacity (Step 3b in Figure 26). From a physical point of view, as deeply discussed in Section 2, the phenomenon of corrosion affects steel properties, reducing its mass, stiffness, strength and deformability. To model corrosion effects, a parameter ξ is defined via Equation (23), as the equivalent percentage reduction of the corroded steel area, i.e., the ratio between the loss of corroded steel area during the corrosion process and the initial area of non-corroded steel.

$$\xi = \frac{\Delta A_c}{A_0} = \frac{A_0 - A_c}{A_0} \quad (23)$$

This parameter appropriately summarizes corrosion effects and can be related analytically to steel geometric and mechanical properties modification. For this reason, in the present procedure, flexure and shear capacity are computed considering given percentages ξ of corroded tendon area in the related critical sections. In particular, the flexure capacity modelling ($M_{C,mid}$) is carried out considering the residual steel area and the corrosion-induced effects on the constitutive law (i.e. reduction of the elastic modulus and ultimate strength and deformation). Details and equations are extensively reported in Section 5, together with a validation of the adopted procedure.

Regarding the shear capacity ($V_{C,sup}$), the computation follows the study proposed by Miluccio et al. (Miluccio *et al.*, 2021), where three different shear capacity models recommended by the Eurocode (GEN, 2004) were tested. The first can be used for RC beams in a cracked configuration with a low amount of shear reinforcements; the second model applies for PC beams in uncracked configuration considering the prestressing contributions; the third model suits for cracked RC beams considering a strut-and-tie resisting mechanism. In (Miluccio *et al.*, 2021), the second shear modelling strategy, which is also currently used in the Italian building code (Ministero delle

Infrastrutture e dei Trasporti, 2018), turned out to be the most accurate for PC simply supported girder bridges assuming that shear cracks are absent at the beam supports, and is used herein for the proposed procedure. Particularly, the shear capacity V_R is computed through Equation (24), in which b_w is the girder web width; J is the second moment of area; S_{x_G} is the first moment of area above and about the centroidal axis; f_{ct} is the concrete tensile strength; σ_{cp} is the average compressive concrete stress due to residual prestressing action σ_{sp} .

$$V_R = \frac{J}{S_{x_G}} b_w \sqrt{f_{ct}^2 + \sigma_{cp} f_{ct}} \quad (24)$$

Other advanced formulations for shear strength computation can be adopted (Park, Kang and Choi, 2013) without compromising the efficiency of the presented procedure. It is worth noting that, by modelling shear capacity through Equation (24), the real distribution of tendons in the beam section at the support zone is neglected. In fact, the effect of post-tensioning compression stress is taken into account only through σ_{cp} term, i.e., the sectional average compressive concrete stress, which decreases by increasing the corrosion level of steel tendons. Finally, it is also important to point out that the beneficial counter-shear contribution provided by the uplift of the prestressing tendons in the PC-beam supports is neglected in this procedure. This leads to a conservative shear response evaluation, which is important to keep in mind for the conclusions drawn in Section 8. However, such a beneficial contribution in most cases turns out to be so small compared to shear demand at the ultimate limit state, which is the objective of this assessment procedure, that it can be neglected without producing big errors in practical evaluations. Besides, the adopted simplified formulation is suitable for the application of the proposed framework on PC girder bridges characterised by an uncertain tendon layout at the supports. This is a common issue in the absence of detailed blueprints and surveys based on advanced non-destructive scanning technologies aimed at detecting the tendon layout. Note that to reduce the inaccuracies associated with this latter approximation, a parabolic tendon distribution

equivalent to the actual tendon distribution could be used in future developments of the methodology.

At the current stage of development, as in previous studies (Kim and Song, 2021), fatigue failures are not accounted for in the present methodology. Note that corrosion induces a reduction in cross-section tendon area, and it can also embrittle the response of the prestressing steel, mainly in the pits of the wires, leading to increasing stress variation and consequent potential fatigue failures under load cycles. Therefore, with the increasing corrosion influence, the fatigue-corrosion interaction should be considered through time-variant reliability analyses to estimate variations of the failure probability over time and the structure residual service life (depending on the expected future evolution of both corrosion and traffic load cycles) (Su *et al.*, 2022; Guo *et al.*, 2024).

4.5 Computation of fragility functions

The last step of the proposed procedure consists of the evaluation of bridge fragility, by developing fragility curves expressing the probability of failure for a given intensity of traffic loads (Step 4 in Figure 26). The failure can be achieved for either flexure or shear demand exceeding the corresponding capacity. To compute fragility curves, an approach based on the multi-stripe seismic fragility analysis method proposed by Baker (Baker, 2015) is adopted.

First, a given corrosion scenario (ξ) is assumed and the capacity values $M_{C,mid}$ and $V_{C,sup}$ for the edge girder are computed for each model realisation. Subsequently, each of the N bridge model realisations generated is analysed considering an increasing intensity value of the traffic load scheme which adds to the gravity load due to structural and non-structural components. For this purpose, a set of M load schemes is defined, in which the magnitude of the adopted traffic load model (Section 4.3.1) is multiplied by a factor α which is used as load intensity measure (IM) for the fragility analysis. The factor α ranges from 0 to an upper limit which should be calibrated to achieve both flexural and shear failures for most of the generated model realisations. The scaling of the code-based traffic load model is deemed to simply approximate real traffic load

scenarios having variable intensity. This simplification fosters the efficiency of the adopted analysis procedure and suits for prioritisation purposes. More accurate traffic load models having different intensities can be developed and implemented in the proposed procedure, both taken from different standards, as discussed in Section 4.1, or on the basis of network-specific traffic scenario simulations, about these latter some references are reported in Section 9.2 about the possible future developments of the work. Note that this latter refined strategy for traffic load modelling is hardly feasible in the field of prioritisation analysis. Indeed, the derivation of accurate traffic load models requires the availability of weight-in-motion (WIM) systems and traffic data collected over wide period intervals, eventually supported by surveillance cameras (Zhou *et al.*, 2024), to detect the spatiotemporal distribution of bridge loads and run probabilistic analysis to derive traffic load models having specific parameters (e.g. number of vehicle axles, axle load and axle spacings) (Fiorillo and Ghosn, 2018).

For each model realisation a demand dataset of M values of $M_{D,mid}(\alpha)$ and $V_{D,sup}(\alpha)$ is computed. To calculate fragility curves, the abovementioned demand dataset is converted into demand-to-capacity ratio (DCR) ones, by dividing the demand values $M_{D,mid}(\alpha)$ and $V_{D,sup}(\alpha)$ for the corresponding sectional capacity $M_{C,mid}$ and $V_{C,sup}$ according to Equations (25) and (26) Finally, for the analysed bridge, two $M \times N$ datasets of $DCR_f(\alpha)$, $DCR_s(\alpha)$ are obtained.

$$DCR_f(\alpha) = \frac{M_{D,mid}(\alpha)}{M_{C,mid}} \quad (25)$$

$$DCR_s(\alpha) = \frac{V_{D,sup}(\alpha)}{V_{C,sup}} \quad (26)$$

Fragility curves for the investigated bridge superstructure express the probability of reaching or exceeding a value of the demand equal to the capacity for a given traffic load multiplier. The failure for a given $\bar{\alpha}$ and a given model realisation is achieved when the condition in Equation (27) is satisfied.

$$DCR_t(\bar{\alpha}) = \max(DCR_f(\bar{\alpha}), DCR_s(\bar{\alpha})) \geq 1 \quad (27)$$

The probability of failure $P[failure|\alpha = \bar{\alpha}]$ conditioned to the load multiplier $\bar{\alpha}$ is calculated as the ratio between the number of realisations associated with failure, N_{fail} (number of times the condition $DCR_t(\bar{\alpha}) \geq 1$ holds in a randomly generated sample of realisations) and the total sample size N (as reported in Equation (28)).

$$P[failure|\alpha = \bar{\alpha}] = P[DCR_t(\alpha) \geq 1|\alpha = \bar{\alpha}] = N_{fail}/N \quad (28)$$

Finally, the final fragility function is derived by fitting a cumulative probability distribution (CDF) to the dataset of M values of $P[failure|\alpha = \bar{\alpha}]$, i.e., the dataset of fragility points. Particularly, two probability distribution functions are fitted to such dataset, namely the lognormal cumulative distribution and the generalised extreme value (GEV) distribution. According to the obtained different cases, the type of probability function that best performs the fitting of the observed data is used. To find the best estimate of the parameters of the CDFs, the method of moments (Baker, 2015), i.e., finding the CDF's parameters such that the resulting distribution has the same moments as the distribution obtained from the observed data, or the least square method are used as parameter estimation methods. Clearly, fragility curves can be also computed by referring only to shear or flexural failures if $P[DCR_f(\alpha) \geq 1|\alpha = \bar{\alpha}]$ and $P[DCR_s(\alpha) \geq 1|\alpha = \bar{\alpha}]$ are directly computed without computing $DCR_t(\bar{\alpha})$. In this case, the fragility curves may be used to understand the critical mechanisms between failure and shear for addressing appropriate inspections or interventions.

To investigate the influence of tendon corrosion on the fragility of a single bridge typology, fragility functions are calculated for several intensity of corrosion scenarios, by repeating the abovementioned process for different ξ values. Particularly, for fragility-informed prioritisation, the analyst should repeat the calculations by starting with a value of $\xi = 0$ (un corroded configuration) until a ξ value for which most of the bridge realisations are affected by a failure under gravity loads.

5 MODELLING FLEXURAL CAPACITY CONSIDERING CORROSION EFFECTS

Recently, experimental studies about PC beam performance under natural or artificial corrosion of tendons have been developed. Some of them are listed in Section 2 (Rinaldi, Imperatore and Valente, 2010; Jeon *et al.*, 2019; Belletti *et al.*, 2020) and the most interesting results achieved are also therein discussed. The same holds for experimental tests on corroded prestressing strands or wires, whose behaviour under chloride-induced degradation has been investigated (Franceschini *et al.*, 2022, 2023; Yu *et al.*, 2022). To sum up the abovementioned discussion on corrosion, thoroughly addressed in Section 2, laboratory experimental test results on several strands extracted by naturally corroded PC beams are reported by Franceschini *et al.* (Franceschini *et al.*, 2022), who propose a simplified corrosion-affected constitutive model. In particular, the authors proposed a modified stress-strain relationship for corroded strands, according to experimental evidence from real strands extracted from full-scale beams exposed for 10 years to chloride action from seawater. Regarding artificially induced degradation, further laboratory experimental test results are available in Rinaldi *et al.* (Rinaldi, Imperatore and Valente, 2010), who studied PC beam and steel strand behaviour subjected to man-made accelerated corrosion. Experimental test results on several artificially corroded PC beams are reported in the work, which records a sizable reductive effect on the flexural capacity of corrosion-affected members. Other experimental results on this topic are shown in Yu *et al.* (Yu *et al.*, 2022), alongside new constitutive laws for corrosion-affected mild and prestressing steel, which are calibrated on tension tests of samples of corroded prestressing steel strands and wires. Particularly, these last constitutive models can be very useful for the methodology described in Section 4.

Herein, two different flexural bearing capacity modelling strategies of different accuracy and analytical complexity are tested to be included in the proposed fragility analysis approach. The investigation is performed via the application of the simplified modelling strategy, due to the low computational effort required. The first flexural

capacity modelling strategy considers corrosion as a simple prestressing steel tendon area reduction, while the second one introduces additional corrosion-induced effects on mild and prestressing steel constitutive laws. The application of both strategies is discussed in the following, by comparing the analytical results with experimental results available in literature (Rinaldi, Imperatore and Valente, 2010; Yu *et al.*, 2022).

5.1 Method I: Tendon area reduction

The first modelling strategy (I procedure hereafter) considers corrosion influence in the flexural bearing capacity calculation as a simple prestressing tendon area percentage reduction ξ_p and no stress-strain relationship modifications are adopted. The investigation of a strategy accounting for such a simplification assumption aims at establishing whether the problem of modelling corrosion influence in flexural bearing capacity of PC members can be solved with low expensive analyses in terms of time and computational effort or if more refined methodologies are needed.

The beam cross-section scheme adopted for computing the ultimate bending moment is represented in Figure 34. The sum of the areas of each single rebar and strand or tendon is considered as lumped in the corresponding centroids, for mild and prestressing steel, respectively, either at the top or at the bottom of the investigated cross-section. The computation of the ultimate bending moment, M_u , is based on the following assumptions:

- 1) Plane cross-sections and perfect steel-concrete bond after flexural deformation;
- 2) Stress-block model for concrete constitutive law in compression;
- 3) Elastic-perfectly plastic behaviour for mild and prestressing steel.

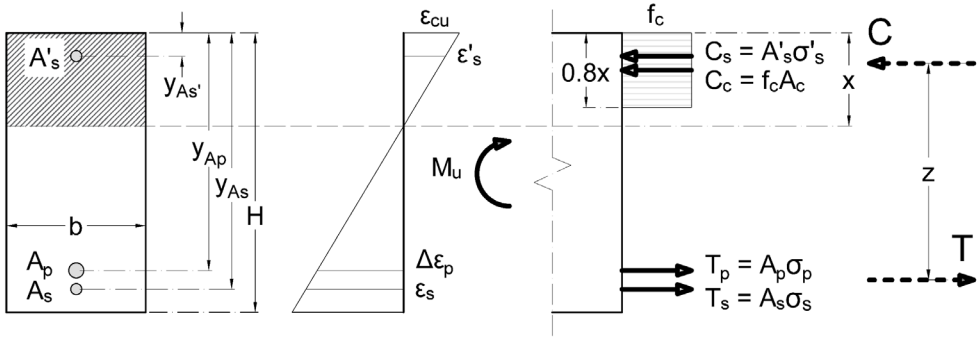


Figure 34 - Beam cross-section model for ultimate bending moment computation. C_c and C_s are the compression resultant force for concrete and upper steel reinforcements; T_p and T_s are the tensile resultant force for prestressing and bottom steel reinforcements; ϵ'_s and ϵ_s are the strains of the mild top and bottom steel; ϵ_{cu} is the ultimate compressive strain of concrete; $\Delta\epsilon_p$ is the tensile strain increment of the prestressing steel tendons. Other symbols adopted in the figure are explained in the main text.

Flexure capacity calculation requires the computation of prestressing tendon area in balanced rupture hypothesis, defined as the failure given by the simultaneous attainment of ultimate compression strain ϵ_{cu} for upper concrete fibre and yielding tensile strain for mild and prestressing steel ϵ_{sy} . This is necessary for distinguishing the cases between fragile and ductile flexural failures for the analysed cross-section, leading to different ways of ultimate bending moment calculation.

It is worth specifying that, for appropriate design of prestressed girders, a ductile failure can always be considered, as the prestressing tendon area is always less than the balanced one. Furthermore, the reduction of steel area due to corrosion facilitates ductile failures. Therefore, generally, the computation of the ultimate bending moment M_u is performed through Equation (29), where A_p and A_s are the prestressing steel and mild steel areas, $f_{p,01}$ and f_y are the prestressing and mild steel conventional yielding strengths, respectively, and z is the internal lever arm, i.e., the distance between the compression and tension resultant forces, depending on the neutral axis position (leading to different area values of the concrete compression zone and consequently different heights of compression resultant force).

$$M_u = (A_p f_{p,01} + A_s f_y) z \tag{29}$$

In (rare) case of non-ductile failure, the ultimate bending moment M_u can be computed through Equation (30), herein reported for the sake of completeness, where f_c is the ultimate compression strength of concrete, A_c indicates the area of the concrete compression zone; σ'_s , σ_s and σ_p are the stresses of the upper and bottom mild steel and prestressing steel reinforcements, respectively; A'_s , A_s and A_p are the areas of upper and bottom mild steel and prestressing steel reinforcements, respectively; and $y_{A'_s}$, y_{A_s} and y_{A_p} are the upper and bottom mild steel and prestressing steel reinforcement height (i.e. distance from the upper edge), respectively, as represented in Figure 34.

$$M_u = 0.6 x f_c A_c + (\sigma'_s A'_s) |x - y_{A'_s}| + (\sigma_s A_s) (y_{A_s} - x) + (\sigma_p A_p) (y_{A_p} - x) \tag{30}$$

5.2 Method II: Effect of modifications of steel constitutive laws

The second strategy (II procedure hereafter) is based on the same basic assumptions of the first strategy (i.e., points 1), 2), and 3), in Section 5.1). Steel areas are modelled as lumped in their centroids as in the first strategy. However, both mild and prestressing steel area reduction and modification of stress-strain relationships (Yu *et al.*, 2022) are considered with increasing corrosion levels.

The stress-strain model adopted for simulating the prestressing steel response is modified based on the influence of corrosion degree ξ_p (defined according to Equation (23)) and it is described in Equation (31) and Figure 35. In particular, a critical value of corrosion $\xi_{p,cr}$ is defined as that specific corrosion value corresponding to the transition from an elastic-plastic law to a simply elastic stress-strain relationship. The constitutive relationship for corroded prestressing steel is expressed as follows.

$$\sigma_{pc} = \begin{cases} \varepsilon_{pc} E_{pc} & \text{for } \varepsilon_{pc} \leq \varepsilon_{pyc} \\ 0.85 f_{puc} + (\varepsilon_{pc} - \varepsilon_{pyc}) \left(\frac{0.15 f_{puc}}{\varepsilon_{puc} - \varepsilon_{pyc}} \right) & \text{for } \varepsilon_{pc} > \varepsilon_{pyc} \end{cases} \begin{cases} \text{for } \xi_p < \xi_{p,cr} \\ \text{for } \xi_p \geq \xi_{p,cr} \end{cases} \tag{31}$$

In the above equations, E_{pc} , f_{puc} , ε_{puc} are the elastic modulus, ultimate strength and ultimate strain of corroded prestressing tendons, respectively; whereas ε_{pyc} is the prestressing steel yielding strain (Equation (32)) computed as the ratio between f_{pyc} and E_{pc} . The prestressing steel yielding stress, f_{pyc} , i.e., the stress corresponding to strain equal to 1%, for steel strand is evaluated according to Equation (33), following the Probabilistic Model Code (Joint Committee on Structural Safety, 2001).

$$\varepsilon_{pyc} = \frac{f_{pyc}}{E_{pc}} \quad (32)$$

$$f_{pyc} = 0.85f_{puc} \quad (33)$$

E_{pc} , f_{puc} and ε_{puc} are defined according to Equations (34), (35) and (36).

$$E_{pc} = \beta_{Ec}E_p \quad (34)$$

$$f_{puc} = \frac{\alpha_{puc}}{1 - \eta_p} f_{pu} \quad (35)$$

$$\varepsilon_{puc} = \beta_{puc}\varepsilon_{pu} \quad (36)$$

These are respectively dependent on E_p , f_{pu} and ε_{pu} , i.e., the prestressing steel elastic modulus, ultimate tensile strength and ultimate tensile strain in the uncorroded configuration, and on three coefficients expressing the influence of corrosion. In particular, in Equation (34), β_{Ec} is the relative elastic modulus, defined as the ratio between E_{pc} and E_p , which can be estimated via Equation (37); in Equation (35), α_{puc} is the ratio between the ultimate load of corroded prestressing steel and the ultimate load of non-corroded prestressing steel and is estimated via Equation (38); finally, in Equation (36), the coefficient β_{puc} is the ratio between the ultimate strain of corroded prestressing steel and the ultimate strain of uncorroded prestressing steel, and is estimated via Equation (39). Equation (36) holds for values of corrosion degree lower than a critical threshold, discussed more in detail later on, beyond which the loss of the stress-strain law plastic branch is recorded in experimental tests (Yu *et al.*, 2022).

$$\beta_{Ec} = \begin{cases} 1 & \text{for steel wires} \\ 1 - 0.848 \xi_p & \text{for steel strands} \end{cases} \quad (37)$$

$$\alpha_{puc} = \begin{cases} 1 - 1.935 \xi_p & \text{for steel wires} \\ 1 - 2.683 \xi_p & \text{for steel strands} \end{cases} \quad (38)$$

$$\beta_{puc} = 1 - 9.387 \xi_p \quad (39)$$

The use of Equations (36) and (39) can lead to numerical issues due to the experimental nature of the relationships. Indeed, Equation (39) leads to a significant reduction of the modified ultimate strain ratio β_{puc} with increasing corrosion level ξ_p . Therefore, the corroded ultimate strain ε_{puc} can assume values lower than the modified yielding strain ε_{pyc} . This issue should be checked with increasing corrosion level scenarios to avoid numerical problems when computing the flexural bearing capacity of a generic cross-section.

More details about the modified stress-strain relationship of prestressing steel can be found in Yu et al. (Yu *et al.*, 2022). In accordance with this study, a very first value of 0.08 can be adopted as critical level of corrosion degree $\xi_{p,cr}$. However, it is worth mentioning that further numerical issues can arise in computing the flexural capacity if such a fixed value of critical corrosion degree is adopted. More in detail, the balanced corrosion degree and the consequent ultimate bending moment computation are obtained by solving the translational equilibrium equation (TEE), via an iterative numerical method (i.e. the bisectional method) for the analysed section. The definition of a reduced ultimate strain ε_{puc} through two different formulations (for lower and higher corrosion values with respect to a fixed critical corrosion value $\xi_{p,cr}$) introduces a mathematical discontinuity in the modified stress-strain relationship for corroded steel (Equation (31)). As observed through the analysis of multiple bridge realisations in the case study section, such discontinuity can prevent the iterative process of finding convergence and the solution for the TEE. Note that, although the $\xi_{p,cr}$ is fixed in (Yu *et al.*, 2022), Franceschini et al. (Franceschini *et al.*, 2022), albeit referring to corrosion triggered by a specific external agent among all the possible ones, i.e., chloride-induced

corrosion, in their experimental study found variability of this critical threshold $\xi_{p,cr}$, suggesting the adoption of a range of values to implement this threshold in the corrosion model. Therefore, considering the outcomes in (Franceschini *et al.*, 2022), a modification of the model proposed in (Yu *et al.*, 2022) is adopted in this study, which leads to slightly different values of critical corrosion degree $\xi_{p,cr}$ realisation-by-realisation. The modification aims to avoid the discontinuity in the stress-strain relationships for corroded prestressing steel and prevent convergence issues. To check the physical consistency of the obtained $\xi_{p,cr}$ values, such a variation has been analysed throughout the randomly generated sample for the selected case-study (see Section 6), and an average value of critical corrosion degree approximately equal to 0.08 has been found, alongside with values that appropriately match the interval reported in Franceschini *et al.* (Franceschini *et al.*, 2022). Therefore, although based on a numerical criterion without any physical basis, such modification is deemed reasonable and is herein adopted as necessary for solving the flexural capacity problem. However, it is worth mentioning that this represents a limitation of the adopted model for corroded prestressing steel, which can be overcome by adopting more accurate corroded steel models.

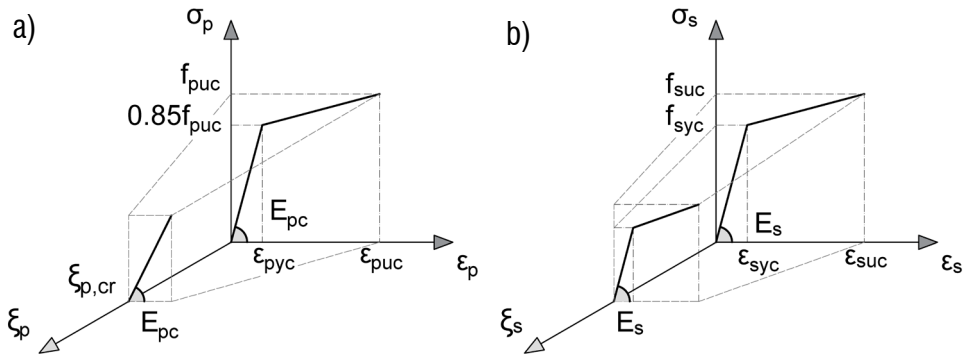


Figure 35 - Modified stress-strain relationship for corrosion-affected a) prestressing steel strands and b) mild reinforcing steel.

In the second strategy, also a corrosion-affected stress-strain relationship for mild reinforcement can be considered, inspired by the model proposed by Yu *et al.* (Yu

et al., 2022). In the proposed methodology, an elastic-plastic law is adopted, described in Equation (40) and Figure 35.

$$\sigma_{sc} = \begin{cases} E_s \varepsilon_{sc} & \text{for } \varepsilon_{sc} \leq \frac{f_{syc}}{E_s} \\ f_{syc} + \frac{\varepsilon_{sc} - \varepsilon_{syc}}{\varepsilon_{suc} - \varepsilon_{syc}} (f_{suc} - f_{syc}) & \text{for } \varepsilon_{sc} > \frac{f_{syc}}{E_s} \end{cases} \quad (40)$$

In this equation, E_s is the elastic modulus of non-corroded mild reinforcement, f_{syc} , f_{suc} , ε_{syc} and ε_{suc} are the yielding and ultimate strength and strain of corroded steel rebars, respectively, computed via Equations from (41) to (44).

As for the prestressing steel model, this law depends on three parameters, i.e., f_{syc} , f_{suc} and ε_{syc} , that, in turn, vary according to a different value of corrosion degree ξ_s .

$$\varepsilon_{syc} = \frac{f_{syc}}{E_s} \quad (41)$$

$$f_{syc} = \frac{1 - 1.092\xi_s}{1 - \xi_s} f_{sy} \quad (42)$$

$$f_{suc} = \frac{1 - 1.152\xi_s}{1 - \xi_s} f_{su} \quad (43)$$

$$\varepsilon_{suc} = e^{-2.556\xi_s} \varepsilon_{su} \quad (44)$$

In the equations above, f_{sy} , f_{su} and ε_{su} are the yielding and ultimate strength and ultimate strain of uncorroded reinforcing steel rebars.

The methodology adopted in the second strategy (II procedure) is described in Figure 36. The procedure starts from the investigation of the balanced corrosion rate ξ_{pb} (Step 1 in Figure 36), i.e., the specific level of corrosion rate such that a balanced failure scenario holds for the generic cross-section. In this second procedure, the balanced failure scenario is defined at the simultaneous attainment of the ultimate strain ε_{cu} in the upper fibre of concrete in compression and the ultimate strain in prestressing

steel tendons (ε_{pu} or ε_{puc}) in tension at the bottom of the section. In this way, it is possible to distinguish between failure due to concrete crushing in compression (CC) or tendon rupture in tension (RT). The translational equilibrium equation (TEE) in the balanced failure scenario is solved through an iterative solution method, as well as in the CC (Step 2a in Figure 36) and RT (Step 2b in Figure 36) scenarios.

Once a solution for the TEE is obtained, the ultimate bending moment M_u can be computed in both cases (CC and RT) through Equation (39) (Step 3 in Figure 36). It is worth noting that in the case of T-section beams, in which also the slab contribution is considered in flexural capacity computation, the variation of the internal lever arm z depends on the neutral axis position x , leading to different values of strain ε'_s in the upper mild steel reinforcement. This means that upper reinforcement could even assume negative strain values, switching from tension to compression stress state for each iteration. This might lead to numerical issues in chasing the problem solution. An easier numerical procedure can be adopted breaking down Equation (39) in Equation (45), for which all the terms are specified in Figure 34.

$$M_u = C_c(0.6x) + C_s|x - y_{A'_s}| + T_s(y_{A_s} - x) + T_p(y_{A_p} - x) \quad (45)$$

Further details about the adopted procedure for computing flexural bearing capacity are reported in Figure 36.

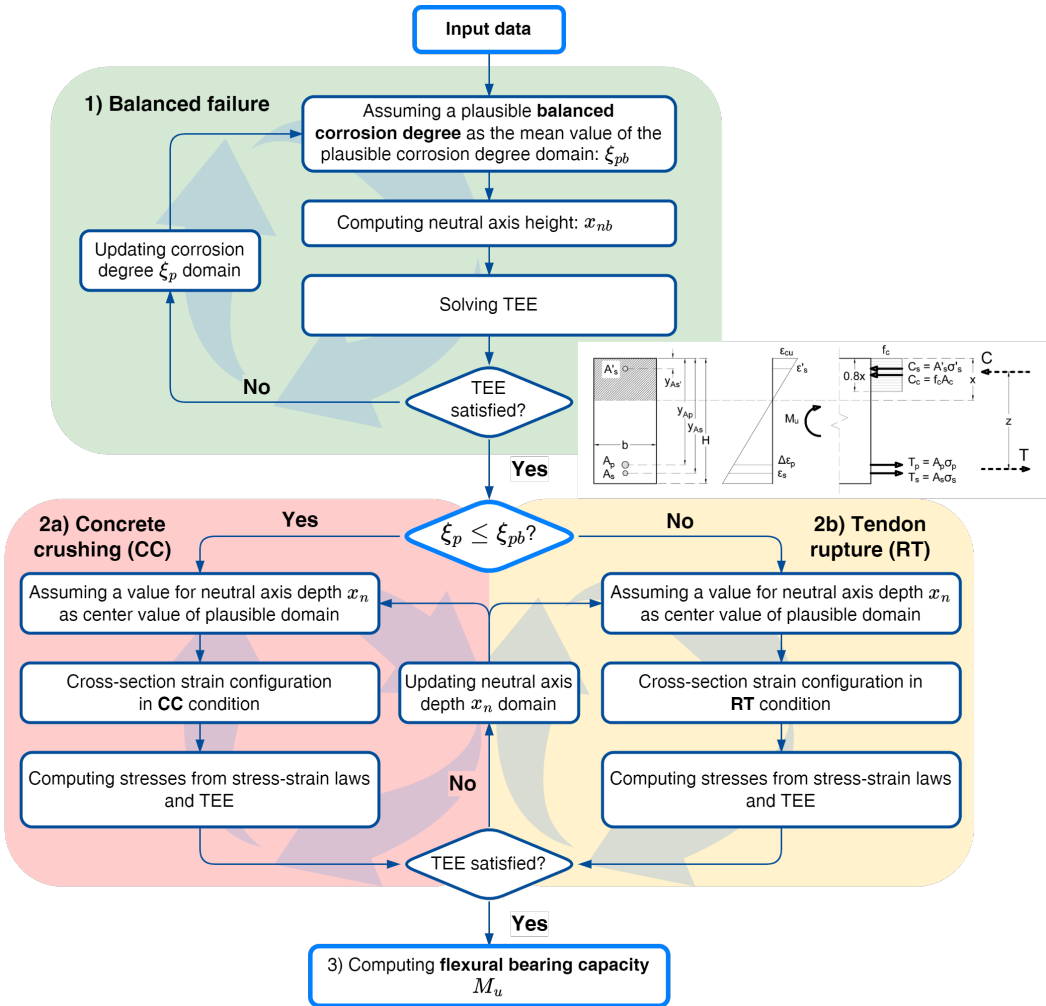


Figure 36 - Flowchart for computing corrosion-affected ultimate bending moment M_u .

5.3 Validation and comparison of methods

Experimental test results on different specimens performed by Yu et al. (Yu et al., 2022) and Rinaldi et al. (Rinaldi, Imperatore and Valente, 2010) are adopted as references for validating and comparing the accuracy of the two different analytical approaches, indicated as procedure I and procedure II. Note that corrosion effects are modelled by a simple prestressing steel tendon area reduction with no stress-strain relationship modification in procedure I (Section 5.1), whereas procedure II accounts

for both prestressing steel tendon area reduction together with the stress-strain relationship modification (Section 5.1 and 5.2). Both the abovementioned studies report results in terms of ultimate load, P_{ur} , obtained through flexural tests on different PC beam specimens presenting corroded strands in a four-point bending set-up. The corrosion level ξ_p is expressed as the steel mass loss ratio and P_u is the ultimate load computed with analytical procedures exposed above. Results are shown in Table 3, where values obtained from the simple procedure I and the second refined procedure II (indicated as I Pr. and II Pr. In Table 3) are reported.

Table 3 - Procedure validation: results of experimental tests vs the analytical methodologies.

Reference	Specimen (ID)	Corrosion level ξ_p	Tested P_{ur} (kN)	P_u (kN)		P_u/P_{ur}		Failure mode
				I Pr.	II Pr.	I Pr.	II Pr.	
(Yu <i>et al.</i> , 2022)	L1	0.00	227.8	240.3	237.8	1.05	1.04	CC
	L2	0.09	216.7	227.8	213.4	1.05	0.98	RT
	L3	0.14	195.1	205.8	188.0	1.05	0.96	RT
(Rinaldi, Imperatore and Valente, 2010)	B7	0.00	160	217.1	214.3	1.36	1.34	CC
	B8	0.20	95	186.8	81.2	1.97	0.85	RT
	B9	0.20	115	186.8	81.2	1.62	0.71	RT
	B2	0.00	190	226.0	226.9	1.19	1.19	CC
	B3	0.14	85	203.0	149.1	2.39	1.75	RT
	B1	0.20	66	192.9	81.9	2.92	1.24	RT
	B4	0.00	210	230.9	234.8	1.10	1.12	CC
	B6	0.07	200	219.1	199.9	1.10	1.00	RT
	B5	0.20	70	196.6	82.4	2.81	1.18	RT

Through the ratio between the analytically computed and the experimentally tested ultimate loads (P_u/P_{ur}), it is evident that the simplified I procedure tends to produce higher errors with increasing corrosion levels. This is related to the simplification in dealing with corrosion modelling, as this procedure neglects some fundamental corrosion-related effects, e.g., the stress-strain relationship modification. Indeed, considering corrosion as a mere uniform steel area reduction implies disregarding all the microscopic alterations suffered by the deteriorated material.

The same outcome cannot be stated for the second procedure which leads to a non-negligible higher accuracy in analytical computation, even though in most of the cases the results are not safe-sided. Results in Table 3, graphically presented in Figure 37, show that the ratio P_u/P_{ur} clearly decreases if computed through the II procedure instead of the I procedure. Some calculations overestimate the tested ultimate loads and this can be related to the variability of the test results, as demonstrated by the two different values of the recorded ultimate load P_{ur} obtained by testing the same specimen B8 and B9 (see Table 3) by Rinaldi et al. (Rinaldi, Imperatore and Valente, 2010) to check the test repeatability. This hypothesis is further confirmed by the analytical calculations performed with the same procedure by Yu et al. (Yu *et al.*, 2022), which overestimate the ultimate load of the same two specimens, i.e., B3 and B7 (see Table 3).

Summarising, although from a practical point of view, the first model is more direct and simpler, it represents a rough simplification and leads to significant inaccuracies. Therefore, although more complex, the second method is recommended for the evaluation of the flexural capacity of PC cross-sections subjected to tendon corrosion. A limitation of both approaches stems from not considering the interaction between corrosion and fatigue (Guo *et al.*, 2024). However, if of interest, the capacity deterioration due to fatigue can easily be included using the residual cross-section area approach (Su *et al.*, 2022), which models the effect of microcracks related to fatigue as an equivalent steel area reduction which is added to the corrosion-related one. Moreover, another limitation comes from not considering the effect of corrosion on the bonding between steel and concrete. It is worth recalling that this verification is performed by considering only uniform corrosion. The case of pitting corrosion, which is the most common in post-tensioned tendons, is not considered in this work.

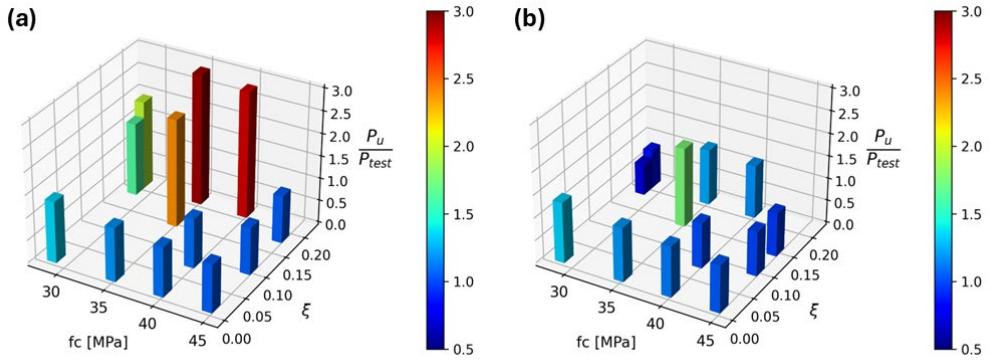


Figure 37 - Ratios of the analytically computed P_u to the experimentally tested ultimate load P_{ur} : (a) I procedure vs (b) II procedure.

6 CASE-STUDY: A SET OF ARCHETYPES OF SIMPLY SUPPORTED GIRDER-TYPE PC BRIDGES

6.1 *Description of the typological and general features of the case-study*

The proposed methodology is applied to investigate the structural fragility of a class of simply supported girder-type PC superstructures. Particularly, a case-study bridge portfolio is selected within an existing highway network in Southern Italy built in the 1960-1970 and designed according to the old Italian regulation, named “*Circolare n.384 del 14.02.1962, Norme relative ai carichi per il calcolo dei ponti stradali*” (Ministero delle Infrastrutture e dei Trasporti, 1962). Such old code, in force in Italy until the 1980s, prescribed traffic load models simulating “real” civil and military traffic vehicles. Particularly, it recommended the use of six real traffic load patterns (not reported for brevity), representing civil and military vehicles, appropriately combined in side-by-side lanes to maximise flexure and shear stresses on bridge girders. This traffic load modelling approach is strongly different with respect to current codes which prescribe the use of “conventional” design loads which do not represent real vehicles, but aim to induce the stress demand related to the maximum real traffic load scenario for a given reference period (100 years in the Eurocode). To the author’s knowledge, no studies are currently available comparing the effects on the flexural and shear capacity of bridge components designed considering such old load prescriptions with respect to the current one.

The analysed portfolio includes simply supported bridges characterised by superstructures composed of PC beams with post-tensioned tendons. The proposed methodology is applied with the scope to prioritise special inspections and a possible subsequent detailed assessment.

Since a complete collection of design documents accurately describing geometric characteristics and structural details of the bridges included within the portfolio is not available, a typological study based on parametrically generated archetype superstructures is carried out. Particularly, six superstructure typologies are identified by observing structural bridge characteristics. These are represented by six archetype

superstructures generated by considering: 1) two different values of beam number of the deck, i.e. three and four, and 2) three different values of span length (L_b), i.e., 30 - 40 - 50 m. These typologies belong to the medium-span length bridge class according to the most recent Italian Guidelines (Consiglio Superiore dei Lavori Pubblici (CS.LL.PP.), 2020). The parametric geometric characterisation of the case-study archetype superstructures is illustrated in Figure 38.

For the analysed bridge typologies, uncertainties in geometry and constructive features are considered as explained in the following subsection. The deck total width is defined by the spacing between the girders, which in turn depends on the beam height and the span length. Depending on the deck width, the carriageway and the number of traffic lanes are defined. The girder height varies according to the span length. The girders of the superstructure present a variable number of tendons collected in specific ducts filled with cementitious grout. The value of the prestressing steel area is related to the span length and is computed through the prestressing steel ratio ρ_{sp} , i.e., the ratio between the prestressing steel area and the tension area of the concrete cross-section, as stated in Section 6.2. It is worth mentioning that, for the analytical simplified modelling strategy, the diaphragms are assumed to guarantee the transverse load distribution among the girders of the same superstructure. A number of five diaphragms, i.e., two at supports, one at mid-span and other two at $\frac{1}{4}$ and $\frac{3}{4}$ of the span length, ensures the transversal repartition of loads among the girders in the selected case-study archetypes. As a result of their cross-sectional shape, length and number in a single span, these components ensure the validity of the assumption of infinite bending stiffness of diaphragms compared to the torsional stiffness of the individual girders, following the Courbon-Albenga assumptions. The same cannot be stated for the refined numerical FE modelling strategy, where transversal elements like diaphragms and the slab are modelled with linear and non-linear beam elements.

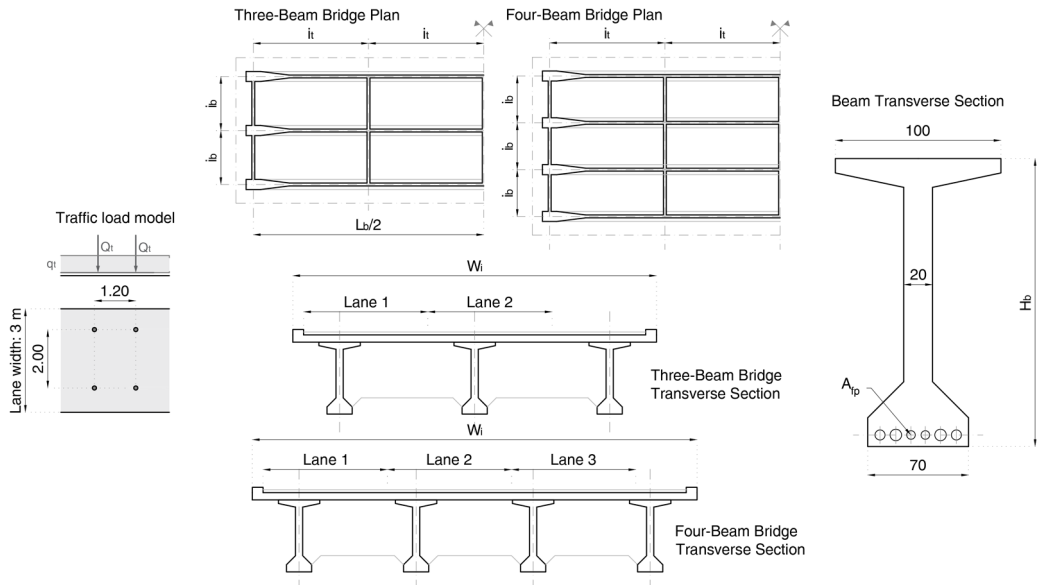


Figure 38 - Geometric and structural characteristics of the case-study superstructures and traffic load model.

6.2 Selection of uncertain parameters and corrosion scenarios

Statistical distributions and regression laws are used to model the variability of structural and material parameters within each analysed typology. Some of these are retrieved from the study by Miluccio *et al.* (Miluccio *et al.*, 2021), referring to bridges in South Italy. For prestressing steel, statistical distributions are derived from Jacinto *et al.* (Jacinto *et al.*, 2012), who analysed a sample of strands produced by six manufacturers from four countries, i.e., Portugal, Spain, Italy and Thailand. Such distributions and models are listed in Table 4 and Table 5. For parameters whose statistical distributions are not available in the literature, the maximum uncertainty is assumed using a continuous uniform distribution (Celik and Ellingwood, 2010). Particularly, for geometric parameters like slab and road pavement thickness, the available design documents of bridges belonging to the analysed bridge class are adopted as a reference for boundary values. Particularly, a key parameter for the computation of the ultimate bending moment capacity is the effective depth of the prestressing tendon system. A fixed distance from the section bottom fibre equal to 8 cm is adopted for defining the position

of the prestressing steel, following the available design documents. Then, the effective tendon depth varies according to the different values of the beam height, defined by the corresponding regression model reported in Table 5. As far as initial prestressing stress value is concerned, the “Brevetto Morandi” is taken as a reference, as the prestressing tendon systems typically adopted for designing structures belonging to the case-study bridge class followed the indications recommended by such a document. The patent recommends an initial prestressing value not higher than 1200 MPa. Boundary values for the initial prestressing uniform distribution in Table 4 are obtained considering overall prestressing losses in a range between 30% and 40%.

To investigate the influence of the degree of tendon corrosion on structural fragility, different critical corrosion scenarios are considered. Each corrosion scenario is associated with a corrosion degree ξ_p quantified as the (percentage) ratio between the tendon mass considered as affected by corrosion and the initial tendon mass (see Equation (23) in Section 4.4). In the proposed analytical methodology, no variation in the distribution of corrosion among the different tendons for a given girder cross-section is considered. This is because the spatial distribution of tendons within the analysed cross-section is neglected in the adopted algorithm. Additionally, the spatial variation in corrosion distribution along the girder longitudinal axis is neglected since only significant cross-sections are considered, as explained in Section 4.3.1. Accordingly, the same choices are adopted for the refined numerical strategy, as the final results will be compared under the same corrosion scenarios.

For each corrosion scenario, the tendon mass loss is associated with the girder cross-sections considered to calculate the DCR (i.e., mid-span for flexure and at the supports for shear). In the analysed scenarios, the corrosion degree is equal to 0, 5, 10, 15, 20 and 25% of the initial tendon mass. For mild reinforcing steel, a zero-corrosion level is assumed for each scenario at the bottom of the beam section. Note that the corrosion of mild steel can be uncorrelated to the corrosion of tendons within the ducts. Preliminary sensitivity analyses (which are not shown for brevity) show the negligible influence on fragility related to the corrosion level of mild steel with respect to the one related to prestressing components. For mild steel reinforcement on the top of

the beam, no corrosion is assumed to be the best choice, as top reinforcements are, in general, well protected by the presence of the concrete slab, as far as the deck is properly waterproofed with an appropriate waterproofing layer.

Table 4 - Statistical distributions for independent variables.

Parameter	Distribution	Parameters/Bounds	
Mean concrete compressive strength (f_{cm}) (Miluccio <i>et al.</i> , 2021)	Lognormal	$\mu = 38.5$; COV = 11.4%	MPa
Mean steel tensile strength (f_{ym}) (Miluccio <i>et al.</i> , 2021)	Lognormal	$\mu = 451$; COV = 7.2%	MPa
Conventional yield strength of prestressing steel ($f_{p,0.1}$) (Miluccio <i>et al.</i> , 2021)	Lognormal	$\mu = 1665$; COV = 7.5%	MPa
Ultimate strain of prestressing steel (ε_{pu}) (Jacinto <i>et al.</i> , 2012)	Normal	$\mu = 5$; COV = 8.0%	%
Prestressing steel Modulus of Elasticity (E_p) (Jacinto <i>et al.</i> , 2012)	Normal	$\mu = 195$; COV = 2.5%	GPa
Slab thickness (s)	Uniform	[0.20; 0.30]	m
Road pavement thickness (h_{bit})	Uniform	[0.08; 0.20]	m
Residual stress level of prestressing steel (σ_{sp})	Uniform	[720; 840]	MPa

Table 5 - Statistical distributions and regression models for dependent variables. L_b is the span length of the beam, d_{sp} is the effective depth of the prestressing tendon system measured from the top fibre of the beam section.

Parameter	Predictors	Distribution/Regression model	Bounds	
Beam height (H_b)	L_b	Uniform	$[L_b/20; L_b/15]$	m
Beam spacing (i_b) (Miluccio <i>et al.</i> , 2021)	L_b, H_b	$H_b = 0.28i_b + 0.03L_b$	-	m
Prestressing steel ratio (ρ_{sp}) (Miluccio <i>et al.</i> , 2021)	L_b	$\rho_{sp}d_{sp} = 8.16 \cdot 10^{-5}L_b + 1.85 \cdot 10^{-5}L_b^2$	-	-

6.3 Sensitivity analysis to define the size of the representative sample

The number of bridge realisations generated by the statistical sampling is expected to affect the fragility results. Therefore, an optimal sample size should be chosen, to achieve a compromise between computational effort and stability in statistics (i.e. convergence in results compared to an exact solution). Particularly, in this section, an optimum sample size is identified through a sensitivity analysis in which fragility results related to different sample sizes are compared to the best estimate (assumed as benchmark sample size). The optimal sample size is the minimum sample size leading to negligible (considering a given tolerance) differences in fragility results, with respect to the best estimate. For this purpose, the abovementioned sensitivity analysis is carried out by considering, as an example, the four-beam typology with a variable corrosion degree of steel tendons equal to 0% and 15%.

First, a set of 10^4 bridge realisations is generated for each analysed span length value and subjected to the fragility analysis. Considering the very large sample size, the computed fragility curve is assumed as the best estimate. Subsequently, several samples with increasing sizes, from 5 to 600, are produced and their fragility curves are compared with the result obtained with the best estimate. The comparison is performed in terms of relative error (RE) between the medians of the fragility curves, i.e., the relative difference between the fragility curve median of each sample size and the best estimate.

This process is repeated several times for different randomly generated samples and for the two different corrosion scenarios. The results are shown in Figure 39 for ten repetitions of sample generation, for the two different values of corrosion degree ξ_p , equal to 0% and 15%. A relative error threshold of 2.5% is set to identify the optimal choice. By observing the results, the optimal sample size ranges between 50 and 300 model realisations. Therefore, a number equal to 300 model realisations turns out to be the optimal choice for ensuring convergence in statistics in all the analysed cases. Subsequently, an additional check is performed, by comparing the dispersion values of the different random generations of the optimal sample size, with the dispersion values of the best estimate, considering the abovementioned bridge typologies. Considering

that the maximum observed relative error on dispersion is equal to 11%, the optimal sample size identified in the previous analysis is considered appropriate. For the sake of brevity, the results of this last check are presented in Table 6 for the four-beam, 30m-span bridge typology, only. In conclusion, a sample size of 300 bridge model realisations is used to perform the following analyses.

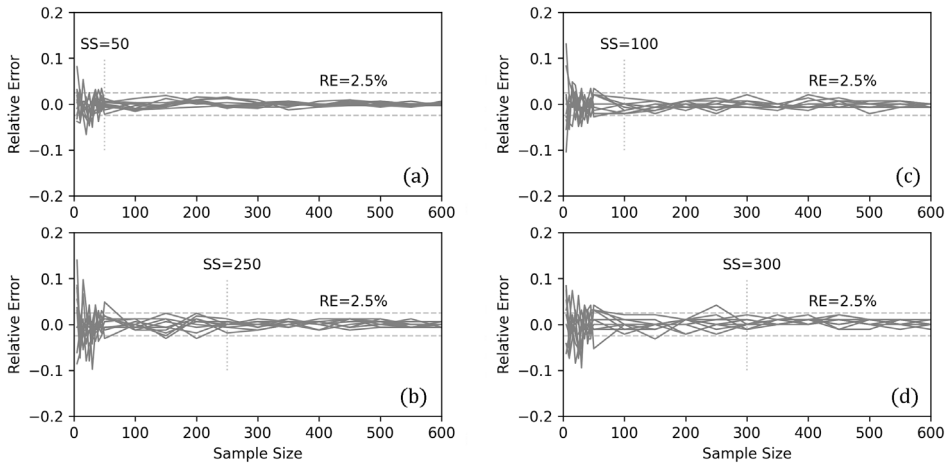


Figure 39 - Relative errors (RE) as a function of sample size for span length equal to 30 m with (a) 0% and (b) 15 % corrosion degrees; span length equal to 50 m with (c) 0% and (d) 15 % corrosion degrees. SS indicates the optimal sample size.

Table 6 – Dispersion values of the optimal sample size and the best estimate for the 30m-long span four-beams bridge (RE is the relative error).

ξ_p [%]		Best estimate	Optimal size
0	Dispersion	0.211	[0.192; 0.226]
	RE		[-9.04; 7.02]%
15	Dispersion	0.175	[0.155; 0.185]
	RE		[-11.80; 5.27]%

7 NUMERICAL FE MODELLING OF THE ARCHETYPE-SET

The analytical simplified model is really straightforward, being characterised by a simply supported single beam reflecting the geometric characteristics of the analysed edge girder of the bridge deck, loaded by a uniformly distributed load simulating the code-compliant traffic load model, plus a concentrated load placed in the worst location according to the selected stress to be assessed. On the opposite side, the refined numerical FE model is much more complicated and requires an appropriate discussion to list modelling and analysis choices. Herein, the model was realised via the OpenSeesPy (Zhu, McKenna and Scott, 2018) software, due to its characteristics of automation, which are extremely useful for probabilistic analysis. The software is the Python version of the renowned OpenSees software (McKenna, Fenves and Scott, 2000), developed in 2000 by Frank McKenna, Gregory L. Fenves and Micheal H. Scott. Through OpenSeesPy, the model generation is performed by coding through Python language (Van Rossum and Drake, 2009), taking advantage of Visual Studio Code (Microsoft Corporation, 2019), as IDE (Integrated Development Environment). Moreover, the model was generated in part by exploiting the possibility provided by the Jupyter Notebook (Kluyver *et al.*, 2016) library, which allows code to be conveniently written and executed in several cells, so that the output of each individual cell can be monitored and operations performed in parts. Such a capability was of paramount importance, given the complexity of the code for generating such a model. This latter was generated in such a way as to be of a parametric type for the class of simply supported girder-type PC bridges, and for this reason, its use can easily be extended to different archetypes belonging to this bridge class, by instantaneously and automatically varying quantities such as the span length, the number of girders or the number of diaphragms of each typology. In this section, an in-depth analysis of every aspect involved in the FE model is described.

7.1 *Modelling of prestressing effects*

Before starting the discussion on geometry and materials used for generating an FE model suitable for the simply supported girder-type PC bridge class, it is worth

analysing how to model prestressing effects on the structure in OpenSeesPy. It is of common practice to introduce prestressing effects in a structural model simulating a prestressed component by applying an external equivalent force system. Such a strategy is not suitable for the scope of the present work, as it involves the application of a fixed external force system to the structure and the initial stress and strain of the prestressing tendons are neglected. This leads to an incorrect assessment of the element's response, as in presence of corrosion, it is precisely the tendons that most probably govern the failure of the section when the ultimate strain is reached.

For this reason, an alternative strategy is adopted in this study. OpenSeesPy provides the possibility of applying some modifications to the adopted materials, by defining materials that are wrapped to the existing ones. The so-called wrapper materials are very useful at the aim of representing the prestressing effects, as, among the whole set of possibilities, the *Initial Strain* or *Initial Stress* (Pacific Earthquake Engineering Research Center (PEER), 2008; Zsarnóczy *et al.*, 2022) material can be selected. Thanks to these wrapper materials, an initial strain or stress, respectively, can be applied to other existing materials in the model to generate. Applying one of them to the prestressing steel material, the prestressing process can be simulated.

To test the reliability of such a modelling strategy, a comparison between the results of the application of the *Initial Strain* and *Initial Stress* materials in OpenSeesPy, with the application of an external equivalent force system in the software SAP2000 (Computers and Structures, 2016) has been performed. For this application, a 40m-long span simply supported PC beam with a simple rectangular 80x200 cm section has been analysed, simulating the span of the 40m-long span archetype described in Section 6.1 and a compatible value of a relative beam height. The prestressing is provided to the element through six M5/12-type prestressing tendons (see Figure 41). This tendon type belongs to the so-called "Brevetto Morandi" system, used in Italy in the 1960s for the construction of post-tensioned structures. The tendon system is placed at the bottom of the cross-section, at an 8 cm distance from the bottom fibre, in conformity with the prestressing height adopted in the case-study definition (see Section 6.2). A prestressing stress value of 540 MPa is chosen for the application. A C25/30-

type concrete and B450C-type mild steel reinforcement are used as ordinary materials. A fibre modelling element is used in OpenSeesPy, while a linear elastic model is used in SAP2000, as the beam element is expected to remain in the elastic field.

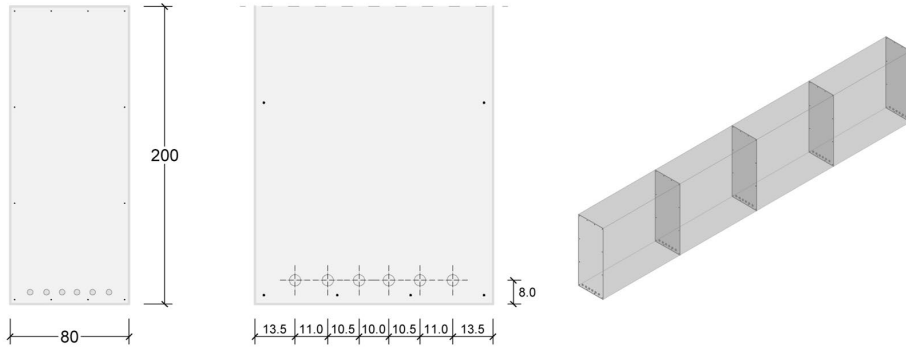


Figure 40 – Simply supported beam adopted for comparing prestressing effects obtained through different prestressing modelling strategies.

Results show perfect correspondence in the application of the two wrapper materials and good correspondence with results by SAP2000. Indeed, an upward vertical displacement is recorded in the three different cases, equal to 4.6 cm for the OpenSeesPy fibre model and 4.3 cm for the SAP2000 linear elastic model. The differences between the two models may be related to the different modelling strategies and the different level of refinement of the materials adopted in OpenSeesPy and SAP2000. Furthermore, it is worth mentioning that using the *InitStrain* command on OpenSeesPy for modelling the application of the prestressing force, when looking at the initial stress state imposed to the tendon fibre, a 10% stress loss compared to the initial imposed prestress emerges. This is most probably related to the redistribution of stresses among the different materials in the element section. The same loss is recorded even when varying the initial imposed prestress value.

2.3 - Portata ed ingombro dei cavi M5

(Vedi al § 2.4 le limitazioni per i tipi S)	Cavo tipo	M5/4	M5/8 M5/8 S	M5/12	M5/16	M5/20 S	M5/24 S
Numero trefoli da 1/2"		4	8	12	16	20	24
Sezione nominale	cm ²	3,716	7,432	11,148	14,864	18,580	22,296
Peso teorico netto (soli trefoli)	Kg/m	2,94	5,87	8,81	11,75	14,68	17,62

Figure 41 - Prestressing tendon characteristics according to the Morandi system.

Further tests have been performed, by applying the prestressing through *Initial Strain* or *Initial Stress* materials to a grillage model representing a bridge deck of the same archetype. For this application, a four-beam 40m-span archetype has been chosen. Results of the different applications are not herein reported for the sake of brevity, but two main problems emerged from the tests. First, the application of prestressing through *Initial Strain* or *Stress* directly on the grillage model in OpenSeesPy software implies that the initial stress state is imposed on the entire structure at the same time. This in turn leads to the development of induced stresses related to hyperstatic effects in the grid model, due to the redistribution of stresses between the beams through the connecting diaphragms. If the beams have different sections, and hence different stiffnesses, these stresses alter the initial stress state of the structure. As will be discussed in the next sections, this is a typical situation in grillage models for girder-type PC bridge class, as the edge girders have a different cross-section compared to the central ones, due to the different effective slab lengths. In this regard, it is worth specifying that comparisons between the OpenSeesPy grillage fibre model and the SAP2000 grid linear elastic model have produced matching results for the application of prestressing in the abovementioned ways, similarly to the single beam case. Secondly, such a way to apply the prestressing stress to the structure implies that also the slab is involved in the prestressing process, but this is not true in real-world structures, as in these composite bridges the slab is cast only after the beam prestressing. These problems would lead to the unreliability of such a model for the purpose of analysis at serviceability limit

states. Indeed, a different prestressing simulation process would be needed in this last case, simulating a staged construction of the model, imposing the state of stress accumulated in the prestressing phase beam-by-beam, and imposing at the same time zero stress in the slab. This way, the analysis would produce truthful outcomes for the simulations.

However, in the case of ultimate limit state analysis, as of interest for the present thesis, the induced hyperstatic effects are negligible compared to the forces acting when the ultimate strength is reached. Furthermore, the effects of prestressing force in tendons at the ultimate limit state are negligible and the structure behaves like an ordinary RC structure, making the evaluation of the problem reliable. Future developments of this work will aim to overcome these initial problems, allowing the evaluation to be extended to the serviceability limit states.

Given the results of all the different tests, the *Initial Strain* material is chosen as the best way to apply the prestressing force in the FE fibre model. Such a choice is related to the greater pertinence of this modelling method to the actual post-tensioning process to a generic real structure, where tendons are effectively stretched before being anchored to the structural member. Furthermore, this wrapper material guarantees the lack of numerical problems during the displacement-control analysis, in contrast to the *Initial Stress* material, which proved to cause numerical issues in subsequent analysis on the PC bridges archetype models. Particularly, these numerical problems may emerge when, due to the random generation of realisation samples and the corrosion scenario adopted, the prestressing stress level reaches high values compared to the corrosion-affected yielding strength of the tendons.

7.2 Grillage model

Once the simulation method of prestressing effects on structure is selected, the FE numerical model can be generated by Python coding. As mentioned above, a plane grillage model is chosen to represent the structural response, seeking a balance between low computational effort and accuracy of the produced structural response. A

conceptual scheme of the workflow followed to generate the model is shown in Figure 42.

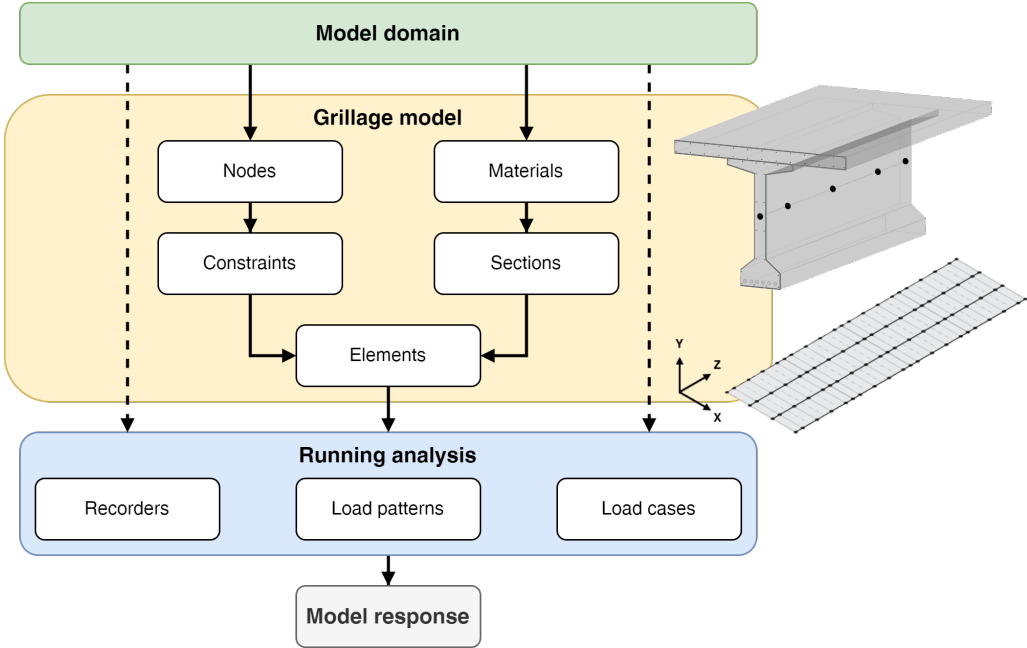


Figure 42 - Flowchart for FE model generation in OpenSeesPy.

The model is built by modelling longitudinal beams of the selected length, depending on the analysed archetype, and transversal elements simulating the connecting effect of diaphragms and the transversal contribution of the slab. A global right-handed OXYZ reference system is adopted for positioning the model in the space domain. The global Y-axis is conventionally chosen to develop along the gravity direction. Hence, the grillage model lies in the XZ plane.

In the longitudinal direction, i.e., the global X-axis, the principal elements are the beams. These elements are modelled as simply supported beams with one-dimensional elements through *nonlinearBeamColumn* element, available in OpenSeesPy (Pacific Earthquake Engineering Research Center (PEER), 2008; Zsarnóczy *et al.*, 2022). This kind of element is based on the iterative force-based formulation. A variety of numerical integration options can be used for this kind of element state determination and in this case the Gauss-Lobatto method is adopted (Davis and Rabinowitz, 1984), which

is also the default option provided by the software. Gauss-Lobatto integration is the most common approach for evaluating the response of force-based elements (Neuenhofer and Filippou, 1997) because it places an integration point at each end of the element, where bending moments are largest in the absence of interior element loads. In each element, the software places N Gauss-Lobatto integration points along the element. Particularly, it is advisable to adopt an odd number of integration points to properly get the element response and five integration points are adopted in the present work. The location and weight of each integration point are tabulated in references on numerical analysis (Abramowitz and Stegun, 1972). The force-deformation response at each integration point is defined by the section with a properly defined section tag, i.e., an integer number associated with each generated section typology.

In the transversal direction, i.e., the global Z-axis, the diaphragms linking the longitudinal beams are modelled through *nonlinearBeamColumn* elements as well. The number of integration points is the same as the one adopted for the beams, and all the abovementioned concepts equally apply to diaphragms. A number of five diaphragms, including the ones at supports, is chosen for the archetype, since this choice is deemed to give a high transverse flexural stiffness to the deck, similarly to the Courbon-Albenga assumption. This choice is adopted for the subsequent comparison with the results coming from the analytical model, but in future developments different number of diaphragms can be adopted, taking into account a lower number, to check the effects of lowering the number of diaphragms on the structural fragility. It is worth mentioning that, in this study, diaphragms are assumed detached from the slab, since this construction technique is common in Italy and applied in the case-study bridge types. This implies that the spacing of the transversal elements representing the slabs does not take into account an effective collaborating slab width at the diaphragm locations.

As far as the slab is concerned, its contribution is modelled in both X and Z global directions. Indeed, this structural element is a plane element which gives its contribution in both directions. Longitudinally, the slab contribution is modelled as merged in the beam elements, while in the transversal direction, its effect is modelled through appropriate one-dimensional elements independent from the diaphragms.

Particularly, an effective slab width contributing to the beam response is adopted in the longitudinal direction. This quantity is computed following the standards formulation taken from Eurocode EN 1992-1 Part 1: *General rules and rules for buildings* (CEN, 2004). In subsection 5.3.2.1, the European standards provide indications on the effective width of flanges to take into account when dealing with T-beam elements. Herein, the standards state that “In T-beams, the effective flange width, over which uniform conditions of stress can be assumed, depends on the web and flange dimensions, the type of loading, the span, the support conditions and the transverse reinforcement.”. The code provides the formulation to compute such an effective flange width, which in the present thesis corresponds to the slab width. The effective slab width b_{eff} may be accordingly derived through Equation (46). In this equation, $b_{eff,i}$ is computed through Equation (47), and all the other parameters are described in Figure 43 and Figure 44. In this case-study, i.e., accounting for only simply supported beams, the parameter l_0 coincides with the entire span length in each archetype. For this reason, it is evident that computing the effective slab width through these equations leads to big values of effective slab width. Hence, the limitation in Equation (47) implies that the effective slab width equals half of the beam spacing in all the cases. This is true for all the beams, but for the edge girders another limitation emerges. Indeed, for this kind of structure, it is common practice to design a cantilever slab having a shorter length than half of the beam spacing. For this reason, for the edge girders, the cantilever slab length governs the effective slab width to take into account, since this parameter cannot have a greater length than the actual existing slab.

$$b_{eff} = \sum b_{eff,i} + b_w \leq b \tag{46}$$

$$b_{eff,i} = 0.2b_i + 0.1l_0 \leq 0.2l_0; \quad b_{eff,i} \leq b_i \tag{47}$$

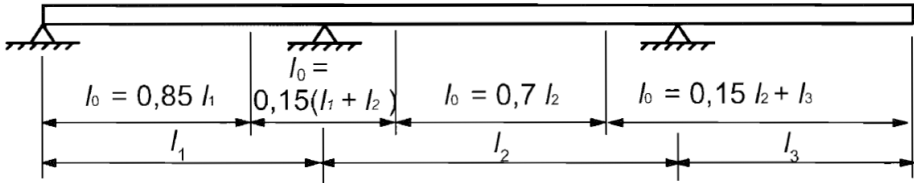
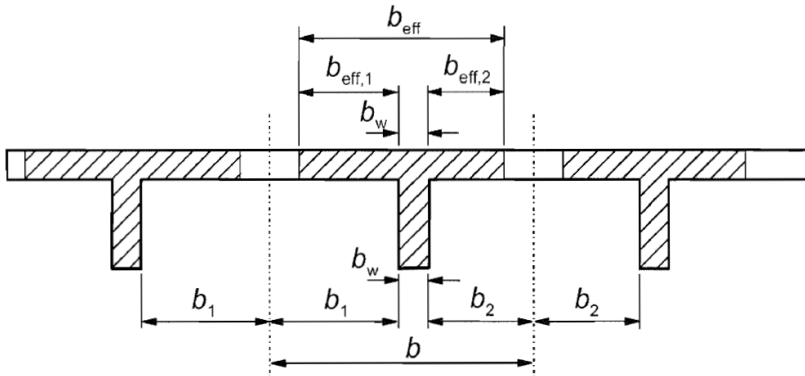

 Figure 43 - Definition of l_0 , for calculation of effective flange width (CEN, 2004).


Figure 44 - Effective flange width parameters (CEN, 2004).

As for the slab transversal contribution, each field between two consecutive diaphragms is divided into an integer number of slab bands. The width of these strips cannot be an integer number, as the length between the adopted archetypes may vary. For this reason, for the automatic generation of the models, a width that guarantees an integer number of bands in each field between two consecutive diaphragms and at the same time that is as close as possible to 3 metres is adopted. In this way, keeping a fixed number of five diaphragms per span, the slab width varies between 2.5 m, 3.3 m and 3.1 m for the 30m-, 40m- and 50m-span archetype, respectively. Such an automatic logic can be easily extended to every possible number of diaphragms. One-dimensional slab elements are then placed in correspondence with the axis of each obtained band. This choice guarantees a good balance between modelling simplicity and representativeness of the slab contribution, by avoiding a more complex and computationally demanding modelling strategy by adopting shell elements. Furthermore, such a choice follows what is prescribed in the literature on grillage models (Hambly, 1991).

Indeed, a convenient spacing for transverse grillage members is deemed to be equal to $1/4$ to $1/8$ of the effective span. In this study, values of about $1/10$, $1/12$ and $1/16$ of the effective span are obtained for 30m-, 40m- and 50m-span length, respectively.

A typical distribution of the nodes in the global geometry of the grillage model obtained following the abovementioned indications is represented in Figure 45 and Figure 46, where only the nodes are shown, placed in the XZ plane. In the figure, it is clearly shown the numbering system adopted for the nodes, i.e., arranged according to a matrix in which each node corresponds to three digits, the first of which corresponds to the row and the second and third to the column. This numbering allows the model to be extended to nine longitudinal elements and 99 transverse elements, limits that are very far from being achieved for modelling a real girder-type PC bridge structure.

In addition, other symbols are visible in the figure to point out the different meanings for each element. Particularly:

- A green little dot is used to represent the nodes between the longitudinal beam element and the transversal slab element.
- A blue dot is used to represent the nodes between the longitudinal beam element and the transversal diaphragm element.
- ▲ A red upward triangle is used to indicate a bearing which allows translational displacements along the z-axis (vertical direction in the figures).
- ▶ A red rightward triangle is used to indicate a bearing which allows translational displacements along the x-axis (horizontal direction in the figures).
- ✘ A red 45-degree-tilted cross is used to indicate a fixed bearing which prevents all the in-plane translational displacements.
- ✚ A red cross is used to indicate a bearing which allows all the in-plane translational displacements.

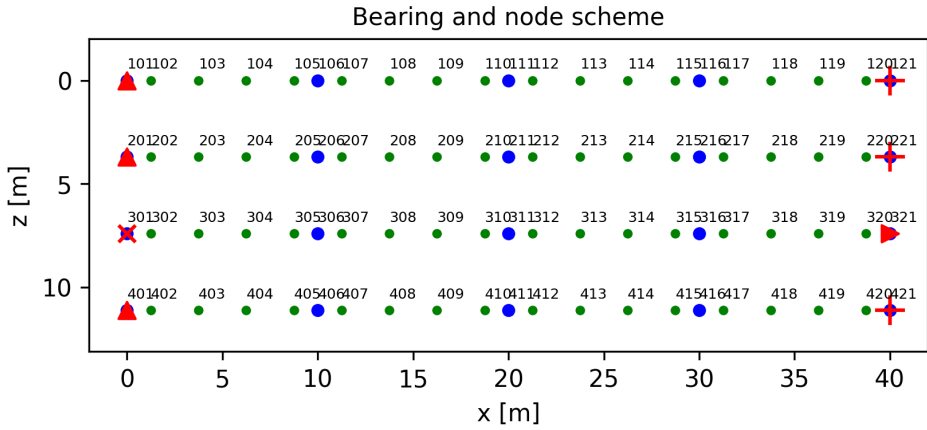


Figure 45 - Bearing and node scheme for the 40m-span, four-beam archetype.

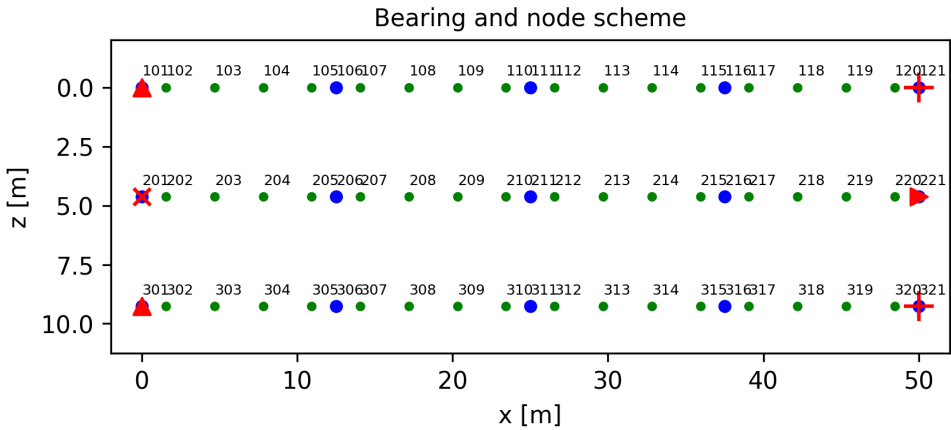


Figure 46 - Bearing and node scheme for the 50m-span, three-beam archetype.

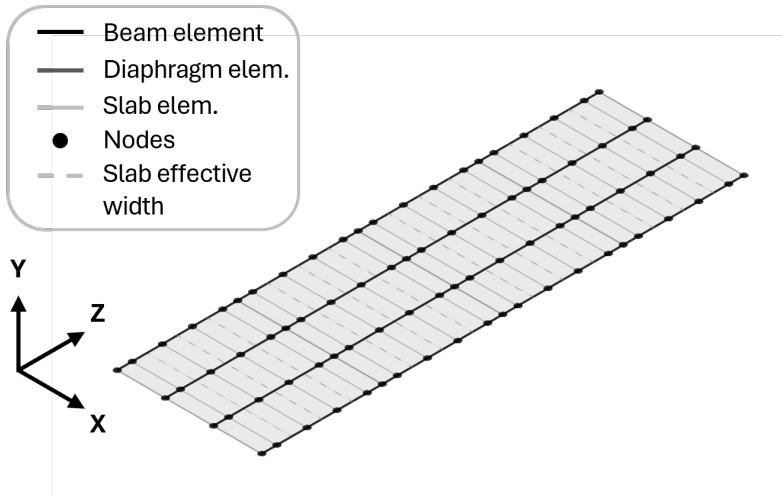


Figure 47 - Three-dimensional view of the grillage model in the reference space, a random realisation of the 40m-span, four-beam archetype.

7.3 Constitutive laws of materials

Once the global geometry is defined, appropriate material models need to be defined, i.e., concrete, mild reinforcement steel and prestressing steel. Obviously, the mechanical characteristics of the adopted materials vary in the same way as defined for the analytical model in Section 6.2. Herein, the chosen material models available in the OpenSeesPy library are listed. Before describing the material adopted in this work, it is worth mentioning that the general command for the generation of every material is called *uniaxialMaterial*. This command is used to construct a *uniaxialMaterial* object which represents uniaxial stress-strain (or force-deformation) relationships.

Regarding the concrete material, a *Concrete02* model is adopted (McKenna, Fenves and Scott, 2000; Zsarnóczyay *et al.*, 2022). The stress-strain relationship of this material model (Mohd Yassin and Mohd Hisham, 1994) is shown below in Figure 48. In the figure, f_{pc} is the concrete compressive strength at 28 days, eps_{c0} is the concrete strain at maximum strength, f_{pcu} is the concrete crushing strength, eps_U is the concrete strain at crushing strength, $lambda$ is the ratio between unloading slope at eps_{cu} and initial slope, f_t is the tensile strength and E_{ts} is the tension softening stiffness (i.e., the slope of the linear tension softening branch).

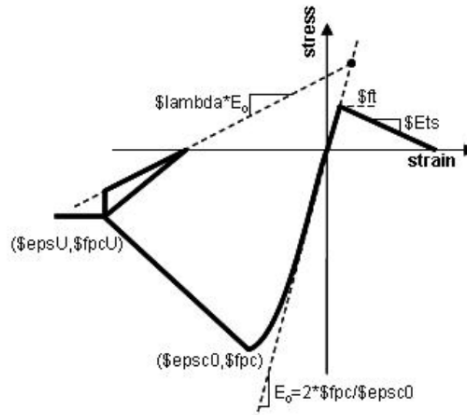


Figure 48 - *Concrete02* model in OpenSeesPy reference manual (Pacific Earthquake Engineering Research Center (PEER), 2008).

As for the compression side, the concrete parameters are chosen to take into account a parabola-rectangle concrete model suggested by the Italian building code (Ministero delle Infrastrutture e dei Trasporti, 2018). Tension-wise, the tensile strength is computed following the Italian code indications, while for the softening slope, the following logic is adopted. Since with values ranging from 50% to 20% of the compressive elastic modulus lots of convergence issues were encountered during the displacement-control analysis to failure, a very low value has been chosen for this parameter, about 1% of the compressive elastic modulus. This value ensures zero convergence problem for the analysis. To prevent an unreal too-strong tensile response of concrete, the tensile strength parameter has been reduced to 20% of the code-prescribed value. In this way, good correspondence of analysis results has been achieved compared to the case in which the code-prescribed tensile value is adopted, but with no longer convergence issue. It is worth specifying that these two parameters, i.e., the tensile concrete strength and the tensile softening slope, have negligible effects on the final response of the model, and hence these adjustments were found to be irrelevant to the outcome of the analyses.

As far as mild and prestressing steel materials are concerned, the same constitutive law exposed in Section 4.4 is adopted, again for the sake of comparison with

the fragility obtained through the analytical model. On the OpenSeesPy library, the corresponding material is defined as *Steel01* and is shown in Figure 49. In the figure, F_y is the yield strength, $E0$ is the initial elastic tangent and b is the strain-hardening ratio, i.e., the ratio between the post-yield tangent and the initial elastic tangent. As for mechanical parameters, the probability distributions listed in Table 4 in Section 6.2 are adopted. Modifications to the prestressing steel constitutive law are used according to indications provided in Section 5.2 and shown in Figure 35. For the reasons explained in Section 6.2, a zero-corrosion level is adopted for mild reinforcing steel.

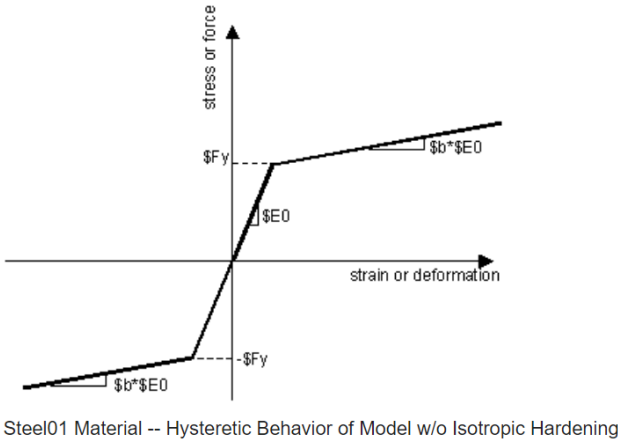


Figure 49 - Steel01 material: stress-strain relationship in OpenSees (Pacific Earthquake Engineering Research Center (PEER), 2008; Zsarnóczyay *et al.*, 2022).

Particularly, as mentioned in Section 7.1, a wrapper material *Initial Strain* (Pacific Earthquake Engineering Research Center (PEER), 2008; Zsarnóczyay *et al.*, 2022) is defined, to be wrapped on the prestressing *Steel01* material. As for the value of prestressing stress, the statistical distribution defined in Table 4 in Section 6.2 is adopted.

7.4 Section modelling via fibre-approach

After the generation of the global geometry and materials, the cross-section of every element type is defined. As mentioned in the previous section, in the longitudinal

direction, the contribution of the beams plus the slab on top needs to be taken into account for a reliable modelling of the deck response. For this reason, a fibre composite section is modelled, with the beam cross-section geometry at the bottom and the slab on top, accounting for the relative effective width computed according to Section 7.2. An example of the so-defined cross-section is shown in Figure 50. The beam in the figure belongs to the 40m-span, three-beam archetype. The figure clearly shows how the different parts of the cross-section are modelled through OpenSeesPy functions for fibre modelling. In grey, the concrete parts of the cross-section describe the main geometry, while the layers of mild reinforcement in the model are shown in red and the green dots at the bottom represent the six tendon fibres.

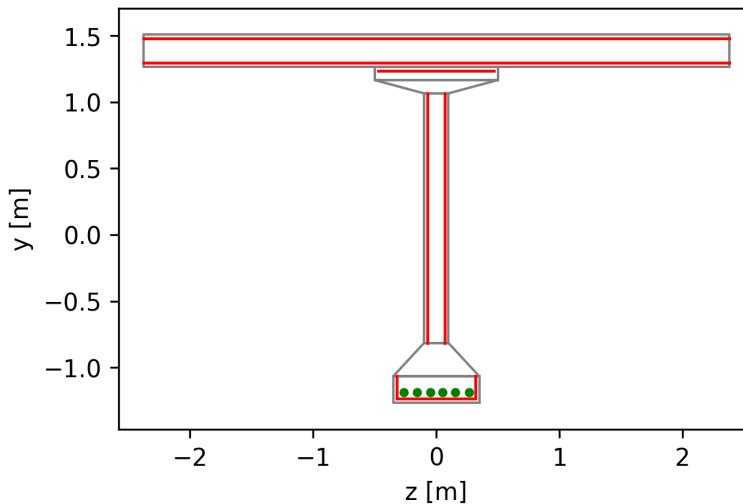


Figure 50 - A random beam cross-section of the 40m-span, three-beam archetype.

As for the concrete part, the section is conveniently divided into four-sided polygons, and each shape is separately modelled through the *patch* function for the fibre generation. This command is used to generate a number of fibres over a cross-sectional area. Particularly, three shapes of cross-section can be generated through this command: quadrilateral, rectangular and circular. In this case, different quadrilateral shapes are used for the cross-section generation. The software imposes specific rules to follow for the quadrilateral patch generation, e.g., the generation needs to be

performed following the quadrilateral perimeter, providing the coordinates of the four corners in a counterclockwise sequence. An idea of how the command works is given in Figure 51. In the figure, the four corners of the quadrilateral shape are defined as nodes *I*, *J*, *K* and *L*, with the relative coordinates, while the *numSubDiv* parameters represent the number of subdivisions for each side of the shape. Such a command allows a faster and more comfortable fibre generation, compared to a fibre-by-fibre generation.

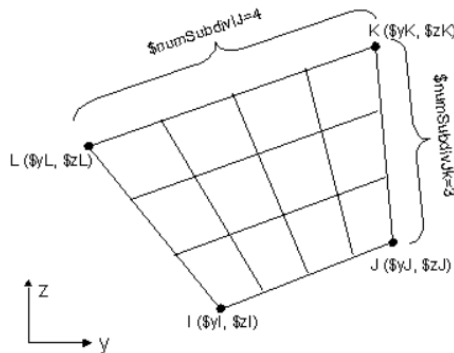


Figure 51 - *Patch* command in OpenSees (Pacific Earthquake Engineering Research Center (PEER), 2008; Zsarnóczy *et al.*, 2022).

As far as the mild reinforcement layers are concerned, the *layer* command is the best modelling choice. This function, as well as the *patch* command, allows the generation of multiple fibres in a single command. Particularly, the *layer* command generates a row of punctual fibres along a geometric arc, which can be a simple straight line or a circular arc. A representation of the command is given in Figure 52. The command requires the respect of precise rules for the layer generation, e.g. the definition must follow a line starting from one node, whose coordinates must be defined, and ending with another node, with its relative coordinates. The *numBars* parameter needs to be specified, i.e., the number of single fibres to arrange along the defined layer. This command perfectly fits the generation of mild reinforcement layers in a cross-section, and hence is herein used at this aim (red lines in Figure 50).

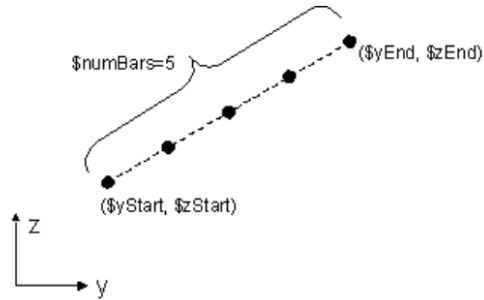


Figure 52 - *Layer* command in OpenSees (Pacific Earthquake Engineering Research Center (PEER), 2008; Zsarnóczyay *et al.*, 2022).

Finally, the *fiber* command is used to define the six punctual fibres simulating the steel tendons (in green in Figure 50). The function allows single-fibre modelling and placement following specific coordinates. The area of the punctual fibres needs to be defined for the generation through this command. In this case, this parameter naturally coincides with the area of a single steel tendon, as the total prestressing steel area is herein equally distributed among the six tendons.

Through these fibre modelling commands, two different beam cross-sections are defined, according to the variation of the effective slab width in the longitudinal direction (see Section 7.2). Particularly, a distinction is made between the edge girders and the central girders of the deck.

A typical moment-curvature curve of the midspan cross-section of a randomly generated realisation belonging to the 40m-span, four-beam archetype, is shown in Figure 53 below. Such a shape is obtained as a consequence of the listed choices of geometry and materials. In the figure, it is possible to note that the starting point of the moment-curvature relationship stands slightly below zero and has a negative value of the curvature χ_{mid} , due to the initial strain given by the prestressing action. Such a curve is obtained with a corrosion value ξ_p equal to zero.

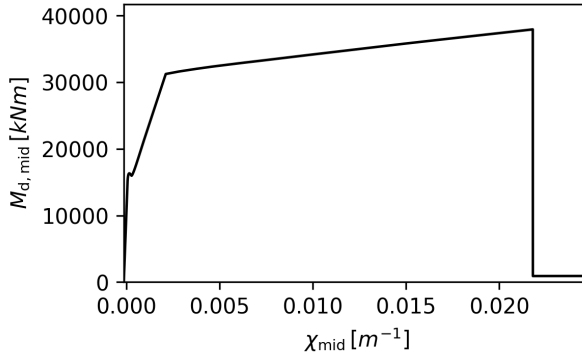


Figure 53 - Moment-curvature relationship for a random realisation of the 40m-span four-beam archetype.

As far as transversal direction elements are concerned, cross-section for diaphragms and slab elements needs to be defined. For diaphragms, which are non-linear elements as mentioned in Section 7.2, a simple rectangular RC section is herein adopted. These transversal linking elements are defined through fibre modelling, as well as the longitudinal beams. This allows a good representativeness of their distribution capacity of stresses among the beams. The methods for the generation of such a section are the same as listed above for the beam cross-section, i.e., *patch* command and *layer* command for the concrete main shape and mild reinforcement layers, respectively.

As for slab elements, it is assumed that these elements have a linear elastic response. This is because slab elements are assessed through appropriate local verifications, according to the standards. In this work, a global assessment is performed and, hence, the failure of slab elements can be neglected. For this reason, the slab is assumed to be able to distribute the load without achieving failure. Therefore, for the definition of the transversal slab-element section, the *section aggregator* command is adopted. This command is used to construct a *SectionAggregator* object which aggregates groups of previously defined *UniaxialMaterial* objects into a single section force-deformation model. Each *UniaxialMaterial* object represents the section force-deformation response for a particular section degree-of-freedom (DOF). Through this command, there is no interaction between responses in different DOF directions. The

command is described by a simple scheme in Figure 54. Taking advantage of this command, three *UniaxialMaterial* are defined for the slab elements, to be aggregated in the section, i.e., an *axial* material, a *flexural* material and a *torque* material. All three behaviours are defined as linear elastic, for this reason:

- The axial behaviour is simply defined through the product of the concrete elastic modulus E_c by the area of the rectangular section A_{slab} , with the transversal effective width of the slab equal to half of each transversal slab band (see Section 7.2).
- The flexural behaviour is defined through the product of the concrete elastic modulus E_c by the inertia of the rectangular section $I_{z,slab}$.
- The torsional behaviour is defined through the product of the concrete shear modulus G_c by the torsion coefficient of the section J_{slab} .

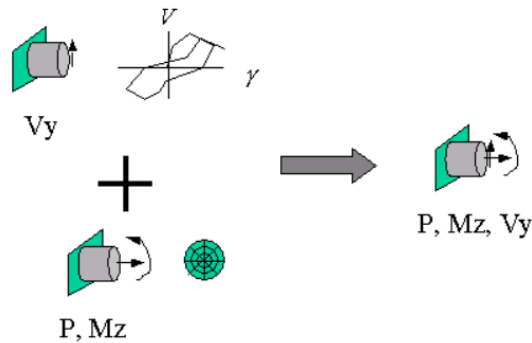


Figure 54 - *Section aggregator* command in OpenSees (Pacific Earthquake Engineering Research Center (PEER), 2008; Zsarnóczyay *et al.*, 2022).

The local geometric characteristics of each type of element are defined following the indications in Sections 6.1 and 6.2. Before switching to the discussion on load models, it is worth going into the details of the definition of the torsional behaviour of the selected elements. Regarding diaphragms and slab elements, the torsion coefficient can be easily computed through the simplified formula for rectangular shapes derived from the St Venant formulation in Equation (48), where b and d are the two sizes of the generic rectangle. This formula can undergo further simplification in the case of a thin

rectangle where $b > 5d$, given that b is the greater size of the rectangle, turning into the formula in Equation (49).

$$J = \frac{3b^3d^3}{10(b^2 + d^2)} \tag{48}$$

$$J = \frac{bd^3}{3} \tag{49}$$

However, finding the torsion constant of the beam cross-section can be tricky, due to its complicated shape. Literature references (Hambly, 1991) suggest that for many sections with re-entrant corners, the torsion coefficient J can be obtained with sufficient accuracy by notionally subdividing the cross-section into shapes without re-entrant corners and summing the values of the singles J obtained for the elementary shapes. A specific rule needs to be attended when subdividing the complicated shape, following the so-called “Prandtl’s membrane analogy”, described in Timoshenko and Goodier (Timoshenko and Goodier, 1970), and here described in Figure 55. Indeed, it is shown that the stiffness of a cross-sectional shape is proportional to the volume under an inflated bubble stretched across a hole of the same shape. The shear stress at any point is along the direction of the bubble’s contours and of magnitude proportional to the gradient at the right angles of the contours. If a cross-section is cut in a half, like in Figure 55 (e), the membrane is in effect held down along the cut, thus greatly reducing its volume and preventing the flow of shear stress along the contours from one part to the other. Consequently, when a cross-section is divided into different parts, like in Figure 55 (a), it is important to choose the elements so that they maximize the volume under their bubbles. To avoid giving the bubble zero height at the notional cuts, the elements can be rejoined at the cuts for calculations, as in Figure 55 (b). Since shear stresses flow across both ends of the web it can be thought of as part of a long thin rectangle for which Equation (49) holds. Figure 55 (c) and Figure 55 (d) also show the cross-section arbitrarily cut into rectangles which, by not trying to maximise the volume under the bubble, leads to a value of J equal to only half of the correct figure. It is worth noting that in the case of a thin open rectangle represented in this case by the

slab, which has a virtual delimitation on the shorter lateral sizes, the torsion coefficient can be conventionally taken as the half of the one of a closed thin rectangle described by Equation (49). This is due to the un-closed path of the shear stresses around the open contour of the element that leads to a loss in the shear stresses for an open cross-section as it is typical for the slab in a composite structure.

Following the abovementioned process, a randomly generated beam cross-section is split into four different parts, following the scheme in Figure 55 (f):

- 1) The top slab, element (1) in Figure 55 (f), representing an open rectangle, gives a contribution given by the formula $J_{slab} = bd^3/6$.
- 2) The top flange, element (2) in Figure 55 (f), is approximated at a rectangle with a width equal to the mean width of the top flange trapezium.
- 3) The web, element (3) in Figure 55 (f), has a simple rectangular shape and its torsion coefficient can be easily computed through Equation (48).
- 4) The bottom flange, element (4) in Figure 55 (f), can be approximated to a rectangle having a width equal to the mean width of the bottom flange trapezium.

The validity of these approximations has been proved by modelling a real beam cross-section on the software SAP2000 and by comparing the torsional coefficients obtained in the two different ways. The software provides the value of the torsional coefficient for a given cross-section of any shape. Comparing the two values showed an almost perfect matching between the torsional coefficient from SAP2000 and the approximated one, confirming the goodness of the adopted strategy.

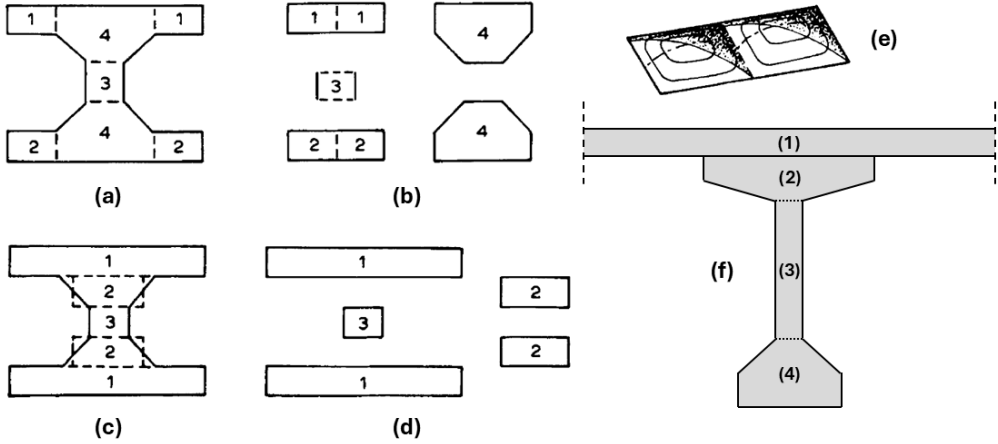


Figure 55 - Torsion coefficient computation.

7.5 Dead and traffic load patterns and cases

After the definition of the sections, the entire geometry of the model is defined. The hierarchy of the OpenSeesPy model follows a precise logic process. The materials previously defined are assigned to each section, and each section is assigned to an appropriate element. Each element spans between two previously defined consecutive nodes.

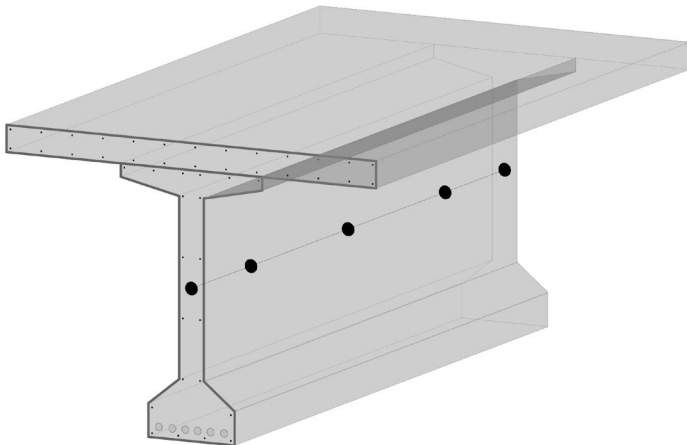


Figure 56 - Longitudinal beam element with five integration points.

Once the structure is generated, the loads must be applied to compute the relative induced stresses on the structure. Nodal and elemental loads can be defined in OpenSeesPy, through the commands *load* and *eleLoad*, respectively. In this model, the first command is used to define concentrated forces, while the second is for uniformly distributed loads acting on elements. Nodal loads can be applied directly on the nodes or, alternatively, on a certain location over a specific element, by defining its location relative to the first node of the element itself. Elemental load can only be defined on a specific element, and it is important to keep this in mind when defining the different loads acting on the structure.

As for structural dead loads, following the process described in Section 6.1, they can be easily defined mainly as uniformly distributed loads (UDLs) acting on elements. The beam self-weight, not including the relative effective slab portion on top, is assigned to the longitudinal element through UDL, as well as the diaphragm self-weight. Regarding the slab, considering its weight both in longitudinal and transversal elements would mean considering its self-weight as doubled. For this reason, its weight is assigned only to the transversal slab elements, whose function is to transfer their load on the longitudinal beam through the beam-slab connection nodes. The same logic can be followed by defining the non-structural dead loads, including the road pavement and the linear weight of the lateral road barriers. Specific attention needs to be paid to the loads acting on the slab cantilever. These can be transformed into an equivalent force system consisting of a vertical force plus the relative moment. In OpenSeesPy, it is impossible to model a linearly distributed moment load, and for this reason, the resulting moment and forces coming from the slab cantilever are computed and assigned to each correspondent node defined on the relative edge girder.

A different situation is the one regarding the traffic loads. Traffic load models to be applied to the superstructure have been deeply discussed in the appropriate Sections 4.1.1 and 4.1.2. As specified in Section 4.3.1, the scheme proposed by the Eurocode 1 – Part 2 (CEN, 2003) is herein adopted, and the scheme proposed by the Italian Guidelines (Consiglio Superiore dei Lavori Pubblici (CS.LL.PP.), 2020) are adopted as

alternative loads. Both the traffic models consist of two main loads, i.e., the uniformly distributed load and the tandem system.

The two models are pretty much the same in the application in OpenSeesPy if the UDL part is considered. UDLs are modelled as linearly distributed loads acting on the longitudinal axis of the code-prescribed distributed loads, i.e., the longitudinal axis of each notional lane. The axis of a notional lane does not fall exactly on a longitudinal beam, for this reason, it is impossible to define the traffic load coming from a notional lane with UDL. To solve this issue, the subdivision of the slab in transversal bands can be exploited. The resulting traffic force coming from the notional lane acting on a single band is computed, and each concentrated force is defined as acting on the relative transversal slab element, following the same logic process adopted for the transversal slab element definition (see Section 7.2). In this way, the notional lane loads are applied to the slab elements that are in charge of carrying the load to the longitudinal beams. A scheme describing the concentrated forces applied for simulating the Eurocode-based traffic model for a random realisation of the 40m-span, four-beam bridge archetype is shown in Figure 57.

Regarding the tandem system in the two traffic load models, two different ways are adopted for their application on the superstructure. Eurocode-conforming tandem loads are defined with a single concentrated load, acting alternatively at midspan or at the supports, for maximum flexure and shear demand, respectively (see Figure 57). Tandem systems conforming to the Italian Guidelines alternative loads are defined as a train of concentrated pairs of loads, simulating the axle of a generic vehicle, acting on the available nodes. To provide a graphical example, a second scheme representing the distribution of concentrated forces simulating the “heavy” traffic load model by the new Italian Guidelines is shown in Figure 58.

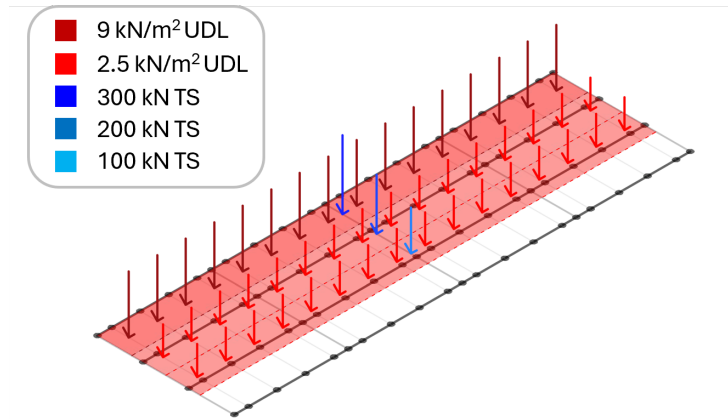


Figure 57 - Concentrated forces simulating the application of uniformly distributed loads (UDL) and tandem systems (TS) for the traffic model by Eurocode, an example on the 40m-span, four-beam archetype. Values in the legend refer to Table 2 in Section 4.1.1.

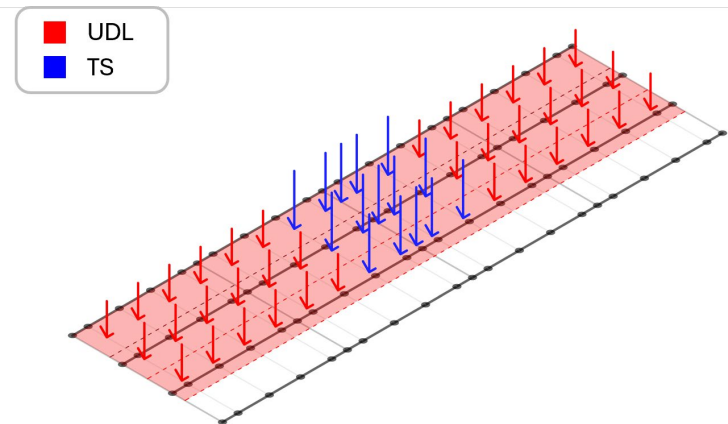


Figure 58 - Concentrated forces simulating the application of uniformly distributed loads (UDL) and tandem systems (TS) for the “heavy” traffic model by Italian Guidelines, an example on the 40m-span, four-beam archetype. Reference values for the load intensities are reported in Section 4.1.2.

OpenSeesPy software allows the user to perform static or dynamic analysis, through the *analysis* command (Pacific Earthquake Engineering Research Center (PEER), 2008; Zsarnóczay *et al.*, 2022). Particularly, three different types of analysis can be chosen among *static*, *transient* and *variable transient*. The first is intuitively understandable, the difference between the second and the third lies in the time step

used for the analysis. For the *transient* analysis the time step is set to be constant during the analysis, while for the *variable transient* one, the time step is considered variable. In this study, according to the nature of the loads acting on the superstructure of a bridge, the static analysis type is adopted.

To get the structural response, after the application of a load system on the structure, a system of equations needs to be solved. OpenSeesPy software solves the problem through a so-called *Integrator* object, which has different methods. The two main methods for a static integrator are *Load Control* and *Displacement Control*. Intuitively, the first method imposes a control of the load applied on the structure in different steps by an increasing factor. The second one does the same, by controlling the displacement. Particularly, the displacement-control command allows setting a displacement objective for a specified node, i.e., the control node, dividing the objective in different displacement steps by an amplification factor and forcing the equilibrium of the structure between internal and external forces at each step of the analysis. The equilibrium is achieved through different iterative algorithms, and OpenSeesPy gives the chance to pick a specific type of algorithm within different possibilities through the *algorithm* command. The best algorithm can change according to the specific problem, but it is of great importance to investigate this aspect to guarantee the analysis convergence at each step. The displacement-control analysis is the best choice to take the structure response into the plastic field and get its ultimate capacity. In this work, an assessment investigating the ultimate limit state of the structure is performed and, hence, this type of analysis is perfectly fit for the purpose.

The different loads are herein applied in different stages. First, the prestressing effects are applied to the structure. The software applies the initial strain to the structure (see Section 7.3), only after the first analysis is performed. For this reason, a first load-control analysis by applying a sort of “ghost load” to the structure, i.e., a distributed load of negligible intensity, is performed. This allows exercising a combination of effects on the structure, i.e., the initial strain plus a gravity load of very low intensity. Due to the negligible effects of the gravity load, the effects of prestressing can be read on the structure, which presents a counter-deflection at this stage, proportional to the

assigned initial strain. The load-control analysis is adopted for this stage, as the structural response surely does not exceed the elastic domain limit, and, hence, this kind of analysis rapidly converges in few steps. A deformed configuration of the structure after the application of prestressing actions is shown in Figure 59. The figure is obtained for an analysis of a random realization of the 40m-span, four-beam bridge archetype.

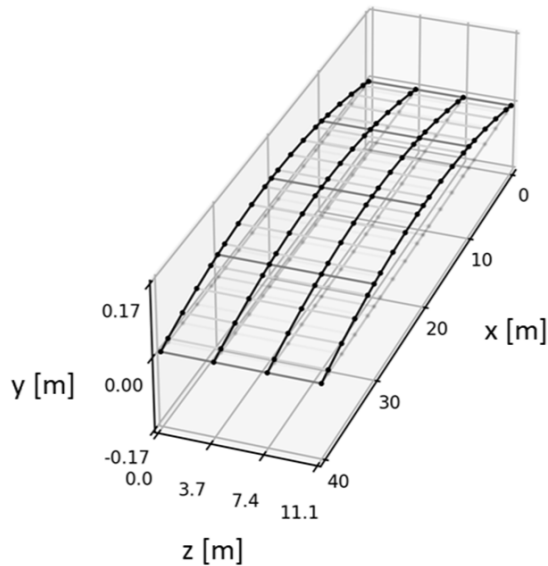


Figure 59 - Structure nodal displacements due to prestressing effects for a random realisation of the 40m-span, four-beam bridge archetype.

In a second stage, the dead loads are applied to the structure. At this stage, the structural response may exceed the elastic threshold in some scenarios, e.g. a high corrosion level scenario can trigger an early failure due to only dead loads. For this reason, a displacement-control analysis is adopted to run this stage. A representation of the dead load effects computed for the same archetype random realisation shown in Figure 59 is provided below in Figure 60. It is worth noting that, with the application of the dead loads, the initial counter-deflection is almost zeroed out, and the same applies to many other realisations.

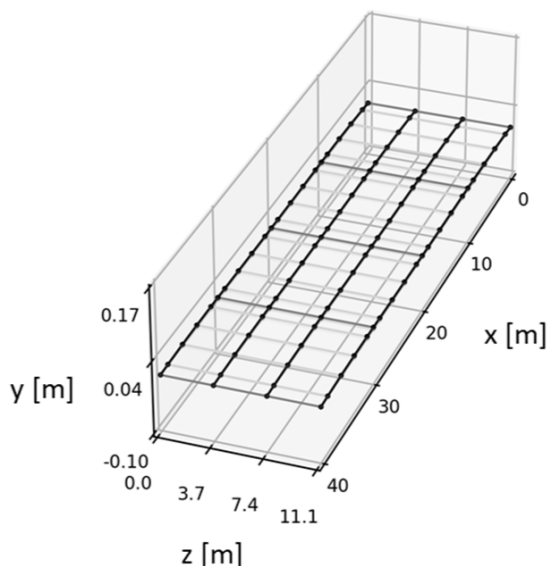


Figure 60 - Structure nodal displacements due to dead loads for a random realisation of the 40m-span, four-beam bridge archetype.

Lastly, traffic loads are applied in a final stage, if dead load failure has not occurred. Most probably, depending on the amplification factor adopted for the analysis, at this stage, the structure goes beyond the elastic domain limit. For this reason, again displacement-control analysis is needed. In Figure 61, the deformed configuration of the same archetype random realisation described in the two previous figures is shown. Such a displacement is reached after the application of a traffic load combination that maximises the flexural response at the mid-span of the edge girder, with an amplification factor that doubles the load. The corrosion scenario adopted for the analysis in the figure is a 5%-level corrosion scenario.

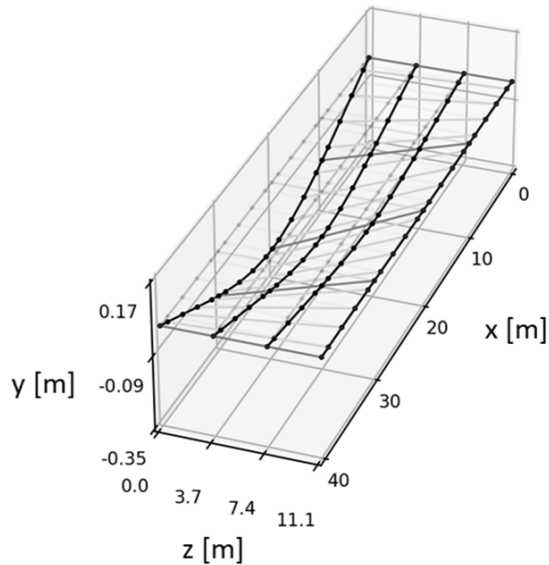


Figure 61 - Structure nodal displacements due to traffic load combination maximising flexure at midspan for a random realisation of the 40m-span, four-beam bridge archetype, given a 5%-corrosion scenario and amplification factor for traffic loads equal to 2.

With displacement-control analysis, the maximum bending moment at midspan and the maximum shear stress at the support zone are computed at each step of the analysis. Once the analysis has started, two different controls are performed during the process. Indeed, the vertical downwards push is stopped when either the load has reached the desired intensity (without any failure), or the first cross-section fails before getting to the pre-set intensity. This last condition corresponds to a demand-to-capacity ratio (DCR) exceeding the unit value, allowing the fragility curve construction process described in Section 4.5.

8 RESULTS AND DISCUSSION

In this section, the results in terms of fragility curves and points are presented. Particularly, the first part presents the fragility results derived from the application of the traffic models prescribed by Eurocode 1 – Part 2 (CEN, 2003), which are the same as in the Italian building code (Ministero delle Infrastrutture e dei Trasporti, 2018). In the second and last parts, results in terms of fragility coming from the application of the alternative traffic load models proposed by the new Italian Guidelines (Consiglio Superiore dei Lavori Pubblici (CS.LL.PP.), 2020) are presented. A brief discussion of the most interesting outcomes is proposed in each section.

8.1 “Corrosion-affected fragility” curves accounting for the Eurocode-based traffic model

In this section, fragility results obtained through the application of the Eurocode-based traffic load models are presented. Results are graphically shown and discussed according to the two proposed different modelling strategies, i.e., the simplified analytical model and the refined FE model. Then, a comparison of the obtained results is performed, highlighting the main differences and understanding their nature. Finally, a brief discussion on the fragility coming separately from the two analysed failure mechanisms, i.e., flexure and shear failure, is proposed.

8.1.1 Fragility curves via simplified analytical model fragility

The results in terms of fragility curves to traffic loads obtained from the simplified analytical modelling strategy are computed and discussed in this subsection, mainly focusing on two aspects: (a) the influence of span length and number of beams characterising the investigated PC bridge archetypes and (b) the influence of different corrosion scenarios (ξ_p). The discussion aims to derive indications to address bridge prioritisation in the analysed simulated bridge network.

Before showing the results, it is worth mentioning the rationale behind the selection of the load amplification factors, i.e., the traffic-load intensity measure (IM) values. In the simplified analytical modelling strategy, traffic load analyses are performed

by varying the traffic load amplification factor from 0 to 5, at a step size of 0.01. Such values are chosen to obtain a high resolution for the fragility dataset. Computational-cost-wise, this is not the best choice to keep the probabilistic assessment procedure fast and cheap. However, the analytical model equations are so easy-to-solve for an ordinary computer, that such a high number of analyses can be run in few minutes. The maximum amplification factor is fixed to 5, because a failure probability equal to one is reached for all the different archetypes at this traffic load value.

The results of the analyses are shown in Table 7, Table 8 and Table 9, which report the median and dispersion of the lognormal cumulative density function representing fragility curves, and Figure 63, Figure 64 and Figure 65, in graphical form. Indeed, the lognormal cumulative distribution function (CDF) was found to fit perfectly the fragility dataset obtained through this simplified procedure. Fragility curves are computed for ξ_p ranging between 0 and 20%, and span lengths equal to 30, 40 and 50 m. Such a range of corrosion values has been chosen because they are compatible with the corrosion values of the specimens experimentally tested by Yu et al. (Yu et al., 2022), from which the herein-adopted corrosion-affected stress-strain relationship has been derived. In addition, a corrosion degree ξ_p equal to 25% has been investigated, but most of the model realisations in the analysed sample failed due to self-weight at this very high corrosion level, preventing the computation of fragility curves. Figure 62 presents an example of the stress-strain relationship modification of corroded prestressing tendons related to a randomly extracted bridge-archetype realisation.

Fragility analysis of prestressed concrete bridges affected by corrosion under traffic loads

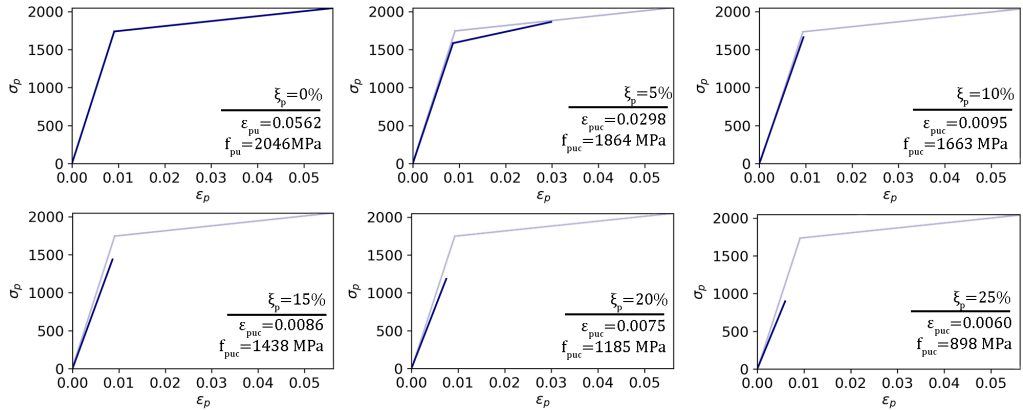


Figure 62 - Modifications of the prestressing steel stress-strain relationship due to corrosion for a random bridge-archetype realisation.

Table 7 - Fragility parameters corresponding to 30 m-span bridge.

ξ_p [%]	Median		Dispersion	
	Three-beam	Four-beam	Three-beam	Four-beam
0	1.69	1.69	0.154	0.119
5	1.60	1.59	0.161	0.127
10	1.31	1.30	0.189	0.167
15	0.93	0.93	0.230	0.200
20	0.54	0.54	0.320	0.297

Table 8 - Fragility parameters corresponding to 40 m-span bridge.

ξ_p [%]	Median		Dispersion	
	Three-beam	Four-beam	Three-beam	Four-beam
0	1.55	1.60	0.150	0.136
5	1.49	1.55	0.149	0.138
10	1.37	1.41	0.158	0.146
15	0.99	1.02	0.218	0.213
20	0.55	0.55	0.335	0.342

Table 9 - Fragility parameters corresponding to 50 m-span bridge.

ξ_p [%]	Median		Dispersion	
	Three-beam	Four-beam	Three-beam	Four-beam
0	1.44	1.51	0.169	0.158
5	1.39	1.46	0.173	0.161
10	1.33	1.39	0.173	0.159
15	1.06	1.12	0.213	0.205
20	0.57	0.58	0.372	0.401

First, the obtained fragility curves related to $\xi_p = 0\%$ (Figure 63, Figure 64 and Figure 65) show that the highest value of the probability of failure, considering the traffic load multiplier $\alpha = 1$, is related to the 50m-long span superstructure typology with three beams, which is a few more than 3%. Instead, a probability of failure equal to about 0.5% is observed for the four-beam and 50m-span typology, and lower for the other archetypes. These significant values of failure probability in absence of corrosion can be related to: 1) the difference in the traffic load model adopted to carry out the fragility analysis with respect to the one prescribed in the old design code; 2) the underestimation of capacity deriving from the models adopted for propagating the uncertainty which can be not accurate for 50m-span PC bridges. Some of these models, described in Table 4 and Table 5, are derived from a bridge sample in which such high span length values are rarely recorded, making their application to the 50m-span length likely unreliable. Furthermore, as highlighted in the following by analysing the fragility curves considering only flexural and shear failure, such a high value of failure probability is determined by the shear failure mode and may be related also to the conservative estimation of the shear capacity obtained from the shear model herein considered. Future research advances aimed at structural data collection can be useful for deriving more accurate estimations of capacity for the investigated bridge typologies, in particular for the higher span values. These results preliminary show that, in the absence of corrosion, and assuming the reliability of the models adopted for the propagation of knowledge-based uncertainties (Table 4 and Table 5), priority should be related to bridges having the highest span length value. This outcome, enhancing the fragility of

long-span PC bridges with respect to the other cases, can be used to revise the prescriptions of the new Italian Guidelines on the structural safety of existing bridges (Consiglio Superiore dei Lavori Pubblici (CS.LL.PP.), 2020) which assign a homogeneous vulnerability class to bridges with a span length value higher than 25 m. It is worth highlighting that this conclusion, as based on the above-listed assumptions, needs to be verified, for instance, with deeper analyses of examples of real bridges.

The increase in the corrosion level significantly affects the superstructure's performance. Results show that the analysed bridge typologies show a relevant increase in fragility for $\alpha = 1$ when the corrosion level exceeds values around 10%. Indeed, the probability of failure related to $\xi_p = 10\%$ increases up to significant values for all the typologies. This may be related to the loss of the plastic branch in the corroded prestressing steel stress-strain relationship (see Figure 62) which starts to occur for corrosion values in the range of 8% (see Section 4.4). At $\xi_p = 15\%$, there is a relevant drop in bridge performance. Indeed, the probability of failure for $\alpha = 1$ exceeds about 30% for all the analysed bridge typologies. It is worth noting that a corrosion level equal to 15% approximately corresponds to the loss of almost an entire strand area over a wide-spread seven-strand steel tendon. If a corrosion degree increment from $\xi_p = 0\%$ to $\xi_p = 15\%$ is analysed, the fragility medians (reflecting the α value related to the probability of failure equal to 50%) show a reduction equal to 45%, 36% and 26% for the 30m-, 40m- and 50m-span archetypes, respectively, regardless of the number of beams. Therefore, while dealing with the prioritisation of special inspections, in presence of expected corrosion, greater priority should be given to the shortest span typology in the simulated road network. The reduction of the fragility curve medians for an increasing corrosion value from $\xi_p = 0\%$ to $\xi_p = 20\%$ remains approximately constant and ranges from 60% to 70% for all the archetypes. According to the assumptions of the simplified analysis adopted in the analytical method, the number of beams seems to be a negligible parameter in fragility-informed prioritisation in presence of corrosion. Indeed, by observing Table 7, Table 8 and Table 9, the medians of fragility curves for typologies with the same span length but different values of the number of beams have quite constant values.

Considering these results, transport managers' operators can define priority lists for addressing appropriate inspections of the prestressing steel components. For example, a ranking can be computed based on the increase in fragility (failure probability) for a given value of traffic load intensity $\bar{\alpha}$, between the no-corrosion scenario and one in which an expected corrosion value $\bar{\xi}_p$ is defined, for instance, based on similar corrosion values recorded in the same region in past surveys or based on probabilistic corrosion evolution models in the area. If traffic limitations exist on the analysed road network, the traffic load multiplier value $\bar{\alpha}$ adopted for prioritisation should be selected to reflect the allowable total load value that can travel on the investigated bridge portfolio.

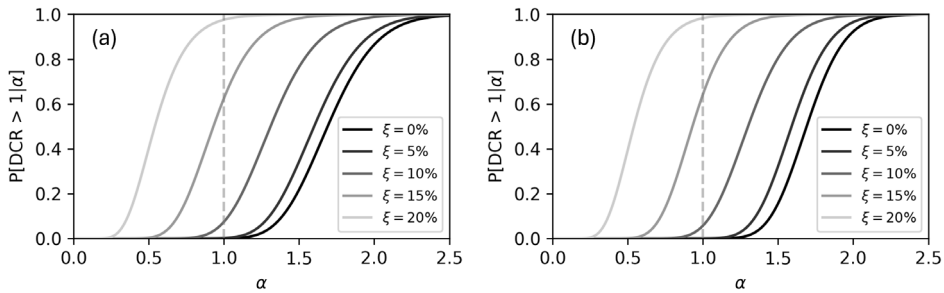


Figure 63 – Analytical-model fragility curves for (a) three- and (b) four-beam, 30 m-span archetypes.

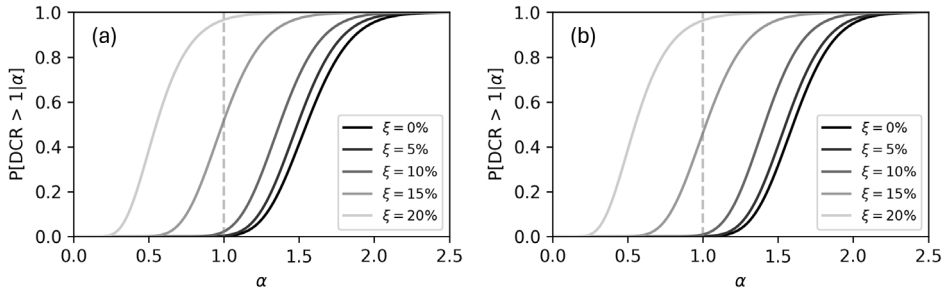


Figure 64 – Analytical-model fragility curves for (a) three- and (b) four-beam, 40 m-span archetypes.

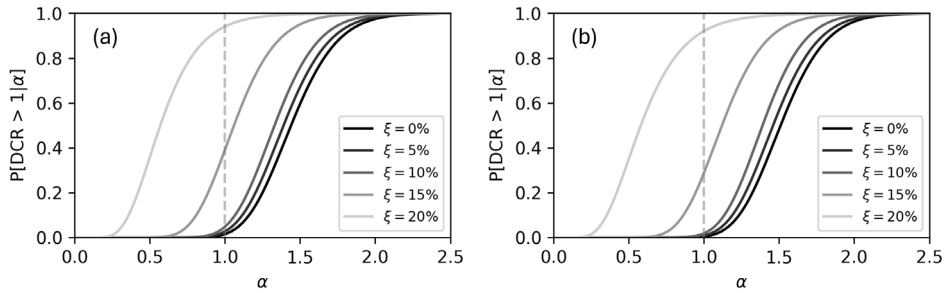


Figure 65 – Analytical-model fragility curves for (a) three- and (b) four-beam, 50 m-span archetypes.

The results in Table 7, Table 8 and Table 9 report the dispersion values. For $\xi_p = 0$, the dispersion ranges between 0.11 to 0.17, indicating that the influence of uncertain parameters is approximately constant for the analysed bridge typologies. Focusing on the influence related to corrosion, dispersion values increase by increasing the corrosion level ξ_p for all the typologies. The reason may lie in the combination of the flexure and shear failure mechanisms, which will be clarified in the following section. Indeed, as corrosion increases, the flexural failure mechanism becomes dominant. Due to the greater variability of fragility curves associated with flexural failure mechanism with respect to the ones related to shear failure, at high level of corrosion the fragility curves tend to show a higher variability.

Some considerations may be derived by analysing the most critical mechanisms leading to the fragility of the investigated bridge typologies. To this aim, the fragility curves expressing the probability of exceedance of DCR_f , DCR_s related to flexure and shear response, respectively, are defined according to the algorithm in Section 4.5. Results are briefly reported in Table 10, Table 11 and Table 12 (in terms of medians, only) and in Figure 66, Figure 67 and Figure 68.

Table 10 - Flexural and shear fragility curve medians (α value corresponding to 50% failure probability) for three- and four-beams, 30 m-span bridges.

ξ_p [%]	Three-beam		Four-beam	
	Flexure	Shear	Flexure	Shear
0	1.92	1.70	1.90	1.70
10	1.31	1.62	1.31	1.62
20	0.54	1.53	0.54	1.54

Table 11 - Flexural and shear fragility curve medians (α value corresponding to 50% failure probability) for three- and four-beam, 40 m-span bridges.

ξ_p [%]	Three-beam		Four-beam	
	Flexure	Shear	Flexure	Shear
0	2.15	1.55	2.23	1.60
10	1.44	1.46	1.48	1.50
20	0.55	1.36	0.55	1.40

Table 12 - Flexural and shear fragility curve medians (α value corresponding to 50% failure probability) for three- and four-beam, 50 m-span bridges.

ξ_p [%]	Three-beam		Four-beam	
	Flexure	Shear	Flexure	Shear
0	2.44	1.44	2.57	1.51
10	1.59	1.34	1.68	1.40
20	0.57	1.23	0.58	1.29

The fragility curves in Figure 66, Figure 67 and Figure 68 for the two different flexural and shear failure modes show that for $\xi_p = 0\%$ the probability related to shear failure is higher than the flexure one for all the bridge typology, meaning that the most recurrent failure mode of the bridge realisations under a given traffic demand is related to shear at supports, as anticipated above. However, for the analysed case studies, considering the models adopted for the beam geometry and constructive details, for high span length the shear failure type becomes increasingly dangerous with respect to flexure ones, as shown looking at the medians of the fragility curves in Table 10, Table 11 and Table 12. The generalisation of this outcome for other cases belonging to

the post-tensioned PC bridge class requires further analyses in which the influence of other beam geometric characteristics is analysed, e.g. cross-section shape and area or beam web thickness variation, and more refined capacity models are employed, for example, concerning the consideration of the beneficial effect on shear demand of the tendon uplift at the supports.

Conversely, as shown by Figure 66, Figure 67 and Figure 68, by increasing the corrosion level, the flexural failure tends to overwhelm the shear failure for all the bridge typologies. This is related to the decrease caused in flexural capacity by corrosion as modelled in the current procedure, i.e., modifications of the steel tendon stress-strain relationship and steel area reduction. On the other hand, the adopted corrosion model has a lower influence on shear strength, contributing only to the mean compression state of the beam cross-section. For example, as shown in Table 12, for the 50m-span three-beam archetype, the α related to the median fragility for flexural failure exhibits a percentage reduction of -35% and -77% for $\xi_p = 10\%$ and $\xi_p = 20\%$, respectively. Conversely, the percentage reduction of median fragility for shear failure is strongly lower, reaching -14% for $\xi_p = 20\%$.

It is worth specifying that despite flexural failure is generally considered a ductile mechanism, this cannot be stated for the adopted critical corrosion level scenarios, as high corrosion involves relevant ductility loss for corroded steel. Indeed, with the corrosion model implemented in this work, steel nonlinear deformation capacity is completely lost beyond 8-10% of corrosion degree, which implies the occurrence of brittle failures (as occurs in every scenario when considering higher corrosion levels).

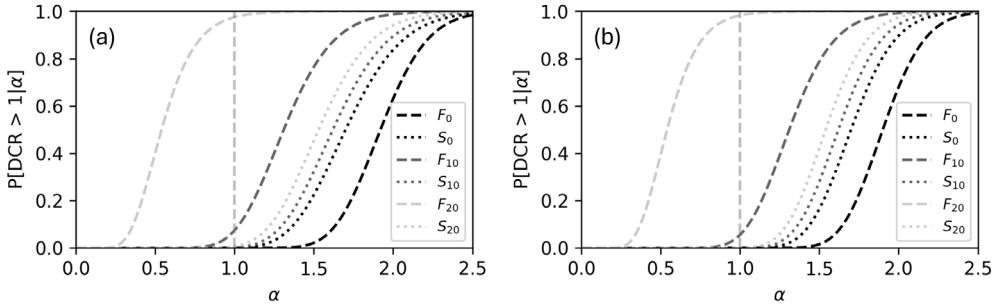


Figure 66 - Flexural and shear fragility curves for (a) three- and (b) four-beam, 30 m-span bridges. Legend: F – flexure; S – shear; 0, 10, 20 – 0%, 10% and 20% of corrosion level.

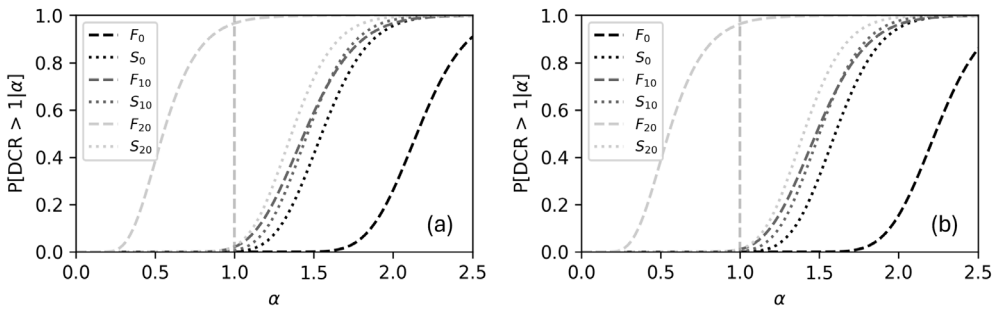


Figure 67 - Flexural and shear fragility curves for (a) three- and (b) four-beam, 40 m-span bridges. Legend: F – flexure; S – shear; 0, 10, 20 – 0%, 10% and 20% of corrosion level.

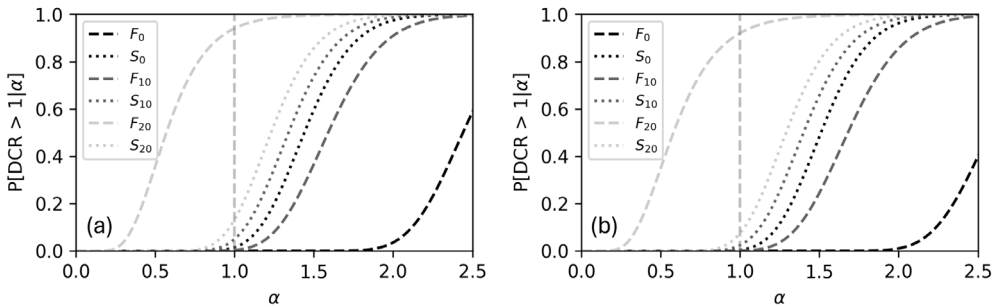


Figure 68 - Flexural and shear fragility curves for (a) three and (b) four-beam, 50 m-span bridges. Legend: F – flexure; S – shear; 0, 10, 20 – 0%, 10% and 20% of corrosion level.

The importance of modelling both flexural and shear contributions comes out from this analysis. Indeed, it is not possible to establish a priori which one is the most

critical failure mechanism. Regarding surveys and in particular special inspections, it is recommended to investigate all beam critical cross-sections, i.e., at mid-span and at support zones. Besides, from the findings of this work, particular attention should be given to the mid-span region of the beams in presence of corrosion, as flexural failure turns out to be the “weakest” mechanism.

8.1.2 Fragility curves via FE model fragility

In this subsection, fragility results obtained via the refined FE modelling strategy are presented. Differently from the simplified methodology (see previous section for details), the analysis for a random realisation of a bridge adopting the refined FE model requires more time and computational cost. Precisely, the time for running a single analysis varies according to the archetype model, the selected step size for the displacement-control analysis and the selected load amplification factor, which determines the end of the analysis when no failure is reached. On average, a single analysis requires few seconds to be performed on a powerful computer, and running millions of analyses without caring about time and computational efforts is not convenient. For this reason, only few values of traffic load amplification factors are selected in this strategy. Particularly, 11 different values ranging from 0.5 to 4.5 are selected, obtained by dividing the interval into steps of 0.5 and adding two more values in the range from 1 to 2, to have a better fragility curve resolution for values around the code-prescribed traffic load. Following this logic, the selected IM values are [0.50, 1.00, 1.25, 1.50, 1.75, 2.00, 2.50, 3.00, 3.50, 4.00, 4.50]. Such a high maximum amplification factor is chosen to guarantee a high probability of failure for all the archetypes.

Moreover, it is worth noting that for this strategy, the lognormal CDF is not always suitable for fitting the obtained fragility dataset for all the archetypes. With such a few points in the fragility dataset, the maximum likelihood method is adopted for seeking the best fitting, differently from the method of moments adopted for the fragility dataset fitting obtained through the simplified modelling strategy. In some cases, especially for high values of corrosion ξ_p , i.e., beyond 15%, the method is not able to converge and find an optimised solution for the parameters describing the fitting lognormal

CDF. In all the other cases the fitting can be performed with a lognormal CDF. However, the best fitting is provided for all the archetypes and all the corrosion scenarios by the Generalized Extreme Value (GEV) distribution.

Given the importance of analysing separately the two failure mechanisms, whose combination turns out to be decisive for wholly understanding the processes underlying the vulnerability of a generic archetype, the FE analysis is performed keeping the distinction between the two failure modes.

Results achieved for the flexural failure mode investigation are shown in Figure 69, Figure 70 and Figure 71 and relative GEV distribution parameters are reported in Table 13, Table 14, Table 15, Table 16, Table 17 and Table 18.

Table 13 - GEV distribution parameter for flexural fragility curves of 30m-span, three-beam archetype.

ξ_p [%]	Shape κ	Scale Ψ	Location θ	Median	Dispersion
0	-0.082	0.402	3.154	3.304	0.170
5	-0.365	0.287	2.658	2.770	0.306
10	-0.307	0.319	1.763	1.887	0.382
15	0.117	0.284	1.376	1.479	0.320
20	0.038	0.248	0.842	0.932	0.304

Table 14 - GEV distribution parameter for flexural fragility curves of 30m-span, four-beam archetype.

ξ_p [%]	Shape κ	Scale Ψ	Location θ	Median	Dispersion
0	0.195	0.463	3.300	3.464	0.140
5	0.043	0.412	2.765	2.915	0.168
10	-0.047	0.333	1.748	1.871	0.233
15	0.220	0.302	1.343	1.449	0.214
20	0.201	0.233	0.866	0.949	0.255

Table 15 - GEV distribution parameter for flexural fragility curves of 40m-span, three-beam archetype.

ξ_p [%]	Shape κ	Scale Ψ	Location θ	Median	Dispersion
0	0.213	0.458	3.572	3.733	0.127
5	0.172	0.526	2.824	3.011	0.185
10	0.157	0.392	1.678	1.818	0.230
15	0.021	0.254	1.223	1.316	0.232
20	0.280	0.222	0.779	0.857	0.259

Table 16 - GEV distribution parameter for flexural fragility curves of 40m-span, four-beam archetype.

ξ_p [%]	Shape κ	Scale Ψ	Location θ	Median	Dispersion
0	0.146	0.449	3.452	3.612	0.134
5	0.194	0.508	2.880	3.060	0.173
10	0.243	0.373	1.713	1.844	0.205
15	0.074	0.241	1.224	1.312	0.210
20	0.280	0.219	0.752	0.828	0.219

Table 17 - GEV distribution parameter for flexural fragility curves of 50m-span, three-beam archetype.

ξ_p [%]	Shape κ	Scale Ψ	Location θ	Median	Dispersion
0	0.310	0.487	3.821	3.989	0.120
5	0.180	0.521	2.995	3.180	0.173
10	0.140	0.378	1.824	1.959	0.208
15	0.164	0.299	1.264	1.371	0.232
20	0.095	0.218	0.710	0.789	0.306

Table 18 - GEV distribution parameter for flexural fragility curves of 50m-span, four-beam archetype.

ξ_p [%]	Shape κ	Scale Ψ	Location θ	Median	Dispersion
0	0.163	0.428	3.579	3.731	0.123
5	0.288	0.505	3.143	3.319	0.151
10	0.243	0.373	1.885	2.015	0.188
15	0.168	0.286	1.289	1.391	0.218
20	0.173	0.221	0.710	0.789	0.295

The tables above show the results in terms of the three parameters of the GEV distribution that best fit the obtained flexural fragility points. For the un-corroded

configuration, the 30m-span typology, with either three or four beams, presents the highest flexural failure probability. Such a consideration comes from the observation only of the fragility curve medians, as in this case, if the probability of flexural failure for the code-conforming traffic load, i.e., $\alpha = 1$, are analysed, their values turn out to be non-significant. Indeed, flexural failure at this load amplification factor is very far from occurring for all the archetypes, and the same applies to the flexural fragility curves obtained through the simplified analytical (SA) procedure. However, significant differences can be highlighted between the values of flexural failure probability obtained through the two procedures. The reasons behind such differences will be deeply discussed in the following Section 8.1.3.

About the un-corroded configuration, for FE analysis, as well as for the SA procedure, results show that the number of beams of the archetype does not significantly affect the results in case of zero level of corrosion. Nevertheless, a slightly more pronounced difference in the medians may be highlighted for FE analysis, equal to about 5% for all the archetypes, probably due to the introduction into the model of the load redistribution capacity among the different beams, not possible with the SA procedure adopting the Courbon-Albenga method for load redistribution.

As far as corrosion influence on flexural response is concerned, Figure 69, Figure 70 and Figure 71 clearly prove that fragility is highly affected by tendon degradation, indistinctly for all the archetypes. Particularly, a big drop in bridge performances can be noted between 5% and 10% of corrosion. This may be related to the loss of the plastic branch of the steel tendon, which for the different bridge realisations occurs on average at 8% of corrosion, as stated in Section 5.2. Percentage reductions of fragility curve medians are approximately the same for all the archetypes. Indeed, for a corrosion increase from 0 to 10%, a quite constant value of 45-50% decrease is found for the fragility curve median, whereas, considering an increase in corrosion from 0 to 15%, a 60-65% of decrease in the median values holds for all the archetypes.

Dispersion values associated with flexural fragility curves are not that high, as well as fragility curves produced through the SA procedure, showing low variability in archetype responses. However, dispersion values increase with corrosion, showing

that for high tendon degradation the response may be more uncertain. For this modelling strategy, this could be related to the multiplication factors adopted for modelling corrosion effects, which modifies the steel tendon area and the prestressing steel mechanical characteristics, enhancing the variability in the response among the different realisations of the same bridge typology.

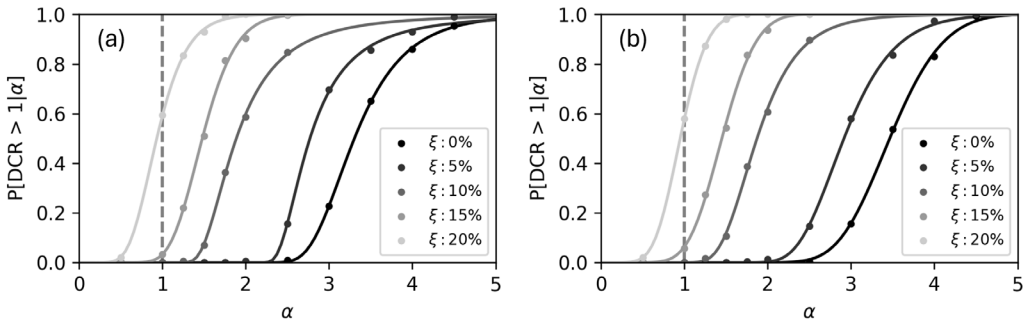


Figure 69 – FE-model fragility curves for (a) three- and (b) four-beam, 30 m-span archetypes.

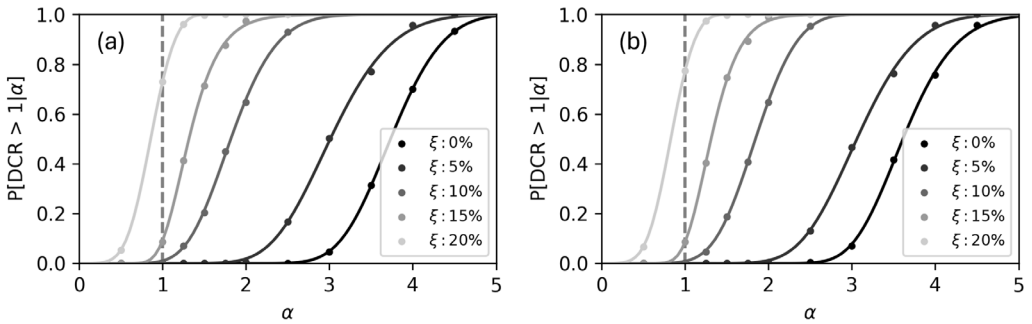


Figure 70 - FE-model fragility curves for (a) three- and (b) four-beam, 40 m-span archetypes.

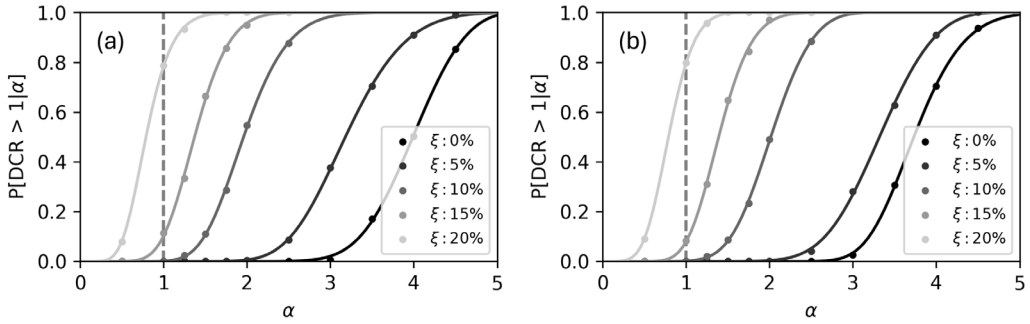


Figure 71 - FE-model fragility curves for (a) three- and (b) four-beam, 50 m-span archetypes.

Given the repeatedly detected irrelevance of the variation of the number of beams in the response of a single archetype, shear fragility and its combination with the flexural one is onwards discussed concerning the three-beam archetypes only, although the same concepts apply to the four-beam typologies.

Concerning shear failure mode, fragility points which may be fitted through different CDF distribution typologies are obtained from the analysis. In this case, both lognormal cumulative distribution and GEV distribution well behave at the aim of interpolation. However, the lognormal CDF does not perform very well in few cases, and in general, looking at the covariance matrix values coming from the GEV and lognormal fitting, the GEV distribution shows much better results in terms of representativeness of the dataset. For this reason, shear fragility points interpolated via GEV distributions are herein reported. Fragility parameters are listed in Table 19, Table 20 and Table 21, and curves are shown in Figure 72, Figure 73 and Figure 74.

Table 19 - GEV distribution parameters for shear fragility curves obtained via FE model of the 30m-span, three-beam archetype.

ξ_p [%]	Shape κ	Scale Ψ	Location θ	Median	Dispersion
0	0.168	0.285	1.314	1.415	0.214
10	0.074	0.259	1.224	1.317	0.225
20	0.152	0.243	1.169	1.255	0.208

Table 20 - GEV distribution parameters for shear fragility curves obtained via FE model of the 40m-span, three-beam archetype.

ξ_p [%]	Shape κ	Scale Ψ	Location θ	Median	Dispersion
0	0.199	0.258	1.139	1.231	0.218
10	0.126	0.241	1.055	1.141	0.231
20	0.180	0.229	0.986	1.067	0.226

Table 21 - GEV distribution parameters for shear fragility curves obtained via FE model of the 50m-span, three-beam archetype.

ξ_p [%]	Shape κ	Scale Ψ	Location θ	Median	Dispersion
0	0.186	0.254	1.023	1.113	0.239
10	0.201	0.232	0.952	1.034	0.233
20	0.213	0.234	0.857	0.940	0.256

In this case, results show significant values of failure probability for the code-conforming traffic load intensity, i.e., $\alpha = 1$. For the un-corroded configurations, a probability of shear failure is recorded for this load intensity equal to about 6%, 19% and 33% for the 30m-, 40m- and 50m-span typology, respectively. Hence, a greater vulnerability is proofed for the longest span typology to shear failure in absence of tendon degradation. Such behaviour is also found through the SA procedure and is discussed in the previous section.

Concerning the corrosion influence, results show that, as well as for the SA procedure, the variability of shear response due to corrosion modifications on structures is much less than the one recorded for flexural response. This outcome holds for all the different archetypes. This is related to the shear capacity model adopted in this study, which is less sensitive to the prestressing actions than the flexural mechanism. Indeed, prestressing steel plays a weak role in shear capacity determination, being present only through the term of the mean compression state of the cross-section (see Equation (24)). Much more decisive is the contribution of the geometry of the cross-section. Numeric-wise the decrease in shear fragility curve median equals about 11%, 13% and 15% for the 30m-, 40m- and 50m-span typology, respectively. Due to an increase of corrosion from 0% to 20%, the probability of shear failure for the code-

conforming traffic load increases from 6% to 14%, from 19% to 39% and from 33% to 59% for the same typology, respectively. Thus, the probability of shear failure almost doubles in every case, but the longest span archetype is identified as the most vulnerable to shear failure mechanism, under the modelling assumptions adopted in this work.

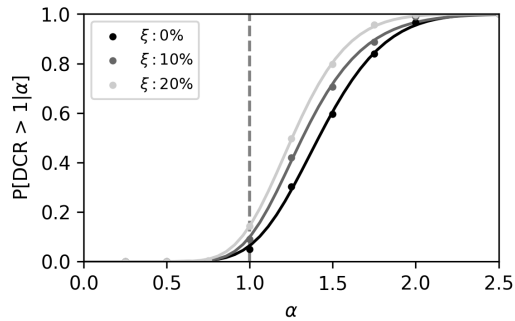


Figure 72 - Shear fragility curves obtained via FE model for the 30m-span, three-beam archetype.

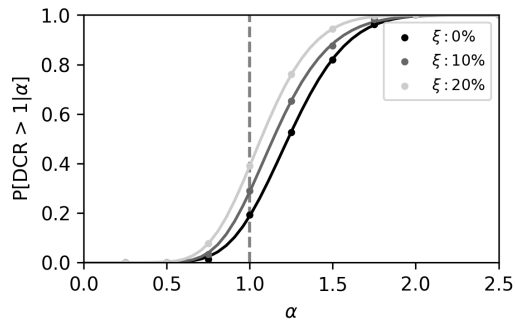


Figure 73 - Shear fragility curves obtained via FE model for the 40m-span, three-beam archetype.

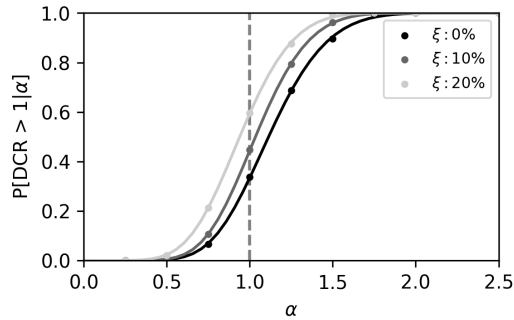


Figure 74 – Shear fragility curves obtained via FE model for the 50m-span, three-beam archetype.

It is worth noting that also for the shear fragility curves, the dispersion is quite low, for both un-corroded and corroded configurations. Indeed, the fragility curve dispersion remains constant with the increasing of corrosion. This shows a low influence of the variable adopted in the problem on the determination of the shear response of the different archetypes.

Given the analysis of the single failure mechanisms, i.e., flexure and shear, it is worth making a comparison between the two, to provide a fragility assessment involving both failure modes at the same time, replicating what has been done with the SA procedure outcomes. By combining the fragility points following the rule explained in Section 4.5, the dataset coming from the combination cannot be well-fitted by a certain probability distribution. For this reason, results are herein kept separated and shown in Figure 75, Figure 76 and Figure 77.

It is clearly visible that the shear mechanism governs the failure mode for all the archetypes, both at 0% and at 10% of corrosion value. Indeed, the probability of shear failure corresponding to the un-corroded configuration is far lower than the value of the probability of the flexural one. For this reason, the shear fragility curve can be considered exactly representative of the combined fragility curve. Hence, at zero corrosion value, what has been explained above for the shear fragility holds also for the combined one, i.e., the most vulnerable typology is the one with the longest span value. For the un-corroded configuration, this outcome is consistent with the results obtained via the SA procedure.

As corrosion increases to 10%, the distance between the corresponding fragility curves reduces. If the distance between the medians of the flexural and shear fragility curves at corresponding corrosion scenarios is taken into account, with an increase in corrosion from 0% to 10%, a reduction of 70%, 73% and 68% is observed for the 30m-, 40m- and 50m-span length archetype, respectively. Still, the combined fragility curve is coincident with the shear one.

As corrosion further increases, the most likely mechanism switches to the flexural one, which at high corrosion scenarios, i.e., 20% corrosion value, becomes dominant in determining the failure mode of all the archetypes. Hence, the combined fragility curve coincides with the flexural one. This outcome is consistent with what has been achieved via the SA procedure as well. If the reduction in the median of the combined fragility curve for an increase in corrosion from 0% to 20% is taken into account, a value of 34%, 30% and 26% is observed for the 30m-, 40m- and 50m-span archetype, respectively. This result shows that, given the validity of the modelling assumptions adopted in this study, in the presence of corrosion, the bridge archetype most affected is the one with the shortest span length. This conclusion is also consistent with the outcomes of the SA procedure.

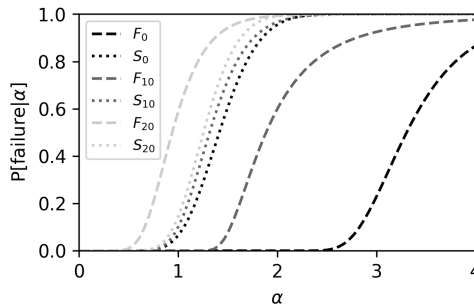


Figure 75 - Shear (S) and flexure (F) fragility curves from the FE model for the 30m-span, three-beam archetype.

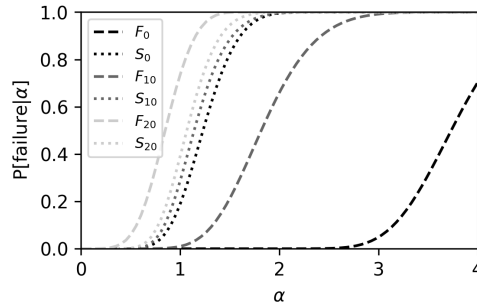


Figure 76 - Shear (S) and flexure (F) fragility curves from the FE model for the 40m-span, three-beam archetype.

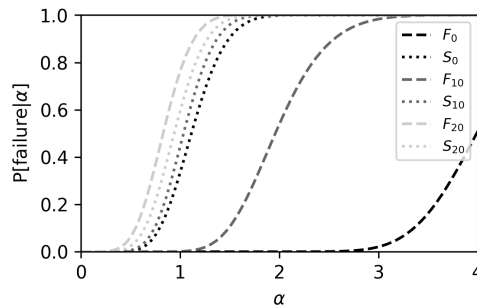


Figure 77 - Shear (S) and flexure (F) fragility curves from the FE model for the 50m-span, three-beam archetype.

8.1.3 Simplified vs FEM strategy

Qualitative-wise, analysing the results obtained through the application of the two different strategies, i.e., the FE modelling and the SA modelling strategy, very similar outcomes are observed. Indeed, as stated in the previous two sections, concerning the traffic load fragility evaluation taking into account the combination of the two failure mechanisms, i.e., flexure and shear, the archetype with the longest span length turns out to be the most vulnerable for both the strategies at low corrosion levels (up to 10%). The shear mechanism governs the failure of the bridge archetypes when the corrosion degree is low, whereas, for scenarios taking into account higher degradation of steel tendons, the flexural mechanism becomes the dominant one. The archetype subjected to the higher decrease in the response, and, hence, the most affected by corrosion, is

the 30m-span typology. These common outcomes can be very useful for the aim of prioritisation among PC bridge typologies, because they provide useful information for channelling resources for both special inspections and the detailed assessment of the most-at-risk typologies.

However, numeric-wise, there are important differences that is worth reporting, analysing the causes and highlighting the relative limitations, that obviously have to be considered, deriving from the assumptions adopted for both the modelling strategies. At this aim, a comparison between the flexural fragility curves obtained for the 30m- and the 40m-span archetypes with three beams is herein performed. Figure 78 and Figure 79 show the fragility curves describing the probability of flexural failure obtained via the application of the FE and SA model, for different corrosion scenarios.

Figure 78 (c) and Figure 79 (c) clearly highlight the differences in the distribution functions representing the probability of flexural failure obtained through the two different strategies. For the un-corroded configurations, the two flexural fragility curves show big differences looking at their probability value. However, with the increase of corrosion degree, the fragility curves get closer and closer. Indeed, the shift in the corresponding fragility curve medians is not constant and reduces as corrosion increases. Table 22 and Table 23 describe the differences in the fragility curve medians Δ_η for the same corrosion scenario.

Table 22 - Reduction in the difference between fragility curve medians for the 30m-span, three-beam typology. η_{FE} is the fragility curve median obtained via the FE strategy, η_{SA} is the fragility curve median obtained via the SA strategy, Δ_η is the absolute difference in the median values.

ξ_p [%]	η_{FE} (ref. Table 13)	η_{SA} (ref. Table 10)	Δ_η
0	3.304	2.150	1.154
20	0.932	0.450	0.392
			-66%

Table 23 - Reduction in the difference between fragility curve medians for the 40m-span, three-beam typology. η_{FE} is the fragility curve median obtained via the FE strategy, η_{SA} is the fragility curve median obtained via the SA strategy, Δ_η is the absolute difference in the median values.

ξ_p [%]	η_{FE} (ref. Table 15)	η_{SA} (ref. Table 11)	Δ_η
0	3.733	2.440	1.293
20	0.857	0.550	0.307
			-76%

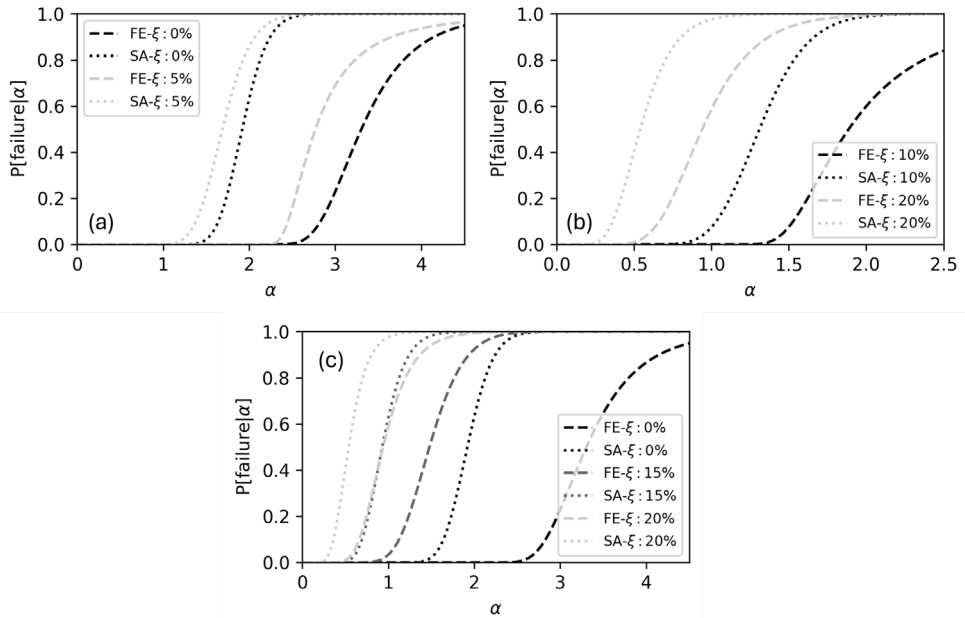


Figure 78 - Flexural fragility curves for the 30m-span, three-beam archetype: comparison between FE and SA modelling strategy.

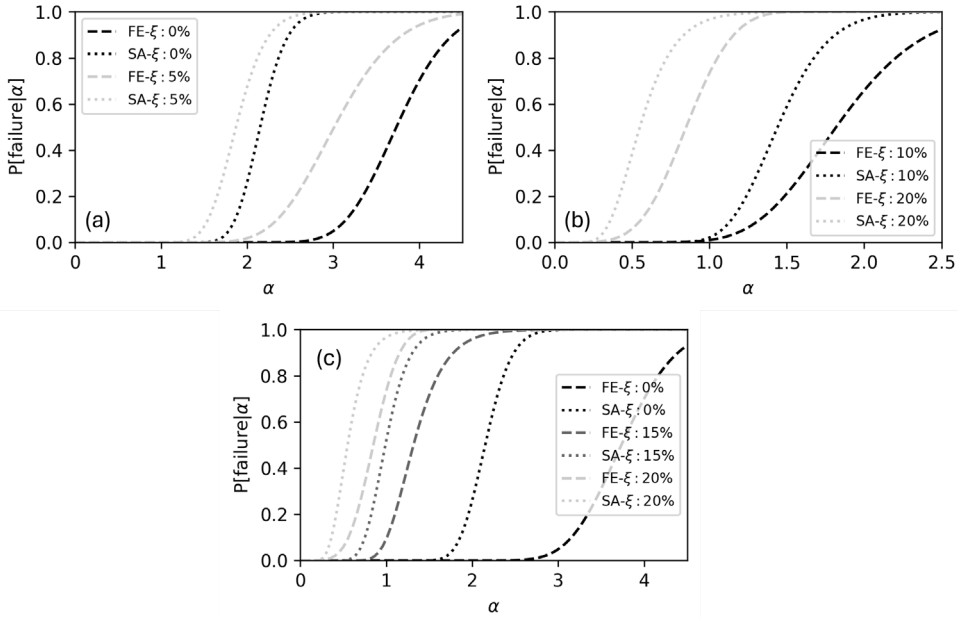


Figure 79 - Flexural fragility curves for the 40m-span, three-beam archetype: comparison between FE and SA modelling strategy.

Considering low corrosion scenarios, such big differences in fragility curves are explainable mainly with two considerations on structural capacity. Examining the behaviour of the same bridge realisation at equal load conditions and degradation scenario, analysed with the two different strategies, 1) slight differences in flexural bearing capacity emerge, with the ultimate bending moment of the critical-cross section computed with FE strategy greater than the SA-computed one (the percentage increase is about 10% on average) and 2) after cracking occurs in the first section, the plastic redistribution capacity within each beam and the load distribution capacity among different beams in the FE model significantly increase the load amplification factor leading to the ultimate limit state compared to the SA strategy. Differences in flexural bearing capacity may be related to the higher accuracy of the FE fibre section modelling compared to the simplifications adopted when computing flexural capacity through the analytical model, e.g., stress-block-type constitutive law for concrete adopted in the SA strategy versus parabola-rectangle for the FE one or the approximations of the cross-

sectional area with variable thickness adopted for the SA strategy compared to the refined fibre model of the FE one.

To justify the differences in flexural response, the demand in bending moment is also investigated. Concerning the flexural demand for the two different strategies, the Courbon-Albenga method neglects the variations in the redistribution of loads among the girders for the bridge superstructure after cracking. For this reason, an increasing linear behaviour is expected for the bending moment demand, with the increase of the load amplification factor. For the FE strategy, the fibre modelling of the cross-section allows capturing the post-cracking behaviour of the beam. Furthermore, the model is able to consider the load redistribution among the different girders of the superstructure. For this reason, an increasing non-linear trend of the demand bending moment is expected for the critical cross-section. Figure 80 illustrates the expected outcomes for both strategies.

Results in the figure show the trend in flexure demand at zero corrosion value for the 30m-span and 40m-span archetypes with four beams, exemplifying the general behaviour of all archetypes. The trends of demand bending moment for the critical cross-section are quite similar at low values of load amplification factors, where the structure is in the linear elastic field, whereas the two trends diverge after the first cracking in the FE model. Higher flexural demands are expected for the Courbon-Albenga method because this is a safety-oriented method in demand computation. The figure confirms such a consideration, more evident for the 30m-span archetype, and less clear for the 40m-span one. At some amplification factors, the mean flexural demand for the FE model slightly exceeds the corresponding demand for the SA strategy. This is related 1) to the initial parasite moments deriving from the prestressing modelling strategy adopted in the FE model and 2) to the fluctuation in the moment demands recorded during the FE displacement-control analysis.

In fact, as explained in Section 7.1, parasite stresses both in terms of shear and flexure can arise in the superstructure elements when modelling prestressing actions in grillage through OpenSeesPy *Initial Strain* material. These stresses influence the response all over the analysis history during the load application process, becoming

almost negligible compared to the stresses achieved at the ultimate limit states but always shifting upwards the response, increasing stresses by a certain little amount. Furthermore, the step size for the displacement-control analysis may also have influences on recorded demand moments. Such an analysis is set to be stopped in correspondence with the first step that records a strain demand in any cross-section material bigger than the relative ultimate strain. Consistently, the corresponding flexure demand is recorded, and for this reason, a flexure moment always a little higher than the actual one is recorded. If a big displacement is adopted as step size for the analysis, this latter may be stopped at higher flexure demand, losing accuracy. Herein, the adopted step size has been calibrated with the aim of running analyses as fast as possible, balancing the size to keep good accuracy. To have a smoother trend of flexure demand in Figure 80, a smaller step size can be adopted to have more refined results. This is proved by the jump in FE demand-moment trend recorded in Figure 80 (a) from the 1.5 to 1.75 load multiplier, as from 1.5 onwards, the displacement adopted as step size for the displacement-control analysis has been intentionally increased to have a faster convergence of analyses. However, a numerical check has been performed to validate this assumption and analyses focused on the multiplier interval from 1.00 to 2.00 have been performed with a small step size. Results are shown in Figure 81, where the jump in the trend is no longer visible, and the two trends, i.e., the mean demand moment obtained through the FE and SA procedure, diverge as expected as the load multiplier increases. The same choice, i.e., a variable step size for the analysis, has been adopted for the 40m-span archetype, increasing the step size from the unit load multiplier onwards. Consequently, in Figure 80 (b), the little jump is anticipated and from that point on, the FE moment trend is smoother.

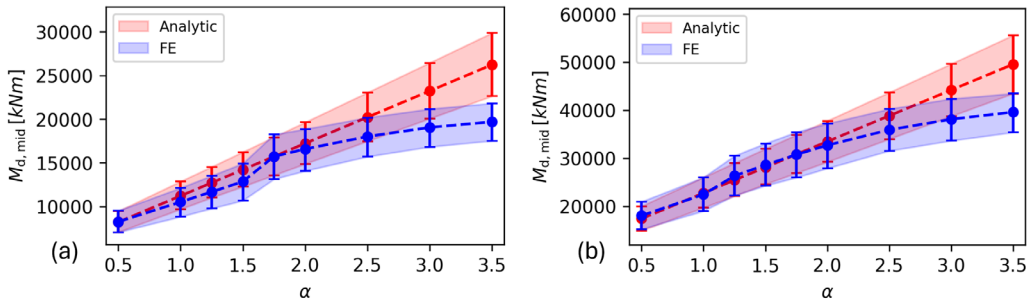


Figure 80 – Mean moment demand for the most loaded beam at zero corrosion value for (a) 30m-span and (b) 40m-span archetype with four beams: a comparison between FE and SA strategy.

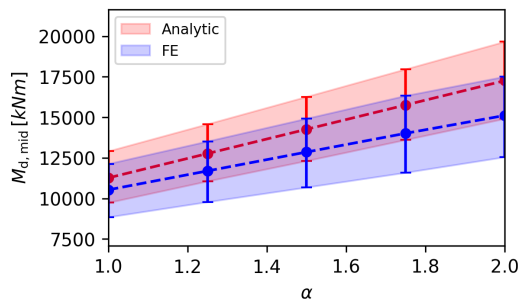


Figure 81 – Mean moment demand for the most loaded beam at zero corrosion value for the 30m-span archetype with four beams: focus on the trend jump due to the change in the step size adopted for the analysis.

As already mentioned, with corrosion increase, the difference between the median of flexural fragility decreases (see Table 22 and Table 23). Figure 78 (b) and Figure 79 (b) highlights this behaviour, showing a comparison between flexural fragility curves at high corrosion scenarios, i.e., 10% and 20% of corrosion degree. This is probably related to the loss in the plastic branch of the prestressing steel, leading to the loss of the plastic redistribution capacity of the single beam, affecting also the load distribution capacity among the girders of the deck. As a consequence, the two different modelling strategies tend to produce more similar outcomes at higher corrosion rates.

Similarly, considerations on the comparison between the shear response deriving from the two different modelling strategies can be carried out. This time, the results in terms of the probability of shear failure are quite similar, but constantly shifted

of a certain quantity. Figure 82 (a), (b) and (c) show a greater probability of shear failure deriving from the FE analysis. This result is not expected, as the Courbon-Albenga method is expected to produce higher shear demands, given that the model adopted for computing the beam shear capacity is exactly the same for both strategies.

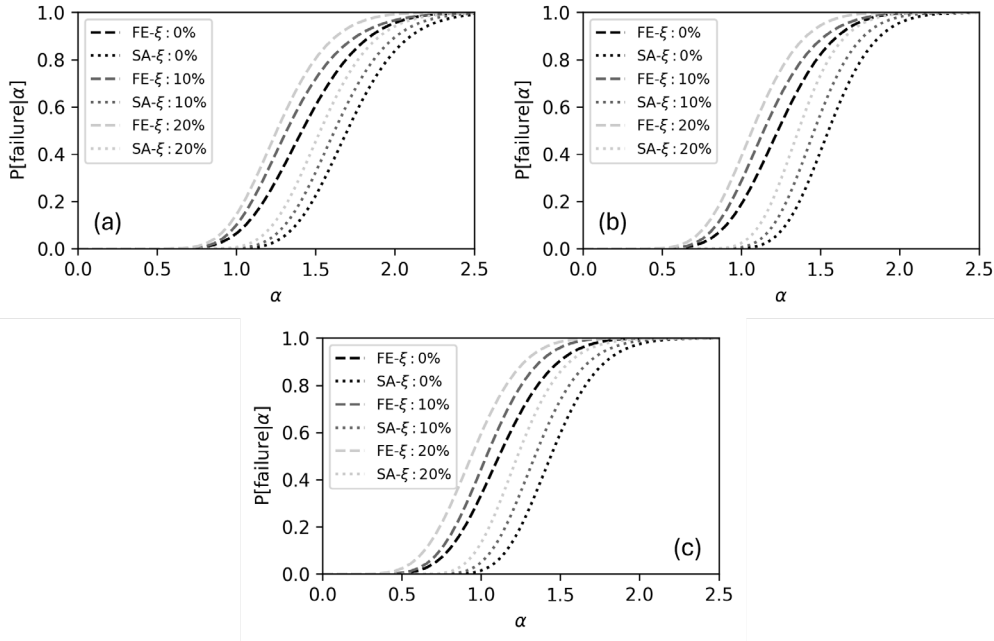


Figure 82 - Shear fragility curves for the (a) 30m-, (b) 40m- and (c) 50m-span, three-beam archetype: comparison between FE and SA modelling strategy

In fact, although the shear capacity model adopted in the two strategies is the same, the differences in cross-section modelling for the two strategies lead to a slightly greater value of shear resistance for the SA strategy. This is related to some local geometry approximations adopted for the analytical model, which in the case of the FE fibre model are not needed.

Furthermore, if shear demand is analysed, similarly to the discussion on flexure demand, a slightly higher shear demand is recorded for the FE strategy. Figure 83 shows the shear demand trends at zero corrosion value for the 30m- and 40m-span archetypes with three beams. An upward shift can be noted in the elastic part of the response. This may be again attributed to 1) the parasite effects of the prestressing

action model adopted in the OpenSeesPy software and 2) the accuracy of the shear demand recording in the FE displacement-control analysis. The differences are more noticeable in Figure 83 (a), as differences are in the order of 100 kN on average compared to a shear demand of 1000 kN. As shear demands increase, as in Figure 83 (b) for the 40m-span, three-beam archetype, the weight of the initial parasite shear stresses decrease, being more negligible. It is worth noting that, being the shear mechanism a brittle failure, no plastic response is recorded in FE shear trends. The two demand trends simply diverge after the shear rupture.

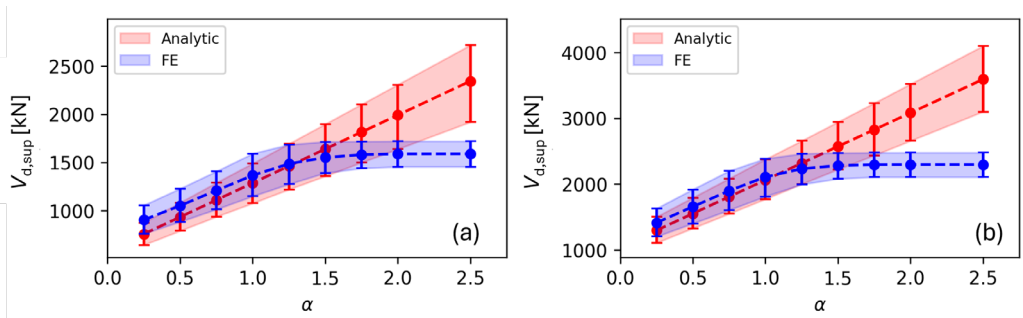


Figure 83 – Mean shear demand for the most loaded beam at zero corrosion value for (a) 30m-span and (b) 40m-span archetype with four beams: a comparison between FE and SA strategy. After reaching the maximum shear demand, corresponding to the shear capacity, the FE model is not able to record higher shear demand values and a constant trend is represented for higher corresponding α values.

Concerning shear failure mode, the corrosion increase does not affect the behaviour equally for both strategies, as prestressing steel has a low influence on the determination of shear capacity, if the capacity model adopted in this study is assumed. Furthermore, the shear mechanism does not involve plastic redistribution, and for this reason no differences are observed between the FE and SA model.

8.2 “Corrosion-affected fragility” accounting for alternative traffic models

Alternative traffic load models proposed by the new Italian Guidelines (Consiglio Superiore dei Lavori Pubblici (CS.LL.PP.), 2020), i.e., models complying with the rules and limitation given by the Italian Road Code (Ministero delle Infrastrutture e dei Trasporti, 1992), are also adopted for the fragility assessment of the PC bridge archetypes.

The refined FE modelling strategy is herein adopted for the application of such load models. Such an analysis strategy allows response evaluation for corrosion degrees up to 25%. Beyond this threshold, initial strain due to prestressing force in tendons tends to overcome the reduced ultimate strain of the prestressing steel computed according to the adopted constitutive law for corroded steel. The objective of the application is to understand how traffic load models other than the ones proposed by the Italian building code (Ministero delle Infrastrutture e dei Trasporti, 2018), hereafter NTC TLM, may be implemented in the proposed methodology.

Although the alternative traffic load models proposed by Italian Guidelines, hereafter LLGG TLM, have an increasing intensity, as evidenced in Section 4.1.2, it is not possible to represent the results of the load application in terms of fragility curves as done up to this point with the NTC TLM. Indeed, fragility curves built for this latter load are based on the amplification of the traffic load intensity, given a certain shape for the traffic model, which is provided by the code. Hence, it is easy to point out a parameter representing an intensity measure (IM) for the traffic load, i.e., the amplification factor itself.

In the case of LLGG TLM application, the different intensities are not given by an amplification factor applied at the same traffic load distribution. The shape of the load model may vary depending on the tandem system adopted for modelling the vehicle actions on the deck. Moreover, the different load models have been defined and calibrated for the assessment of structures subjected to different load situations, therefore, the nature of the different models is inconsistent, making the task of pointing out a common IM meaningless.

Fragility curves to LLGG TLM may be presented by adopting a different approach. For NTC TLM, fragility curves are presented by fixing the corrosion scenario and varying the IM as a parameter representing the load intensity variation for increasing discrete value of corrosion degree. By adopting an inverse logic, i.e., fixing the traffic load model and varying the IM as a parameter representing the variation in corrosion intensity, fragility curves describing the probability distribution of failure can be similarly built and adopted for prioritisation strategies at a large scale. Results deriving from an

application of such a methodology are herein provided, taking into account the flexural failure of the six case-study archetypes. The results derived in such a way are graphically shown in Figure 84, Figure 85 and Figure 86 and numerically listed in Table 24, Table 25, Table 26, Table 27, Table 28 and Table 29.

In the figures, the vulnerability to LLGG TLMs of the six different archetypes is described through fragility points. Indeed, it was not possible to find a probability distribution that performed a good fitting of the obtained flexural fragility dataset. For this reason, fragility points with a linear interpolation for each pair of consecutive points are represented in the figures. This way of showing the results is also meaningful for the aim of understanding the different behaviours of the six bridge archetypes and can be adopted for decision-making of prioritisation strategies in the same way as for the CDF-fitted fragility functions. In the figures, the flexural fragility dataset obtained for the four LLGG TLMs is reported, i.e., the heavy, medium, light and superlight TLMs, indicated by the acronyms CdSHeavy, CdSMedium, CdSLight and CdSSuperLight, respectively. In addition, a comparison with the NTC TLM may be performed, as in the figures also the associated flexural fragility dataset is shown, indicated through the acronym “adequacy”, as this TLM is adopted for the assessment concerning the bridge adequacy limit state, as stated in the Guidelines.

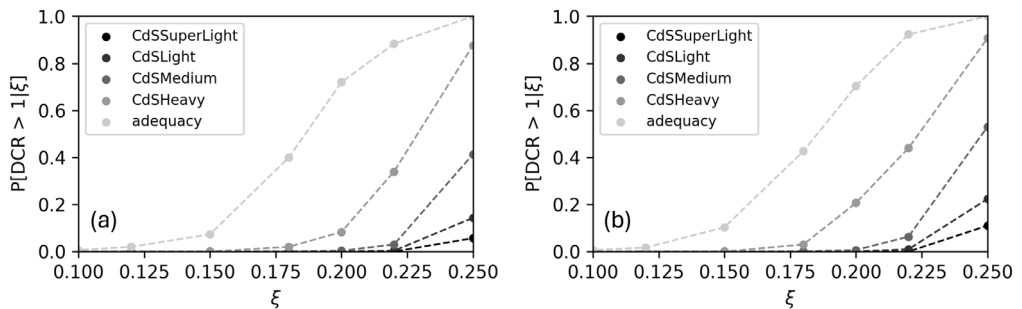


Figure 84 - LLGG TLM flexural fragility curves for (a) 30m-span, three-beam and (b) 30m-span, four-beam archetypes.

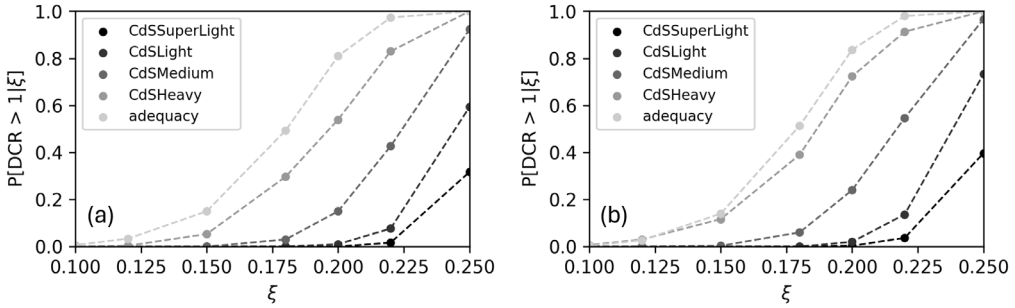


Figure 85 - LGG TLM flexural fragility curves for (a) 40m-span, three-beam and (b) 40m-span, four-beam archetypes.

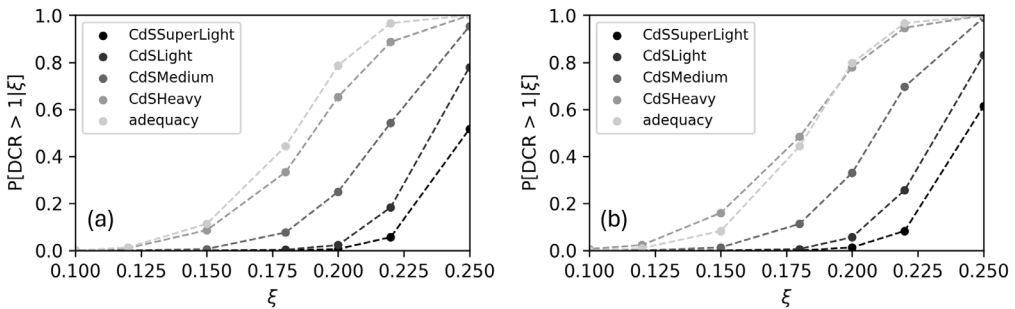


Figure 86 - LGG TLM flexural fragility curves for (a) 50m-span, three-beam and (b) 50m-span, four-beam archetypes.

In general, the three figures and the six tables describe an increasing probability of flexural failure as corrosion increases and as the intensities of the LGG TLMs increase, as expected. Looking separately at the LGG TLMs and NTC TLM, an increase in the probability of flexural failure is observed as the span length increases for the former, whereas a quite constant probability of failure is observed for the latter (see tables below for numbers). Moreover, it is worth noting that also in this analysis the variation in the number of beams for all the archetypes' superstructures does not affect the results. It is also important to highlight that, in general, significant values of flexural failure probability are observed only from 8% of corrosion onwards.

Focusing on the 30m-span archetype, for both the three-beam and the four-beam ones, Figure 84 (a) and Figure 84 (b) clearly show that fragility points obtained through the LGG TLMs have lower values than the fragility points derived from the

application of the NTC TLM. Low failure probability values are observed for the CdSSuperLight and CdSLight, which show a relevant flexural failure probability only at 22-25% of corrosion value. In these two archetypes, the increase in flexural failure probability is evident with the increase of the load intensity scenario, with the adequacy TLM turning out to be the most intense for this archetype, for both values of the number of beams.

For the other two span length archetypes, higher flexural failure probabilities are observed for the LLGG TLMs. This may be related to the shape of the model of the Italian Road Code, which does not prescribe a gradual reduction of the traffic loads for notional lanes which are far from the analysed critical beam. Indeed, the highest value of traffic load prescribed for the notional lane is extended to all the lanes open to traffic, including the emergency lanes, as long as the worst distribution of notional lanes is adopted for the analysed beam. This implies that as the deck width increases, the number of adverse notional lanes with the highest intensity grows, increasing the probability of failure. The same happens for the NTC TLM, however, as described in Section 4.1.1, the shape of this load provides decreasing intensities for the notional lanes moving away from the most loaded critical beam, reducing this growing effect with the increase in the deck width. Among the different assumptions of this work, a regression model is adopted for modelling the deck width (see Table 5 in Section 6.2), choosing the beam spacing for the superstructure as a function of the beam length and the beam height. For this reason, as span length increases, the beam spacing and, consequently, the deck width increase, leading to a growing probability of failure due to the increasing number of notional lanes, all at the highest intensity for the LLGG TLMs.

Hence, the probability of failure associated with the application of the LLGG TLMs gets closer and closer to the one associated with the NTC TLM, with increasing of the span length. It is interesting to note that, for the 50m-span, four-beam archetype, the probability of flexural failure associated with the CdSHeavy at few corrosion values even exceeds the probability of failure associated with the NTC TLM.

Table 24 - Probability of flexural failure to LLGG and NTC TLMs for the 30m-span, three-beam bridge archetype.

TLM	ξ_p [%]							
	0.08	0.1	0.12	0.15	0.18	0.2	0.22	0.25
Adequacy	$<10^{-6}$	0.007	0.020	0.073	0.400	0.720	0.883	1.000
CdSHeavy	$<10^{-6}$	$<10^{-6}$	$<10^{-6}$	$<10^{-6}$	0.020	0.083	0.340	0.877
CdSMedium	$<10^{-6}$	$<10^{-6}$	$<10^{-6}$	$<10^{-6}$	$<10^{-6}$	0.003	0.030	0.413
CdSLight	$<10^{-6}$	$<10^{-6}$	$<10^{-6}$	$<10^{-6}$	$<10^{-6}$	$<10^{-6}$	0.003	0.143
CdSSuperLight	$<10^{-6}$	$<10^{-6}$	$<10^{-6}$	$<10^{-6}$	$<10^{-6}$	$<10^{-6}$	$<10^{-6}$	0.057

Table 25 - Probability of flexural failure to LLGG and NTC TLMs for the 30m-span, four-beam bridge archetype.

TLM	ξ_p [%]							
	0.08	0.1	0.12	0.15	0.18	0.2	0.22	0.25
Adequacy	$<10^{-6}$	0.007	0.017	0.103	0.427	0.703	0.923	1.000
CdSHeavy	$<10^{-6}$	$<10^{-6}$	$<10^{-6}$	$<10^{-6}$	0.030	0.207	0.440	0.907
CdSMedium	$<10^{-6}$	$<10^{-6}$	$<10^{-6}$	$<10^{-6}$	$<10^{-6}$	0.007	0.063	0.530
CdSLight	$<10^{-6}$	$<10^{-6}$	$<10^{-6}$	$<10^{-6}$	$<10^{-6}$	$<10^{-6}$	0.010	0.223
CdSSuperLight	$<10^{-6}$	$<10^{-6}$	$<10^{-6}$	$<10^{-6}$	$<10^{-6}$	$<10^{-6}$	$<10^{-6}$	0.110

Table 26 - Probability of flexural failure to LLGG and NTC TLMs for the 40m-span, three-beam bridge archetype.

TLM	ξ_p [%]							
	0.08	0.1	0.12	0.15	0.18	0.2	0.22	0.25
Adequacy	$<10^{-6}$	0.007	0.033	0.150	0.493	0.810	0.973	1.000
CdSHeavy	$<10^{-6}$	$<10^{-6}$	0.003	0.053	0.297	0.540	0.830	1.000
CdSMedium	$<10^{-6}$	$<10^{-6}$	$<10^{-6}$	$<10^{-6}$	0.030	0.150	0.427	0.923
CdSLight	$<10^{-6}$	$<10^{-6}$	$<10^{-6}$	$<10^{-6}$	$<10^{-6}$	0.010	0.077	0.593
CdSSuperLight	$<10^{-6}$	$<10^{-6}$	$<10^{-6}$	$<10^{-6}$	$<10^{-6}$	$<10^{-6}$	0.017	0.317

Table 27 - Probability of flexural failure to LLGG and NTC TLMs for the 40m-span, four-beam bridge archetype.

TLM	ξ_p [%]							
	0.08	0.1	0.12	0.15	0.18	0.2	0.22	0.25
Adequacy	$<10^{-6}$	0.003	0.027	0.140	0.513	0.837	0.980	1.000
CdSHeavy	$<10^{-6}$	0.007	0.030	0.117	0.390	0.723	0.913	1.000
CdSMedium	$<10^{-6}$	$<10^{-6}$	$<10^{-6}$	0.003	0.060	0.240	0.547	0.967
CdSLight	$<10^{-6}$	$<10^{-6}$	$<10^{-6}$	$<10^{-6}$	$<10^{-6}$	0.020	0.137	0.733
CdSSuperLight	$<10^{-6}$	$<10^{-6}$	$<10^{-6}$	$<10^{-6}$	$<10^{-6}$	0.003	0.037	0.397

Table 28 - Probability of flexural failure to LLGG and NTC TLMs for the 50m-span, three-beam bridge archetype.

TLM	ξ_p [%]							
	0.08	0.1	0.12	0.15	0.18	0.2	0.22	0.25
Adequacy	$<10^{-6}$	$<10^{-6}$	0.013	0.113	0.443	0.787	0.967	1.000
CdSHeavy	$<10^{-6}$	$<10^{-6}$	0.010	0.087	0.333	0.653	0.887	1.000
CdSMedium	$<10^{-6}$	$<10^{-6}$	$<10^{-6}$	0.007	0.077	0.250	0.543	0.953
CdSLight	$<10^{-6}$	$<10^{-6}$	$<10^{-6}$	$<10^{-6}$	0.003	0.023	0.183	0.780
CdSSuperLight	$<10^{-6}$	$<10^{-6}$	$<10^{-6}$	$<10^{-6}$	$<10^{-6}$	0.007	0.057	0.517

Table 29 - Probability of flexural failure to LLGG and NTC TLMs for the 50m-span, four-beam bridge archetype.

TLM	ξ_p [%]							
	0.08	0.1	0.12	0.15	0.18	0.2	0.22	0.25
Adequacy	$<10^{-6}$	$<10^{-6}$	0.010	0.083	0.443	0.797	0.967	1.000
CdSHeavy	$<10^{-6}$	0.007	0.023	0.160	0.483	0.780	0.947	1.000
CdSMedium	$<10^{-6}$	$<10^{-6}$	$<10^{-6}$	0.013	0.113	0.330	0.697	0.990
CdSLight	$<10^{-6}$	$<10^{-6}$	$<10^{-6}$	$<10^{-6}$	0.007	0.057	0.257	0.830
CdSSuperLight	$<10^{-6}$	$<10^{-6}$	$<10^{-6}$	$<10^{-6}$	$<10^{-6}$	0.013	0.083	0.613

Considering these results, as proposed for fragility curves (probability of failure) associated with NTC TLM in Section 8.1.1, transport managers' operators can prioritise among a set of bridges belonging to a specific road network for performing appropriate inspections of the relative prestressing steel components. Following the same logic

described previously discussed, for example, a ranking can be computed based on the increase in fragility (failure probability) between the no-corrosion scenario and one in which an expected corrosion value is defined $\bar{\xi}_p$, for a given scenario of traffic load. Whereas in the procedure proposed in Section 8.1.1, a fixed value $\bar{\alpha}$ is needed – and it has to be representative of the traffic load intensity provided for the specific analysed road – the availability of such a fragility dataset allows managers to assume different traffic-load limitations on the network taking into account the actual load intensity complying with the in force Road Code. Priority lists may be drafted in case traffic limitations already exist on the analysed road network, or if they must be imposed in order to limit the expected risk or losses in the investigated bridge portfolio.

9 CONCLUSIONS

9.1 Summary

The fragility of simply supported prestressed-concrete (PC) girder-type bridges subjected to traffic loads, as defined in European and Italian codes, considering the corrosion of steel tendons is investigated in this thesis. A probabilistic assessment methodology is presented to evaluate the failure probability considering the influence of structural, geometrical, and mechanical uncertain parameters, different critical corrosion scenarios and different code-compliant traffic load models. The methodology is not fully probabilistic, as the traffic load is considered deterministic. Corrosion effects are modelled as 1) a percentage loss of prestressing steel tendon area and 2) modifications of the prestressing steel stress-strain relationship. The fragility analysis is carried out by analysing bridge realisations, which are generated by statistical sampling, under incremental traffic loads. The methodology is composed of different computation modules, involving simplified iterative calculations or refined finite element (FE) models, which can be applied automatically for portfolio-scale bridge analysis. It can be efficiently used for prioritisation purposes at a network-level assessment, to highlight critical post-tensioned girder bridges belonging to the most vulnerable typology to be fully inspected with specific surveys, e.g. the ones listed in Section 1.2, and, if needed, consequently assessed in detail. Prioritisation-oriented procedures are needed for such post-tensioned bridges, as corrosion of steel tendons in these structures cannot be evaluated by a simple visual inspection and requires expensive and time-consuming diagnostic campaigns.

The proposed methodology is demonstrated for the investigation of the fragility of PC superstructure typologies extracted from bridges belonging to a road network in Southern Italy. Six archetype superstructure cases of variable span lengths (from 30 to 50) and variable numbers of beams per span are analysed, following two different modelling strategies, i.e., one simplified and one more refined. The following main outcomes, common to both modelling strategies adopted, are observed.

- General results deriving from both procedures show that a strong influence is covered by the steel tendon corrosion state, as it significantly affects bridge fragility to traffic loads in all the analysed cases.
- The fragility analysis of the different selected typologies shows that for zero corrosion value, the highest failure probability is recorded for the 50m-span bridge archetype characterised by the minimum number of beams. By using the code-based unscaled traffic load, the probability of failure can range from 3% to 6% depending on the adopted modelling strategy. It is important to underline that these numerical value looks high and needs deeper verification.
- When considering an increase in corrosion level from 0 to 15%, results prove that for the code-based unscaled traffic load, the failure probability is higher than 30% in all the cases.
- The 30m-span bridge typology can be considered the most susceptible to corrosion, as it shows a greater increase in fragility.
- It is observed that the number of beams has a limited influence on fragility results. However, this outcome cannot be extended to a greater number of beams, which needs to be analysed in future developments.
- The dispersion related to fragility curves is generally low and approximately constant within the analysed typologies, proving a homogeneous influence of uncertain parameters on fragility. It can increase with increasing corrosion, which leads to an amplification in the variability of prestressing-steel-related characteristics.
- Results report also that, in case of no corrosion, the shear mechanism always induces failure for the analysed cases. However, the flexural response governs the failure for all bridge typologies presenting a severe corrosion degree, suggesting greater attention on the middle region of PC beams in surveys in case of expected relevant degradation conditions.

9.2 Future developments

The work proposed in the present thesis is definitely not exhaustive. Still many advances have to be made by research in the field of risk-targeted prioritisation. This work aims to add information to the basics of this research topic and the case-study application demonstrates that it could improve the current practices of risk prioritisation, by supporting transportation authorities in ensuring the safety of the existing post-tensioned girder bridges. However, it is worth listing its current limitations to provide suggestions for further investigations and developments. In fact, further developments can be oriented to implement improved modelling strategies for either the bridge structure or the traffic load scheme.

In this regard, more advanced traffic load model proposals are currently available in the scientific literature about bridge assessment. In most of the studies, advanced models consist of probabilistic models aiming at finding traffic actions for refined probabilistic risk or loss assessment (Enright and O'Brien, 2013; O'Brien *et al.*, 2015; Anitori, Casas and Ghosn, 2017; Ruan *et al.*, 2017; Soriano, Casas and Ghosn, 2017). Interestingly, traffic load advanced models are suitable for fragility assessment purposes (Fiorillo and Ghosn, 2018). For this reason, their use perfectly fits the methodology proposed in the present thesis and they can be integrated into the procedure to allow considerations at a risk-assessment level. The reason behind the use of such a refined approach lies in the excessive generalisation of the semi-probabilistic approach to structural reliability (Wiśniewski, Casas and Ghosn, 2012) adopted in current standards (CEN, 2003; American Association of State Highway and Transportation Officials (AASHTO), 2020). Indeed, it is expected that the actual probability according to which the code-prescribed traffic effect is exceeded on a specific bridge in a time interval, i.e., the exceedance return period, depends on the characterisation of the traffic on the specific transportation network to which the bridge belongs (Testa *et al.*, 2023). Structure-specific traffic load analysis is desirable to determine the safety margin under which the bridge operates and to introduce traffic control measures or structural retrofitting actions.

The definition of such a traffic model is strictly subjected to real traffic data availability. In recent years more and more applications related to traffic data have been published due to the increasing number of collected data. For example, recently, the so-called weigh-in-motion (WIM) systems, if installed in strategic places over a single road or in a road network, represent a precious resource for collecting interesting data for these applications (Iervolino *et al.*, 2023). When direct traffic observations are not available, simulation techniques can be adopted to determine a surrogate of detailed structure-specific traffic data (Olstam and Tapani, 2011). Specifically, it is possible to perform traffic micro-simulations to obtain traffic load statistical distributions, and, if available, WIM-collected data can enrich the information basis needed for simulations. However, it is worth highlighting some limitations related to this approach. Indeed, the traffic dataset currently available refers to few years of collection. As stated in Section 4.1.1, LM1 of Eurocode refers to a characteristic value of load, which represents the load intensity with a 1000-year return period for traffic on the main roads in Europe, or equivalently a load intensity with a 5% exceedance probability in 50 years. For this reason, a big limitation in applying collected traffic data to derive traffic statistical distributions for practical applications is represented by the limited amount of time during which these data have been recorded so far. To extrapolate data of a return period of 1000 years from simulations based on collected traffic data in a short time may lead to the risk of obtaining inconsistencies or values of maximum effects on structures which are not reliable and such a problem may affect the final result in an assessment procedure. It is assumed that more and more traffic data will be available in the future, making the integration of such advanced traffic models into bridge risk-assessment methodologies, such as the one proposed in this thesis, more reliable.

Other improvements in the modelling strategies adopted in the present methodology may be related to:

- Although statistical distributions from different contexts are used in this study, it is expected that more statistical data about the structural and geometrical variability of existing highway bridges, specifically for a territorial

context and on a typological basis, will be available in future, improving the reliability of such an approach.

- Advanced corrosion models including specific corrosion types (e.g. pitting corrosion, see the ones listed in Section 3), fatigue-corrosion interaction, effects of corrosion on steel-concrete bonding characteristics and a refined distribution of corrosion among the strands or along the tendons (i.e. spatial variability of corrosion) can improve the current version of the proposed methodology leading to more accurate fragility results (at the expense of computational efficiency and data needed to perform the analysis).
- A probabilistic model of corrosion evolution over time can be also easily implemented, like in the studies proposed in Section 3, to provide the proposed procedure with the possibility of making considerations about life-cycle assessment and maintenance of bridges.
- These fragility outcomes should be completed by further analysis considering the influence of fatigue which is deemed to impact the fragility under traffic loads of bridge superstructures characterised by increasing tendon corrosion.

With such improvements, the methodology could be similarly applied for investigating other case studies within the selected bridge class or other structures belonging to different bridge classes, to systematically apply it in the context of risk-based prioritisation of the existing bridge stock.

10 ACKNOWLEDGEMENTS

The three-year PhD period has been a beautiful and unforgettable journey. So many people have given their precious contribution to my personal growth, by sharing their experiences, advices, or even a simple word. Mentioning just few of them for these acknowledgements simply would not be fair, as well as not citing all the loved people who played an important role in my life before the last three years. For this reason, I would like to keep this brief passage as generic as possible, hoping that whoever reads can identify as a part of it.

I would like to start off by thanking all my Italian supervisors. Professor Uva, Andrea and Sergio most of the time have guided me through the process with wisdom and light-heartedness, creating a perfect room for co-working and building good human relationships.

Along with them, I cannot avoid to thank the entire team of colleagues, or rather, friends, who have accompanied me during these three years. Some of them all the time at my side, some of them have changed, but every single one of them have given me a fundamental contribution, each on its own way, and have represented for myself an occasion of enrichment. I will bring all of you in my heart.

An enormous thank goes to my Spaniard supervisor, Professor Casas, a fundamental reference in my visiting period in Barcelona, one of the most exciting experiences of my life. His peacefulness and trustworthiness inspired me, representing a good example to follow in my personal process of growth, both professional-wise and as human being.

During this time, lots of people have contributed to my professional growth. I would like to thank all the academics, colleagues and professionals I have met in the various occasions, in Italy and abroad, at conferences, PhD courses and summer schools, bridge inspections, because they have been all little parts of this journey and some of them will keep on being so afterwards.

Outside of university, a special thank is mandatory to all the people working in the team of CFEngineering, headed by Denni, who supported me at the beginning and throughout all the period, valuably advising me and infusing me with his experience, as

a solid reference point. I would like all the people of the team to feel involved in this thanksgiving, because with their warm-heartedness they made me feel safe and at-ease during the time spent working together.

Finally, the most important, my loved ones, family and friends. Some of them have played a role during this period, some of them have not, but they constitute the roots that daily provide me with lifeblood, without which I could not live and grow.

11 LIST OF FIGURES

Figure 1 – Verdura (a) and Petrulla (b) Viaduct failures, Agrigento 2014	2
Figure 2 - Annone Viaduct (a), Lecco 2016, and Fossano Viaduct (b), Cuneo 2017.....	3
Figure 3 - Polcevera Bridge failure, Genoa 2018.....	4
Figure 4 - Albiano Magra bridge collapse.	5
Figure 5 - Risk-based prioritisation procedure in Italian 2020 Guidelines for existing bridge assessment.	6
Figure 6 - Prestressed concrete (PC) basic principles, a) reinforced concrete cracked under load; b) post-tensioned concrete before loading; c) post-tensioned concrete after loading.....	9
Figure 7 - Degradation of concrete structures.....	10
Figure 8 - Physical corrosion mechanism and result on concrete members.	18
Figure 9 - Models of corrosion: uniform, pitting and deep-pitting formation (Ge, Yang and Kim, 2023).	23
Figure 10 - Three different pit morphology (Franceschini <i>et al.</i> , 2022).....	25
Figure 11 - Stress-strain behaviour of a corroded steel wire as a function of the cross-sectional loss (Franceschini <i>et al.</i> , 2022).	26
Figure 12 - Load-deformation curves of rupture tests on (a) differently corroded strands and (b) differently corroded wires (Yu <i>et al.</i> , 2022).	28
Figure 13 - Constitutive model for corroded prestressing steel (Yu <i>et al.</i> , 2022).	28
Figure 14 - Standard beam for testing (Rinaldi, Imperatore and Valente, 2010).	30
Figure 15 - Load - midspan displacement curves (Rinaldi, Imperatore and Valente, 2010)	31
Figure 16 - Comparison between analytical ultimate force and experimental outcomes (Rinaldi, Imperatore and Valente, 2010)	32
Figure 17 - (a) GEV distribution fit to 10000 column curvature ductility ratios for the moderate damage state at 75 years of pitting corrosion obtained using pushover	

analysis, and (b) time-evolution of capacity damage state distributions at 25, 50, 75 and 100 years of pitting corrosion. The dotted lines indicate the time-dependent changes in the mean of the fitted distributions to the different damage states (Ghosh and Sood, 2016). 36

Figure 18 - Seismic fragility curves for critical bridge components, such as (a) RC columns. (b) Comparison of system level fragility curves for Slight (S), Moderate (M), Extensive (E), and Complete (C) at the end of service life (100 years) under pitting corrosion using time-evolving seismic demand and capacity models (Ghosh and Sood, 2016). 37

Figure 19 - Variation in annual temperature corresponding to the RCP 4.5 and RCP 8.5 scenarios for South Caroline up to the year 2100. The historical temperature model and the recorded observations of actual temperature originate from the year 1950 (Mortagi and Ghosh, 2022). 38

Figure 20 - A scheme of the two case-study bridges (Mortagi and Ghosh, 2022). 39

Figure 21 - Seismic fragility curves at 50 years of life for columns of (a) MSC steel bridge and (b) MSC reinforced concrete bridge (Mortagi and Ghosh, 2022). ... 40

Figure 22 - Bridge modelling for case-study application (Ge, Yang and Kim, 2023). 42

Figure 23 - Time-dependent seismic fragility curves of bridge column under four deterioration scenarios: (a) U w/o C; (b) P w/o C; (c) U w/ C; (d) P w/ C (Ge, Yang and Kim, 2023). 42

Figure 24 - Obtained time-variant reliability of the two analysed bridges (Wang *et al.*, 2021). 45

Figure 25 - Cross-section of the Ynys-y-Gwas bridge (Al-Mosawe, Neves and Owen, 2022). 46

Figure 26 - Flowchart for fragility analysis..... 50

Figure 27 - Example of the Lane Numbering in the most general case (CEN, 2003). 54

Figure 28 - Application of Load Model 1 (CEN, 2003). 56

Figure 29 - Load Model 1 in Italian standards (Ministero delle Infrastrutture e dei Trasporti, 2018).	58
Figure 30 - Load Model 2, 3, 4 and 5 in Italian standards (Ministero delle Infrastrutture e dei Trasporti, 2018).	59
Figure 31 - Heavy traffic load model conforming to the Italian Road Code, a possible distribution (Consiglio Superiore dei Lavori Pubblici (CS.LL.PP.), 2020). ...	63
Figure 32 - Medium traffic load model conforming to the Italian Road Code, a possible distribution (Consiglio Superiore dei Lavori Pubblici (CS.LL.PP.), 2020). ...	63
Figure 33 - Light traffic load model conforming to the Italian Road Code, a possible distribution (Consiglio Superiore dei Lavori Pubblici (CS.LL.PP.), 2020). ...	64
Figure 34 - Beam cross-section model for ultimate bending moment computation. C_c and C_s are the compression resultant force for concrete and upper steel reinforcements; T_p and T_s are the tensile resultant force for prestressing and bottom steel reinforcements; ε'_s and ε_s are the strains of the mild top and bottom steel; ε_{cu} is the ultimate compressive strain of concrete; $\Delta\varepsilon_p$ is the tensile strain increment of the prestressing steel tendons. Other symbols adopted in the figure are explained in the main text.	77
Figure 35 - Modified stress-strain relationship for corrosion-affected a) prestressing steel strands and b) mild reinforcing steel.	81
Figure 36 - Flowchart for computing corrosion-affected ultimate bending moment M_u	84
Figure 37 - Ratios of the analytically computed P_u to the experimentally tested ultimate load P_{ur} : (a) I procedure vs (b) II procedure.	87
Figure 38 - Geometric and structural characteristics of the case-study superstructures and traffic load model.	91
Figure 39 - Relative errors (RE) as a function of sample size for span length equal to 30 m with (a) 0% and (b) 15 % corrosion degrees; span length equal to 50 m with (c) 0% and (d) 15 % corrosion degrees. SS indicates the optimal sample size.	95
Figure 40 – Simply supported beam adopted for comparing prestressing effects obtained through different prestressing modelling strategies.	99

Figure 41 - Prestressing tendon characteristics according to the Morandi system. 100

Figure 42 - Flowchart for FE model generation in OpenSeesPy. 102

Figure 43 - Definition of l_0 , for calculation of effective flange width (CEN, 2004).
..... 105

Figure 44 - Effective flange width parameters (CEN, 2004). 105

Figure 45 - Bearing and node scheme for the 40m-span, four-beam archetype.
..... 107

Figure 46 - Bearing and node scheme for the 50m-span, three-beam archetype.
..... 107

Figure 47 - Three-dimensional view of the grillage model in the reference space, a random realisation of the 40m-span, four-beam archetype. 108

Figure 48 - *Concrete02* model in OpenSeesPy reference manual (Pacific Earthquake Engineering Research Center (PEER), 2008). 109

Figure 49 - *Steel01* material: stress-strain relationship in OpenSees (Pacific Earthquake Engineering Research Center (PEER), 2008; Zsarnóczy *et al.*, 2022). 110

Figure 50 - A random beam cross-section of the 40m-span, three-beam archetype. 111

Figure 51 - *Patch* command in OpenSees (Pacific Earthquake Engineering Research Center (PEER), 2008; Zsarnóczy *et al.*, 2022). 112

Figure 52 - *Layer* command in OpenSees (Pacific Earthquake Engineering Research Center (PEER), 2008; Zsarnóczy *et al.*, 2022). 113

Figure 53 - Moment-curvature relationship for a random realisation of the 40m-span four-beam archetype. 114

Figure 54 - *Section aggregator* command in OpenSees (Pacific Earthquake Engineering Research Center (PEER), 2008; Zsarnóczy *et al.*, 2022)..... 115

Figure 55 - Torsion coefficient computation. 118

Figure 56 - Longitudinal beam element with five integration points. 118

Figure 57 - Concentrated forces simulating the application of uniformly distributed loads (UDL) and tandem systems (TS) for the traffic model by Eurocode, an

example on the 40m-span, four-beam archetype. Values in the legend refer to Table 2 in Section 4.1.1..... 121

Figure 58 - Concentrated forces simulating the application of uniformly distributed loads (UDL) and tandem systems (TS) for the “heavy” traffic model by Italian Guidelines, an example on the 40m-span, four-beam archetype. Reference values for the load intensities are reported in Section 4.1.2. 121

Figure 59 - Structure nodal displacements due to prestressing effects for a random realisation of the 40m-span, four-beam bridge archetype. 123

Figure 60 - Structure nodal displacements due to dead loads for a random realisation of the 40m-span, four-beam bridge archetype. 124

Figure 61 - Structure nodal displacements due to traffic load combination maximising flexure at midspan for a random realisation of the 40m-span, four-beam bridge archetype, given a 5%-corrosion scenario and amplification factor for traffic loads equal to 2. 125

Figure 62 - Modifications of the prestressing steel stress-strain relationship due to corrosion for a random bridge-archetype realisation..... 129

Figure 63 – Analytical-model fragility curves for (a) three- and (b) four-beam, 30 m-span archetypes. 132

Figure 64 – Analytical-model fragility curves for (a) three- and (b) four-beam, 40 m-span archetypes. 132

Figure 65 – Analytical-model fragility curves for (a) three- and (b) four-beam, 50 m-span archetypes. 133

Figure 66 - Flexural and shear fragility curves for (a) three- and (b) four-beam, 30 m-span bridges. Legend: F – flexure; S – shear; 0, 10, 20 – 0%, 10% and 20% of corrosion level. 136

Figure 67 - Flexural and shear fragility curves for (a) three- and (b) four-beam, 40 m-span bridges. Legend: F – flexure; S – shear; 0, 10, 20 – 0%, 10% and 20% of corrosion level. 136

Figure 68 - Flexural and shear fragility curves for (a) three and (b) four-beam, 50 m-span bridges. Legend: F – flexure; S – shear; 0, 10, 20 – 0%, 10% and 20% of corrosion level. 136

Figure 69 – FE-model fragility curves for (a) three- and (b) four-beam, 30 m-span archetypes. 141

Figure 70 - FE-model fragility curves for (a) three- and (b) four-beam, 40 m-span archetypes. 141

Figure 71 - FE-model fragility curves for (a) three- and (b) four-beam, 50 m-span archetypes. 142

Figure 72 - Shear fragility curves obtained via FE model for the 30m-span, three-beam archetype. 144

Figure 73 - Shear fragility curves obtained via FE model for the 40m-span, three-beam archetype. 144

Figure 74 – Shear fragility curves obtained via FE model for the 50m-span, three-beam archetype. 145

Figure 75 - Shear (S) and flexure (F) fragility curves from the FE model for the 30m-span, three-beam archetype. 146

Figure 76 - Shear (S) and flexure (F) fragility curves from the FE model for the 40m-span, three-beam archetype. 147

Figure 77 - Shear (S) and flexure (F) fragility curves from the FE model for the 50m-span, three-beam archetype. 147

Figure 78 - Flexural fragility curves for the 30m-span, three-beam archetype: comparison between FE and SA modelling strategy. 149

Figure 79 - Flexural fragility curves for the 40m-span, three-beam archetype: comparison between FE and SA modelling strategy. 150

Figure 80 – Mean moment demand for the most loaded beam at zero corrosion value for (a) 30m-span and (b) 40m-span archetype with four beams: a comparison between FE and SA strategy. 153

Figure 81 – Mean moment demand for the most loaded beam at zero corrosion value for the 30m-span archetype with four beams: focus on the trend jump due to the change in the step size adopted for the analysis..... 153

Figure 82 - Shear fragility curves for the (a) 30m-, (b) 40m- and (c) 50m-span, three-beam archetype: comparison between FE and SA modelling strategy 154

Figure 83 – Mean shear demand for the most loaded beam at zero corrosion value for (a) 30m-span and (b) 40m-span archetype with four beams: a comparison between FE and SA strategy. After reaching the maximum shear demand, corresponding to the shear capacity, the FE model is not able to record higher shear demand values and a constant trend is represented for higher corresponding α values. 155

Figure 84 - LLGG TLM flexural fragility curves for (a) 30m-span, three-beam and (b) 30m-span, four-beam archetypes..... 157

Figure 85 - LLGG TLM flexural fragility curves for (a) 40m-span, three-beam and (b) 40m-span, four-beam archetypes..... 158

Figure 86 - LLGG TLM flexural fragility curves for (a) 50m-span, three-beam and (b) 50m-span, four-beam archetypes..... 158

12 LIST OF TABLES

Table 1 - Number and width of notional lanes (CEN, 2003).....	53
Table 2 - Load Model 1: characteristic values (CEN, 2003).	56
Table 3 - Procedure validation: results of experimental tests vs the analytical methodologies.	85
Table 4 - Statistical distributions for independent variables.	93
Table 5 - Statistical distributions and regression models for dependent variables. L_b is the span length of the beam, d_{sp} is the effective depth of the prestressing tendon system measured from the top fibre of the beam section.	93
Table 6 – Dispersion values of the optimal sample size and the best estimate for the 30m-long span four-beams bridge (RE is the relative error).	95
Table 7 - Fragility parameters corresponding to 30 m-span bridge.....	129
Table 8 - Fragility parameters corresponding to 40 m-span bridge.....	129
Table 9 - Fragility parameters corresponding to 50 m-span bridge.....	130
Table 10 - Flexural and shear fragility curve medians (α value corresponding to 50% failure probability) for three- and four-beams, 30 m-span bridges.....	134
Table 11 - Flexural and shear fragility curve medians (α value corresponding to 50% failure probability) for three- and four-beam, 40 m-span bridges.	134
Table 12 - Flexural and shear fragility curve medians (α value corresponding to 50% failure probability) for three- and four-beam, 50 m-span bridges.	134
Table 13 - GEV distribution parameter for flexural fragility curves of 30m-span, three-beam archetype.	138
Table 14 - GEV distribution parameter for flexural fragility curves of 30m-span, four-beam archetype.	138
Table 15 - GEV distribution parameter for flexural fragility curves of 40m-span, three-beam archetype.	139
Table 16 - GEV distribution parameter for flexural fragility curves of 40m-span, four-beam archetype.	139
Table 17 - GEV distribution parameter for flexural fragility curves of 50m-span, three-beam archetype.	139

Table 18 - GEV distribution parameter for flexural fragility curves of 50m-span, four-beam archetype..... 139

Table 19 - GEV distribution parameters for shear fragility curves obtained via FE model of the 30m-span, three-beam archetype..... 142

Table 20 - GEV distribution parameters for shear fragility curves obtained via FE model of the 40m-span, three-beam archetype..... 143

Table 21 - GEV distribution parameters for shear fragility curves obtained via FE model of the 50m-span, three-beam archetype..... 143

Table 22 - Reduction in the difference between fragility curve medians for the 30m-span, three-beam typology. η_{FE} is the fragility curve median obtained via the FE strategy, η_{SA} is the fragility curve median obtained via the SA strategy, $\Delta\eta$ is the absolute difference in the median values. 148

Table 23 - Reduction in the difference between fragility curve medians for the 40m-span, three-beam typology. η_{FE} is the fragility curve median obtained via the FE strategy, η_{SA} is the fragility curve median obtained via the SA strategy, $\Delta\eta$ is the absolute difference in the median values. 149

Table 24 - Probability of flexural failure to LLGG and NTC TLMs for the 30m-span, three-beam bridge archetype. 160

Table 25 - Probability of flexural failure to LLGG and NTC TLMs for the 30m-span, four-beam bridge archetype..... 160

Table 26 - Probability of flexural failure to LLGG and NTC TLMs for the 40m-span, three-beam bridge archetype. 160

Table 27 - Probability of flexural failure to LLGG and NTC TLMs for the 40m-span, four-beam bridge archetype..... 161

Table 28 - Probability of flexural failure to LLGG and NTC TLMs for the 50m-span, three-beam bridge archetype. 161

Table 29 - Probability of flexural failure to LLGG and NTC TLMs for the 50m-span, four-beam bridge archetype..... 161

13 BIBLIOGRAPHY

Abramowitz, M. and Stegun, I.A. (1972) *Handbook of Mathematical Functions with Formulas, Graphs, and Mathematical Tables*. 9th edn. Dover, New York, NY.

Albenga, G. (1930) *Lezioni di ponti*. Torino: U.T.E.T.

Al-Mosawe, D., Neves, L. and Owen, J. (2022) 'Reliability analysis of deteriorated post-tensioned concrete bridges: The case study of Ynys-y-Gwas bridge in UK', *Structures*, 41, pp. 242–259. Available at: <https://doi.org/10.1016/j.istruc.2022.04.094>.

American Association of State Highway and Transportation Officials (AASHTO) (2020) *Load and Resistance Factor Design, Bridge Design Specifications*. Washington D.C.

Anania, L., Badalà, A. and D'Agata, G. (2018) 'Damage and collapse mode of existing post tensioned precast concrete bridge: The case of Petrulla viaduct', *Engineering Structures*, 162, pp. 226–244. Available at: <https://doi.org/10.1016/j.eng-struct.2018.02.039>.

Anitori, G. (2021) *Risk-based highway bridge inspection intervals*. Universitat Politècnica de Catalunya. Available at: <https://doi.org/10.5821/dissertation-2117-348908>.

Anitori, G., Casas, J.R. and Ghosn, M. (2017) 'WIM-Based Live-Load Model for Advanced Analysis of Simply Supported Short- and Medium-Span Highway Bridges', *Journal of Bridge Engineering*, 22(10). Available at: [https://doi.org/10.1061/\(asce\)be.1943-5592.0001081](https://doi.org/10.1061/(asce)be.1943-5592.0001081).

Baker, J.W. (2015) 'Efficient analytical fragility function fitting using dynamic structural analysis', *Earthquake Spectra*, 31(1), pp. 579–599. Available at: <https://doi.org/10.1193/021113EQS025M>.

Bazzucchi, F., Restuccia, L. and Ferro, G.A. (2018) 'Considerations over the Italian road bridge infrastructure safety after the polcevera viaduct collapse: Past errors and future perspectives', *Frattura ed Integrità Strutturale*, 12(46), pp. 400–421. Available at: <https://doi.org/10.3221/IGF-ESIS.46.37>.

BBC News (2016) *Italian bridge collapses on busy road in Lecco*, *BBC News Europe*. Available at: <https://www.bbc.com/news/world-europe-37810808> (Accessed: 10 October 2024).

Belletti, B. *et al.* (2020) 'Experimental tests on shear capacity of naturally corroded prestressed beams', *Structural Concrete*, 21(5), pp. 1777–1793. Available at: <https://doi.org/10.1002/suco.202000205>.

Bradley, B.A. (2010) 'Epistemic uncertainties in component fragility functions', *Earthquake Spectra*, 26(1), pp. 41–62. Available at: <https://doi.org/10.1193/1.3281681>.

Calvi, G.M. *et al.* (2019) 'Once upon a Time in Italy: The Tale of the Morandi Bridge', *Structural Engineering International*, 29(2), pp. 198–217. Available at: <https://doi.org/10.1080/10168664.2018.1558033>.

Caspanello, S. (2018) *Quando a Messina crollò un ponte "targato" Morandi*, *Gazzetta del Sud*. Available at: <https://messina.gazzettadelsud.it/articoli/archivio/2018/08/18/quando-a-messina-crollo-un-ponte-targato-morandi-243bb71e-61d2-441a-8c7e-abad7f2740d0/> (Accessed: 10 October 2024).

Celik, O.C. and Ellingwood, B.R. (2010) 'Seismic fragilities for non-ductile reinforced concrete frames - Role of aleatoric and epistemic uncertainties', *Structural Safety*, 32(1), pp. 1–12. Available at: <https://doi.org/10.1016/j.strusafe.2009.04.003>.

CEN (2003) 'Eurocode 1: Actions on structures - Part 2: Traffic loads on bridges'. Brussels, Belgium.

CEN (2004) 'Eurocode 2: Design of concrete structures - Part 1-1 : General rules and rules for buildings.' Brussels, Belgium.

Climate Change 2013: The Physical Science Basis. Contribution of Working Group I to the Fifth Assessment Report of the Intergovernmental Panel on Climate Change (2013). Cambridge.

Colajanni, P. *et al.* (2016) 'Failure by corrosion in PC bridges: A case history of a viaduct in Italy', *International Journal of Structural Integrity*, 7(2), pp. 181–193. Available at: <https://doi.org/10.1108/IJSI-09-2014-0046>.

Computers and Structures, Inc. (2016) 'SAP2000 Integrated Software for Structural Analysis & Design'. Berkeley, California: Computers and Structures, Inc. Available at: <https://www.csiamerica.com/products/sap2000> (Accessed: 21 October 2024).

Consiglio Superiore dei Lavori Pubblici (CS.LL.PP.) (2020) 'Linee guida per la classificazione e gestione del rischio, la valutazione della sicurezza ed il monitoraggio dei ponti esistenti.'

Cufalo, D. (2013) *Crolla il ponte sul fiume Verdura, ma nessun ferito per miracolo. SS 115 Sciacca-Agrigento spezzata in due., Sicania News*. Available at: <https://www.sicanianews.it/crolla-il-ponte-sul-fiume-verdura-ma-nessun-ferito-strada-statale-115-sciacca-agrigento-spezzata-in-due/> (Accessed: 10 October 2024).

Davis, P.J. and Rabinowitz, P. (1984) *Methods of Numerical Integration*. 2nd edn. Academic Press.

Enright, B. and O'Brien, E.J. (2013) 'Monte Carlo simulation of extreme traffic loading on short and medium span bridges', *Structure and Infrastructure Engineering*, 9(12), pp. 1267–1282. Available at: <https://doi.org/10.1080/15732479.2012.688753>.

Farneti, E. *et al.* (2023) 'Residual service life prediction for bridges undergoing slow landslide-induced movements combining satellite radar interferometry and numerical collapse simulation', *Engineering Structures*, 293. Available at: <https://doi.org/10.1016/j.engstruct.2023.116628>.

Ferro, G.A. *et al.* (2022) 'Collapse of Existing Bridges: From the Lesson of La Reale Viaduct to the Definition of a Partial Safety Coefficient of Variable Traffic Loads', *Journal of Structural Engineering*, 148(11). Available at: [https://doi.org/10.1061/\(ASCE\)ST.1943-541X.0003458](https://doi.org/10.1061/(ASCE)ST.1943-541X.0003458).

FHWA - Office of Research Development and Technology (2013) *Guidelines for Sampling, Assessing, and Restoring Defective Grout in Prestressed Concrete Bridge Post-Tensioning Ducts*.

Fiorillo, G. and Ghosn, M. (2018) 'Fragility analysis of bridges due to overweight traffic load', *Structure and Infrastructure Engineering*, 14(5), pp. 619–633. Available at: <https://doi.org/10.1080/15732479.2017.1380675>.

Franceschini, L. *et al.* (2022) 'Mechanical behaviour of corroded strands under chloride attack: A new constitutive law', *Construction and Building Materials*, 316. Available at: <https://doi.org/10.1016/j.conbuildmat.2021.125872>.

Franceschini, L. *et al.* (2023) 'A simplified stress–strain relationship for the mechanical behavior of corroded prestressing strands: The SCPs-model', *Structural Concrete*, 24(1), pp. 189–210. Available at: <https://doi.org/10.1002/suco.202200170>.

Fulloni, A. (2017) *Crolla un viadotto a Fossano Schiacciata auto dei carabinieri*, *Corriere della Sera*. Available at: https://www.corriere.it/cronache/17_aprile_18/crolla-viadotto-fossano-schiacciata-auto-carabinieri-ae2f0300-243f-11e7-9ccc-1412672da04e.shtml (Accessed: 10 October 2024).

Ge, B., Yang, Y. and Kim, S. (2023) 'Time-dependent multi-hazard seismic vulnerability and risk assessment of deteriorating reinforced concrete bridges considering climate change', *Structures*, 55, pp. 995–1010. Available at: <https://doi.org/10.1016/j.istruc.2023.06.068>.

Ghosh, J. and Sood, P. (2016) 'Consideration of time-evolving capacity distributions and improved degradation models for seismic fragility assessment of aging highway bridges', *Reliability Engineering and System Safety*, 154, pp. 197–218. Available at: <https://doi.org/10.1016/j.res.2016.06.001>.

Guo, Z. *et al.* (2024) 'Probabilistic fatigue life prediction of corroded PC beams considering spatial variability of pitting corrosion', *Engineering Structures*, 306. Available at: <https://doi.org/10.1016/j.engstruct.2024.117721>.

Hambly, E.C. (1991) *Bridge Deck Behaviour*. 2nd edn. London and New York: Taylor & Francis.

Iervolino, I. *et al.* (2023) 'Empirical distributions of traffic loads from one year of weigh-in-motion data', *Scientific Data*, 10(1). Available at: <https://doi.org/10.1038/s41597-023-02212-0>.

Iman, R.L. and Conover, W.J. (1982) 'A Distribution-Free Approach to Inducing Rank Correlation Among Input Variables', *Communications in Statistics - Simulation and Computation*, 11(3), pp. 311–334. Available at: <https://doi.org/10.1080/03610918208812265>.

Iori, T. and Poretti, S. (2009) 'The Golden Age of "Italian Style" Engineering', in *Proceedings of the Third International Congress on Construction History*. Berlin: Brandenburg University of Technology Cottbus, Germany.

IPCC (2019) 'Summary for Policymakers', *IPCC Special Report on the Ocean and Cryosphere in a Changing Climate* [Preprint].

Jacinto, L. *et al.* (2012) 'Probabilistic models for mechanical properties of prestressing strands', *Construction and Building Materials*, 36, pp. 84–89. Available at: <https://doi.org/10.1016/j.conbuildmat.2012.04.121>.

Jeon, C.H. *et al.* (2019) 'Equivalent material model of corroded prestressing steel strand', *Journal of Materials Research and Technology*. Elsevier Editora Ltda, pp. 2450–2460. Available at: <https://doi.org/10.1016/j.jmrt.2019.02.010>.

Joint Committee on Structural Safety (2001) 'JCSS. Probabilistic Model Code'.

Kim, J. and Song, J. (2021) 'Time-Dependent Reliability Assessment and Updating of Post-tensioned Concrete Box Girder Bridges Considering Traffic Environment and Corrosion', *ASCE-ASME Journal of Risk and Uncertainty in Engineering Systems, Part A: Civil Engineering*, 7(4). Available at: <https://doi.org/10.1061/ajrua6.0001188>.

Kluyver, T. *et al.* (2016) 'Jupyter Notebooks – a publishing format for reproducible computational workflows', in F. Loizides and B. Schmidt (eds) *Positioning and Power in Academic Publishing: Players, Agents and Agendas*. IOS Press, pp. 87–90. Available at: <https://doi.org/10.3233/978-1-61499-649-1-87>.

Li, C.Q. (2003) 'Life-Cycle Modeling of Corrosion-Affected Concrete Structures: Propagation', *Journal of Structural Engineering*, 129(6), pp. 753–761. Available at: [https://doi.org/10.1061/\(ASCE\)0733-9445\(2003\)129:6\(753\)](https://doi.org/10.1061/(ASCE)0733-9445(2003)129:6(753)).

Mazzatura, I. *et al.* (2023) 'Damage detection, localization, and quantification for steel cables of post-tensioned bridge decks', *Structures*, 57. Available at: <https://doi.org/10.1016/j.istruc.2023.105314>.

McKay, M.D., Beckman, R.J. and Conover, W.J. (1979) 'A Comparison of Three Methods for Selecting Values of Input Variables in the Analysis of Output from a Computer Code', *Technometrics*, 21(2), p. 239. Available at: <https://doi.org/10.2307/1268522>.

McKenna, F., Fenves, G.L. and Scott, M.H. (2000) 'Open system for earthquake engineering simulation (OpenSees).' University of California, Berkeley.

Messina, D. and Proverbio, E. (2023) 'Effect of prestressing corrosion on failure in bridges', *Structural Concrete*, 24(1), pp. 227–238. Available at: <https://doi.org/10.1002/suco.202200360>.

Microsoft Corporation (2019) 'Visual Studio Code'. Available at: <https://code.visualstudio.com/> (Accessed: 21 October 2024).

Miluccio, G. *et al.* (2021) 'Traffic-load fragility models for prestressed concrete girder decks of existing Italian highway bridges', *Engineering Structures*, 249. Available at: <https://doi.org/10.1016/j.engstruct.2021.113367>.

Ministero delle Infrastrutture e dei Trasporti (1962) 'Circolare n.384 del 14.02.1962, Norme relative ai carichi per il calcolo dei ponti stradali.'

Ministero delle Infrastrutture e dei Trasporti (1992) *Nuovo Codice della Strada*. Italy.

Ministero delle Infrastrutture e dei Trasporti (2018) 'Decreto Ministeriale 17 Gennaio 2018. Aggiornamento delle norme tecniche per le costruzioni. Gazzetta ufficiale n.42 del 20 febbraio 2018.'

Mohd Yassin and Mohd Hisham (1994) 'Nonlinear Analysis of Prestressed Concrete Structures under Monotonic and Cycling Loads'. University of California, Berkeley: PhD dissertation.

Mortagi, M. and Ghosh, J. (2022) 'Consideration of Climate Change Effects on the Seismic Life-Cycle Cost Analysis of Deteriorating Highway Bridges', *Journal of Bridge Engineering*, 27(2). Available at: [https://doi.org/10.1061/\(asce\)be.1943-5592.0001815](https://doi.org/10.1061/(asce)be.1943-5592.0001815).

Nettis, A., Raffaele, D. and Uva, G. (2023) 'Seismic risk-informed prioritisation of multi-span RC girder bridges considering knowledge-based uncertainty', *Bulletin of Earthquake Engineering* [Preprint]. Available at: <https://doi.org/10.1007/s10518-023-01783-y>.

Nettis, A., Saponaro, M. and Nanna, M. (2020) 'RPAS-based framework for simplified seismic risk assessment of Italian RC-bridges', *Buildings*, 10(9). Available at: <https://doi.org/10.3390/BUILDINGS10090150>.

Neuenhofer, A. and Filippou, F.C. (1997) 'Evaluation of Nonlinear Frame Finite-Element Models', *Journal of Structural Engineering*, 123(7), pp. 958–966. Available at: [https://doi.org/10.1061/\(asce\)0733-9445\(1997\)123:7\(958\)](https://doi.org/10.1061/(asce)0733-9445(1997)123:7(958)).

O'Brien, E.J. *et al.* (2015) 'A review of probabilistic methods of assessment of load effects in bridges', *Structural Safety*, 53, pp. 44–56. Available at: <https://doi.org/10.1016/j.strusafe.2015.01.002>.

Olstam, J. and Tapani, A. (2011) 'A review of guidelines for applying traffic simulation to level-of-service analysis', in *Procedia - Social and Behavioral Sciences*. Elsevier Ltd, pp. 771–780. Available at: <https://doi.org/10.1016/j.sbspro.2011.04.496>.

Pacific Earthquake Engineering Research Center (PEER) (2008) *OpenSees-Wiki: The Open System for Earthquake Engineering Simulation Wiki*, University of California, Berkeley. University of California, Berkeley. Available at: <https://open-sees.berkeley.edu/wiki/> (Accessed: 21 October 2024).

Park, H.G., Kang, S. and Choi, K.K. (2013) 'Analytical model for shear strength of ordinary and prestressed concrete beams', *Engineering Structures*, 46, pp. 94–103. Available at: <https://doi.org/10.1016/j.engstruct.2012.07.015>.

Di Prisco, M. *et al.* (2018) 'The technical causes of the collapse of Annone overpass on SS.36', in *IL CALCESTRUZZO STRUTTURALE OGGI: TEORIA IMPIEGHI MATERIALI TECNICHE*. Available at: <https://hdl.handle.net/11311/1057236> (Accessed: 3 October 2024).

Redazione AGRIGENTOOGGIIT (2018) *Licata, Crollo del Petrulla: chiesta una condanna ed un rinvio a giudizio*, www.agrigentooggi.it. Available at: <https://www.agrigentooggi.it/licata-crollo-del-petrulla-chiesta-condanna-ed-un-rinvio-giudizio/> (Accessed: 10 October 2024).

Redazione ANSA (2016) *Crollo viadotto, sfiorata tragedia nell'agrigentino, feriti*, www.ansa.it. Available at: <https://www.ansa.it/sicilia/notizie/2014/07/07/crollo->

viadotto-sfiorata-tragedia-nellagrigentino-feriti_f9d703ac-30dc-4496-b691-79977529b266.html (Accessed: 10 October 2024).

Rinaldi, Z., Imperatore, S. and Valente, C. (2010) 'Experimental evaluation of the flexural behavior of corroded P/C beams', *Construction and Building Materials*, 24(11), pp. 2267–2278. Available at: <https://doi.org/10.1016/j.conbuildmat.2010.04.029>.

Van Rossum, G. and Drake, F.L. (2009) 'Python 3 Reference Manual'. Python Software Foundation. Available at: <https://docs.python.org/3/> (Accessed: 21 October 2024).

Ruan, X. *et al.* (2017) 'A site-specific traffic load model for long-span multi-pylon cable-stayed bridges', *Structure and Infrastructure Engineering*, 13(4), pp. 494–504. Available at: <https://doi.org/10.1080/15732479.2016.1164724>.

Sangiorgio, V. *et al.* (2022) 'Analytical fault tree and diagnostic aids for the preservation of historical steel truss bridges', *Engineering Failure Analysis*, 133. Available at: <https://doi.org/10.1016/j.engfailanal.2021.105996>.

Silva, V. *et al.* (2014) 'Evaluation of analytical methodologies used to derive vulnerability functions', *Earthquake Engineering and Structural Dynamics*, 43(2), pp. 181–204. Available at: <https://doi.org/10.1002/eqe.2337>.

Soriano, M., Casas, J.R. and Ghosn, M. (2017) 'Simplified probabilistic model for maximum traffic load from weigh-in-motion data', *Structure and Infrastructure Engineering*, 13(4), pp. 454–467. Available at: <https://doi.org/10.1080/15732479.2016.1164728>.

Su, X. *et al.* (2022) 'Fatigue life prediction for prestressed concrete beams under corrosion deterioration process', *Structures*, 43, pp. 1704–1715. Available at: <https://doi.org/10.1016/j.istruc.2022.07.043>.

Testa, G. *et al.* (2023) 'Infrastructure-level traffic micro-simulation for probabilistic analysis of bridge loads', *Computer-Aided Civil and Infrastructure Engineering*, 38(9), pp. 1217–1235. Available at: <https://doi.org/10.1111/mice.12950>.

Timoshenko, S.P. and Goodier, J.N. (1970) *Theory of Elasticity*. 3rd edn. New York: McGraw-Hill.

Tu, B., Dong, Y. and Fang, Z. (2019) 'Time-Dependent Reliability and Redundancy of Corroded Prestressed Concrete Bridges at Material, Component, and System Levels', *Journal of Bridge Engineering*, 24(9). Available at: [https://doi.org/10.1061/\(asce\)be.1943-5592.0001461](https://doi.org/10.1061/(asce)be.1943-5592.0001461).

Val, D. V. and Melchers, R.E. (1997) 'Reliability of Deteriorating RC Slab Bridges', *Journal of Structural Engineering*, 123(12), pp. 1638–1644. Available at: [https://doi.org/10.1061/\(ASCE\)0733-9445\(1997\)123:12\(1638\)](https://doi.org/10.1061/(ASCE)0733-9445(1997)123:12(1638)).

Vidal, T., Castel, A. and François, R. (2007) 'Corrosion process and structural performance of a 17 year old reinforced concrete beam stored in chloride environment', *Cement and Concrete Research*, 37(11), pp. 1551–1561. Available at: <https://doi.org/10.1016/j.cemconres.2007.08.004>.

Wang, X. *et al.* (2021) 'Full-scale experimental and numerical investigation on the ductility, plastic redistribution, and redundancy of deteriorated concrete bridges', *Engineering Structures*, 234. Available at: <https://doi.org/10.1016/j.engstruct.2021.111930>.

Wiśniewski, D.F., Casas, J.R. and Ghosn, M. (2012) 'Codes for safety assessment of existing bridges-current state and further development', *Structural Engineering International: Journal of the International Association for Bridge and Structural Engineering (IABSE)*, 22(4), pp. 552–561. Available at: <https://doi.org/10.2749/101686612X13363929517857>.

Yu, Q.Q. *et al.* (2022) 'Flexural behavior of Corrosion-Damaged prestressed concrete beams', *Engineering Structures*, 272. Available at: <https://doi.org/10.1016/j.engstruct.2022.114985>.

Zelaschi, C., Monteiro, R. and Pinho, R. (2016) 'Parametric Characterization of RC Bridges for Seismic Assessment Purposes', *Structures*, 7, pp. 14–24. Available at: <https://doi.org/10.1016/j.istruc.2016.04.003>.

Zhou, H. *et al.* (2023) 'Time-variant reliability analysis of simply supported PC girder bridges considering shrinkage, creep, resistance degradation and vehicle load flows', *Structures*, 56. Available at: <https://doi.org/10.1016/j.istruc.2023.104885>.

Zhou, J. *et al.* (2024) 'A hybrid virtual–real traffic simulation approach to reproducing the spatiotemporal distribution of bridge loads', *Computer-Aided Civil and Infrastructure Engineering* [Preprint]. Available at: <https://doi.org/10.1111/mice.13154>.

Zhou, J., Caprani, C.C. and Zhang, L. (2021) 'On the structural safety of long-span bridges under traffic loadings caused by maintenance works', *Engineering Structures*, 240. Available at: <https://doi.org/10.1016/j.engstruct.2021.112407>.

Zhu, M., McKenna, F. and Scott, M.H. (2018) 'OpenSeesPy: Python library for the OpenSees finite element framework', *SoftwareX*, 7, pp. 6–11. Available at: <https://doi.org/10.1016/j.softx.2017.10.009>.

Zsarnóczyay, A. *et al.* (2022) 'OpenSeesPy Documentation: Python interface to the OpenSees framework'. University of California, Berkeley. Available at: <https://open-seespydoc.readthedocs.io/en/latest/> (Accessed: 21 October 2024).

14 CURRICULUM



Alessandro Nettis

Contacts

alessandro.nettis@poliba.it
+39 3332293991
nettisalessandro@gmail.com

Personal information

Date of birth: 28/09/1995
Nationality: Italian
Address: via Luigi Pirandello
40, Acquaviva delle Fonti,
Bari, Italy

EDUCATION

- 2021 – Present: Ph.D., Structural Engineering, Ph.D. Course of Risk and Environmental, Territorial and Building Development, Polytechnic University of Bari
- 2024: Visiting Ph.D., Universitat Politècnica de Catalunya, Department of Civil and Environmental Engineering – Bridge Section, Supervisor: Prof. Joan Ramon Casas, Barcelona, Spain
- 2021: Master of Science in Civil Engineering, Structures, 110/110 Cum Laude, Polytechnic University of Bari
- 2018: Bachelor of Science in Building Engineering, 110/110 Cum Laude, Polytechnic University of Bari
- 2014: High School Diploma, Liceo Scientifico Statale Leonardo da Vinci, Cassano delle Murge, Italy

EXPERIENCE

- 2021 – Present: Structural Engineer at CFEngineering: Ingegneria Strutturale and Consulting, Ing. Ph.D. Domenico Colapietro, Casamassima, Bari, Italy. Support for structural interventions on historical, masonry and reinforced concrete constructions.
- 2022: Bridge Inspections, Consorzio Fabre, Polytechnic University of Bari
- 2021: Traineeship at CFEngineering: Ingegneria Strutturale and Consulting, Ing. Ph.D. Domenico Colapietro, Casamassima, Bari, Italy.

Support for survey, retrofitting and renovation of historic masonry structures, retrofitting of mixed RC/masonry structures, construction of new RC structure.

2018: Traineeship at Studio Petrone&Partners, arch. Petrone, Corato, Bari, Italy. Drafting and reworking of executive details relating to the design of the building envelope of a single-family residence with NZEB energy performance.

PUBLICATIONS

ResearchGate: <https://www.researchgate.net/profile/Alessandro-Nettis>

Authorship convention: for student-authored publications, the student is the first author, and the advisor is the last author. For other authorship positions or larger collaborative papers, authorship order denotes contribution level.

Archival Journal Publications

- **Alessandro Nettis**, Andrea Nettis, S. Ruggieri, G. Uva (2024), "Corrosion-induced fragility of existing prestressed concrete girder bridges under traffic loads.", *Engineering Structures*, Volume 314, 118302, ISSN 0141-0296, <https://doi.org/10.1016/j.engstruct.2024.118302>.
- V. Paris, N. Damiani, M. Sousamli, I. Ehrenbach, M. Lorello, **A. Nettis**, A. Montanino and P. Meriggi (2022), "Traditional tools and modern technologies for the analysis of masonry structures: the case of the Church of Saint Andrea in Anagni," *Structural*, vol. 241, no. 12, doi:10.12917/STRU241.12.

Other Publications

- **Alessandro Nettis**, Andrea Nettis, S. Ruggieri, G. Uva, "Probabilistic traffic load assessment of prestressed girder bridges considering corrosion evolution", 18th World Conference on Earthquake Engineering. At: Milan, June 30 - July 5, 2024
- S. Ruggieri, Andrea Nettis, M. Calò, **Alessandro Nettis**, A. Cardellicchio, G. Uva, "Towards a new vision of civil engineering: digital innovation applications for the structural health management of existing bridge portfolios", iNDiS 2023 - International Scientific Conference Planning, Design, Construction And Building Renewal. At: Novi Sad, Serbia, November 16-17, 2023
- **Alessandro Nettis**, Andrea Nettis, S. Ruggieri, G. Uva, "Fragility analysis of prestressed concrete girder bridges to traffic loads considering tendon corrosion",

EUROSTRUCT 2023: European Association on Quality Control of Bridges and Structures: Digital Transformation in Sustainability. At: Vienna, Austria. Volume 6, Issue 5. DOI: 10.1002/cepa.2059

- **Alessandro Nettis**, Andrea Nettis, S. Ruggieri, G. Uva, “Typological fragility assessment of prestressed concrete girder bridges subjected to traffic loads affected by corrosion”, COMPDYN 2023 9th ECCOMAS Thematic Conference on Computational Methods in Structural Dynamics and Earthquake Engineering. At: Athens, 12-14 June 2023. DOI: 10.7712/120123.10797.21003.

PRESENTATIONS

- “Una valutazione di tipo meccanico della Classe di Attenzione sismica basata sulle nuove Linee Guida italiane sulla sicurezza dei ponti esistenti”, Fabre Conference – *Ponti, viadotti e gallerie esistenti: ricerca, innovazione e applicazioni*, Lucca, Italy, 02-04 February 2022.
- “Typological fragility assessment of prestressed concrete girder bridges subjected to traffic loads affected by corrosion”, COMPDYN 2023, 9th International Conference on Computational Methods in Structural Dynamics and Earthquake Engineering, Athens, Greece, 12-14 June 2023.
- “Probabilistic traffic load assessment of prestressed girder bridges considering corrosion evolution”, 18th World Conference on Earthquake Engineering. Milan, Italy, June 30 – July 5 2024.

TEACHING EXPERIENCE

- Course: “Costruzioni in zona sismica”, SSD ICAR/09, Academic Year 2021-2022. Role: supervisor for the project part of the course.
- Course: “Tecnica delle costruzioni”, SSD ICAR/09, Academic Year 2021-2022. Role: supervisor for the project part of the course.
- Course: “Costruzioni in zona sismica”, Academic Year 2022-2023, Role: supervisor for the project part of the course.
- Course: “Tecnica delle costruzioni”, Academic Year 2022-2023. Role: supervisor for the project part of the course.
- Course: “Costruzioni in zona sismica”, Academic Year 2023-2024. Role: instructor for the exercise and project parts and supervisor for the project part of the course.

ADVISING

- Loseto Chiara, MS, “Modelling and analysis of prestressed concrete girder bridges with post-tensioned tendons.”, 2022. Co-supervisor of the thesis project.
- Carrino Dario, MS, “Safety assessment of existing bridges subjected to traffic loads.”, 2022. Co-supervisor of the thesis project.

LANGUAGE SKILLS

- Italian
- English, Level B2, ISE II – Trinity College London Certificate.

DIGITAL SKILLS

- Structural engineering: SAP2000, CSI Bridge, OpenSees, Straus7, POR2000
- Programming skills: Python, Matlab
- GIS: QGIS
- Graphics: AutoCad, Rhinoceros, Revit
- Other: Microsoft Office, Windows, macOS.

CERTIFICATES

- 2022: METIS Summer School on Seismic Fragility, National Technical University of Athens, at Athens, Greece.
- 2021: International Summer School – Historic Masonry Structures, University of Salerno, Roma Tre, Universidad Politècnica de Madrid, at Anagni, Italy.
- 2021: Complements of construction technique and seismic risk of RC structures, University of Catania, at Catania, Italy.
- 2020: Introductory certificate in Project Management, IPMA Italy.
- 2012: ISE II – Trinity College London, King’s College London, London, United Kingdom.
- 2010: European Computer Driving License (ECDL), AICA, Cassano delle Murge, Bari, Italy.

SERVICE

- Home tutor. Support in studying and teaching of scientific subjects, in particular mathematics and physics for secondary school and university students.
- Volunteering. Summer entertainment activities for children and teenagers from 5 to 13, also with animation groups coordinating function. Education and church activities for boys and girls from 9 to 18.